Università degli Studi di Napoli "Federico II"

Scuola Politecnica e delle Scienze di Base

Ph.D. Thesis

Doctoral Programme

in

Industrial Engineering

Cooperation and Autonomy for UAV Swarms

Supervisors

Prof. D. Accardo

Prof. G. Fasano

Candidate

Amedeo Rodi Vetrella

October 2017

"Tough and Competent."

E.F. Kranz

Abstract

In the last few years, the level of autonomy of mini- and micro-Unmanned Aerial Vehicles (UAVs) has increased thanks to the miniaturization of flight control systems and payloads, and the availability of computationally affordable algorithms for autonomous Guidance Navigation and Control (GNC). However, despite the technological evolution, operations conducted by a single micro-UAV still present limits in terms of performance, coverage and reliability.

The scope of this thesis is to overcome single-UAV limits by developing new distributed GNC architectures and technologies where the cooperative nature of a UAV formation is exploited to obtain navigation information. Moreover, this thesis aims at increasing UAVs autonomy by developing a take-off and landing technique which permits to complete fully autonomous operations, also taking into account regulations and the required level of safety. Indeed, in addition to the typical performance limitations of micro-UAVs, this thesis takes into account also those applications where a multi-vehicle architecture can improve coverage and reliability, and allow real time data fusion. Furthermore, considering the low cost of micro-UAV systems with consumer grade avionics, having several UAVs can be more cost effective than equipping a single vehicle with high performance equipment.

Among several research challenges to be addressed in order to design and operate a distributed system of vehicles working together for real time applications, this thesis focuses on the following topics regarding cooperation and autonomy:

Improvement of UAV navigation performance This research topic aims at improving the navigation performance of an UAV flying cooperatively with one or more UAVs, considering that the only integration of low cost

inertial measurement units (IMUs), Global Navigation Satellite Systems (GNSS) and magnetometers allows real time stabilization and flight control but may not be suitable for applications requiring fine sensor pointing.

The focus is set on outdoor environments and it is assumed that all vehicles of the formation are flying under nominal Global Positioning System (GPS) coverage, hence, the main navigation improvement is in terms of attitude estimation. In particular, the key concept is to exploit Differential GPS (DGPS) among vehicles and vision-based tracking to build a virtual additional navigation sensor whose information is then integrated within a sensor fusion algorithm based on an Extended Kalman Filter (EKF). Both numerical simulations and flight results show the potential of sub-degree angular accuracy. In particular, proper formation geometries, and even relatively small baselines, allow achieving a heading uncertainty that can approach 0.1°, which represents a very important result taking into account typical performance levels of IMUs onboard small UAVs.

UAV navigation in GPS challenging environments This research topic aims at developing algorithms for improving navigation performance of UAVs flying in GPS-challenging environments (e.g. natural or urban canyons, or mixed outdoor-indoor settings), where GPS measurements can be unavailable and/or unreliable. These algorithms exploit aiding measurements from one or more cooperative UAVs flying under nominal GPS coverage and are based on the concepts of relative sensing and information sharing. The developed sensor fusion architecture is based on a tightly coupled EKF that integrates measurements from onboard inertial sensors and magnetometers, the available GPS pseudoranges, position information from cooperative UAVs, and line-of-sight information derived by visual sensors. In addition, if available, measurements coming from a

monocular pose estimation algorithm can be integrated within the developed EKF in order to counteract the position error drift. Results show that aiding measurements from a single cooperative UAV do not allow eliminating position error drift. However, combining this approach with a standalone visual-SLAM, integrating valid pseudoranges in the tightly coupled filtering structure, or exploiting ad hoc commanded motion of the cooperative vehicle under GPS coverage drastically reduces the position error drift keeping meter-level positioning accuracy also in absence of reliable GPS observables.

Autonomous take-off and landing This research activity, conducted during a 6 month Academic Guest period at ETH Zürich, focuses on increasing reliability, versatility and flight time of UAVs, by developing an autonomous take-off and landing technique. Often, the landing phase is the most critical as it involves performing delicate maneuvers; e.g., landing on a station for recharging or on a ground carrier for transportation. These procedures are subject to constraints on time and space and must be robust to changes in environmental conditions. These problems are addressed in this thesis, where a guidance approach, based on the intrinsic Tau guidance theory, is integrated within the end-to-end software developed at ETH Zürich. This method has been validated both in simulations and through real platform experiments by using rotary-wing UAVs to land on static platforms. Results show that this method achieves smooth landings within 10 cm accuracy, with easily adjustable trajectory parameters.

Contents

List of Figures

List of Tables

Chapter 1

Introduction

In the last few years, miniaturization of Flight Control Units (FCUs) and payloads, and the availability of computationally affordable algorithms for autonomous GNC, have contributed to an increasing interest in the development of Unmanned Aerial Systems (UAS) [1, 2].

To give some numbers on the growth of the UAS market, in 2010, the Federal Aviation Administration (FAA) estimated that 15,000 unmanned units would have been employed by 2020 [3]. Surprisingly, with the introduction of the rule for small UAV registration, up to now more than 750,000 UAVs have been registered [4], demonstrating again the great interest behind this technology.

In general, there exist different UAS categories which can be classified on the basis of operational characteristics and their capabilities [5]. One of the adopted classification metric is the Maximum Take-Off Weight (MTOW), where all systems weighing less than 5 kg are defined as micro-UAVs, whereas all UAS with a weight up to 30 kg are labelled as Small- or Mini-UAVs [5]. Other classification metrics are: the operational altitude; the maximum range; and the level of autonomy [5].

Nowadays, Small- and micro-UAVs are widely used in military applications and are playing a significant role in civil scenarios where great investments have

been performed by international companies in order to adopt these systems for commercial purposes such as small packet delivery, mixed indoor–outdoor operations, surveillance, relay of wireless data communications, support in the management of hazard and disasters, and monitoring of power lines and pipelines. Indeed, such platforms have very peculiar capabilities, in fact they can work as long as they get the necessary power, they do not suffer from fatigue and illness, are typically smaller than a manned aircraft used in the same role, and usually cheaper in first cost [6].

In some applications, UAVs are remotely piloted and their motion is bounded to remain always within the pilot (certified) Visual Line-of-Sight (VLOS). Hence, the pilot is always in control of the vehicle and limited autonomous capabilities are required to the UAV. As a natural evolution, in the last years a great effort was generated by international companies and research centers to develop fully autonomous UAVs. In this case, UAVs usually fly Beyond Visual Line-of-Sight (BVLOS) and the path to be followed is decided *a priori*, hence a high level of autonomy is required in order to react to unexpected events such as possible collisions or changes in meteorological conditions.

In [7] ten different levels of autonomy are considered, each of which depends on the required level of decision making, situational awareness and operational capability demanded to the UAV. In general, a system is considered fully autonomous when, given mission goals, it is capable to accomplish them also facing unforeseen events [1]. Furthermore, the system must monitor its health status and take actions in case of failures. As a consequence, it is clear that UAS autonomy and operational safety are strictly connected to the following functions

- **Guidance Navigation and Control (GNC)**
- **Situational awareness and decision making capability**

A definition of GNC systems can be found in [8]. In particular guidance nav-

igation and control represent the processes of driving a UAV to achieve assigned mission goals (guidance) by manipulating the inputs to the UAV dynamical system to obtain a desired effect on its output (control), and monitoring its movement from one place to another (navigation). For long range and autonomous operations it is usually necessary to rely on high-performance navigation systems, where the integration of IMUs and GPSs [9] is usually augmented with active or passive Electro-Optical (EO) sensors (e.g. RGB-D, cameras [10] and Light Detection and Ranging (LIDAR)) and/or radars [11, 12].

A further important step to obtain autonomous systems is the situational awareness and decision making capability of an UAV that must be able to detect and identify failures, possible collisions and losses in communication link and react to them. Collision avoidance is one of the most important requirements for the introduction of UAVs into the civil airspace, this is the capability of a UAV to detect static (e.g. ground, buildings) or moving (other vehicles) obstacles and avoid them during the flight. In the last decade many researchers have tackled this problem [13, 14, 15]. In more detail, collision avoidance can be divided in cooperative and non-cooperative. In the first case, obstacles positions are transmitted or known *a priori* and the avoidance maneuver is performed accordingly, in the second case, obstacles positions are unknown and the collision is avoided thanks to sensing systems usually based on active (lidars, radars) and/or passive (cameras) sensors.

All these elements represent research gaps that must be further addressed.

1.1 Why cooperation?

In spite of a fast technological evolution, operations based on a single micro-UAS still present limits in terms of performance, coverage and reliability. In fact, there are various applications where real time coverage of large areas is

required, which can not be achieved by a single-UAV due to the limited onboard power and payload, as well as the limited flight altitude. Moreover, focusing our attention on UAV navigation, this is typically obtained by integrating low cost avionics and GNSS receivers. This results in position accuracies of the order of 5-10 meters and attitude accuracies of approximately 1-5 degrees [16]. Indeed, even larger errors may arise for the heading angle, due to the common adoption of magnetometers and the consequent effects of magnetic uncertainties, sensors errors, interference phenomena generated by compact installation of electronic components on board micro-UAVs, and possible environmental disturbances. In addition, GNSS are highly vulnerable to unintentional (e.g. multipath) and deliberate (e.g. RF interferences, jamming) disruptions making these systems particularly unreliable. As a consequence, the accuracy level reachable throughout the integration of IMU and GNSS measurements suffices for real time stabilization and control, but it is not suitable for applications that require precise positioning and fine sensor pointing, such as direct georeferencing [16] and LIDAR-based 3D mapping [17], where there is a direct link between navigation performance and point cloud reconstruction accuracy. Furthermore, accurate estimates of position and attitude may also play a key role in photogrammetric processing, potentially limiting the need of Ground Control Points (GCPs) for given reconstruction accuracy requirements, helping tie points matching, and reducing the computational time for bundle adjustment [18].

Also, all applications that require precision guidance or multi-vehicle data fusion usually pose more stringent navigation requirements.

As regards positioning, assuming the availability of GPS coverage, a better accuracy up to centimeter level can be obtained exploiting carrier phase differential GPS between dual frequency antennas/receivers located on-board the aircraft and at known locations on ground. Off-the-shelf systems and solutions are nowadays available and recent developments have significantly increased the

level of miniaturization while also reducing the price of this technology. Single frequency carrier phase differential GPS [19] can also be used for accurate positioning, accepting some performance reduction with respect to dual frequency architectures [20] (e.g., longer convergence times and larger error on average). On the other hand, achieving a very accurate attitude solution, with sub-degree errors on all the angles, still presents challenges.

Most of these limits can be overcome by swarms of UAVs that fly and behave in a coordinated, nature-inspired way [2-5]. In fact, these swarms can represent revolutionary tools in fields such as response to natural disasters and homeland security, as in all those civil applications that require fast deployment and the capability to provide accurate sensor information in near real time.

In addition to offering the possibility of the above mentioned applications, where real time coverage of large areas is required, two or more UAVs working together can allow to improve the navigation performance of one or more of them, either in GPS-challenging environments or under nominal GPS coverage.

In the following, the thesis objectives will be focused on identifying and developing new cooperative navigation methods.

Chapter 2

Thesis Objectives

The scope of this thesis is to overcome single-UAV limits by developing new distributed GNC architectures where the cooperative nature of a UAV formation is exploited to obtain navigation information, and innovative strategies for autonomous flight with particular reference to landing. Indeed, in addition to the typical performance limitations of micro-UAVs, this thesis takes into account also those applications where a multi-vehicle architecture can improve coverage and reliability, and allow real time data fusion. Furthermore, as it will be clarified in the following, considering the low cost of micro-UAV systems with consumer grade avionics, having several UAVs can be more cost effective than equipping a single vehicle with high performance equipment.

Among several research challenges to be addressed in order to design and operate a distributed system of vehicles working together for real time applications, this thesis will focus on the following topics regarding cooperation and autonomy

Improvement of UAV navigation performance In this chapter, performance improvement mainly refers to the achievable navigation accuracy, assuming that the only integration of low cost IMUs, GNSS and magnetometers allows real time stabilization and flight control but may not be suitable for

applications requiring fine sensor pointing. This topic of research is discussed in chapter 3, where the focus is set on outdoor environments and it is assumed that all vehicles of the formation are flying under nominal GPS coverage, hence, the main navigation improvement is in terms of attitude estimation. In particular, the key concept is to exploit DGPS among vehicles and vision-based tracking to build a virtual additional navigation sensor whose information are then integrated within a sensor fusion algorithm based on an EKF. The proposed method resembles multi-antenna attitude estimation architectures. However, while the latter ones exploit carrier phase processing and short baselines (known by calibration) between antennas rigidly mounted on the vehicle, the proposed approach can exploit any differential GPS strategy using antennas embarked on different vehicles, where the exact geometry among them is unknown, but the line of sight between antennas can be estimated by vision sensors.

The developed concepts and processing architectures are described in chapter 3, where performance assessment is carried out on the basis of both numerical simulations and flight tests. In the latter ones, navigation estimates derived from the proposed method are compared with those provided by the onboard navigation filter of a customized quadrotor. Moreover, a validation strategy is performed showing the potential of the developed approach, mainly deriving from the possibility to exploit magnetic- and inertial-independent accurate attitude information.

UAV navigation in GPS challenging environments This topic of research presented in chapter 4 aims at developing algorithms for improving navigation performance of UAVs flying in GPS-challenging environments (e.g. natural or urban canyons, or mixed outdoor-indoor settings), where GPS measurements can be unavailable and/or unreliable. These algorithms exploit aiding measurements from one or more cooperative UAVs flying under

nominal GPS coverage and are based on the concepts of: relative sensing; and information sharing. The developed sensor fusion architecture is based on a tightly coupled EKF that integrates measurements from onboard inertial sensors and magnetometers, the available GPS pseudoranges, position information from cooperative UAVs, and line-of-sight information derived by visual sensors. In addition, if available, measurements coming from a monocular pose estimation algorithm can be integrated within the developed EKF in order to counteract the position error drift. Performance analysis is conducted on the basis of numerical simulations and real platform experiments showing the potential of exploiting multi-UAV navigation approaches to operate UAVs in GPS-challenging environments.

Autonomous take-off and landing This research activity, conducted during a 6 month Academic Guest period at ETH Zürich, focuses on increasing reliability, versatility and flight time of UAVs, by developing an autonomous take-off and landing technique. Often, the landing phase is the most critical as it involves performing delicate maneuvers; e.g., landing on a station for recharging or on a ground carrier for transportation. These procedures are subject to constraints on time and space and must be robust to changes in environmental conditions. These problems are addressed in chapter 5 where a guidance approach based on the intrinsic tau guidance theory is integrated within the end-to-end software developed at ETH Zürich. This method has been validated both in simulations and through real platform experiments by using rotary-wing UAVs to land on static platforms. Results show that this method achieves smooth landings within 10 cm accuracy, with easily adjustable trajectory parameters.

Chapter 3

Improvement of UAV Navigation performance

In this chapter, the scientific results relevant to the first research topic are presented. It is worth noting that all the work was conducted in strong collaboration with co-authors and supervisors.

As already mentioned, the idea behind this research topic is to improve UAV navigation performance by adopting a formation of UAVs (multi-UAV approach) and exploiting the spatial diversity of measurements obtained by these cooperating aircraft.

This work has followed several improvements starting from [21] where the concept of integrating GNSS (in particular, GPS) and vision-based measurements to provide inertial- and magnetic-independent attitude information (which can be defined as DGPS/Vision processing) was presented. In particular, [11] discussed direct attitude estimation based on three cooperating vehicles, while in [12] the focus was set on integrating the attitude information within a navigation algorithm based on a loosely coupled EKF. Then, [22] presented a tight integration scheme to combine GNSS and vision-based information. In these papers, code-based differential GPS (DGPS) was used as GNSS information

source. DGPS provides a reliable solution based on kinematic processing, with meter-level accuracy. As it will be clarified in the following, baselines of the order of 100 meters are needed to convert the meter-level relative positioning error into sub-degree angular uncertainty [11] in order to achieve a sub-degree accuracy also in attitude estimation. As a natural evolution, in [23, 24] the DGPS processing has been substituted by a Carrier-phase DGPS (CDGPS) solution as GNSS information source within the considered multi-UAV architecture (in the following CDGPS/Vision). From the performance point of view, the potential availability of cm-level baseline estimation accuracy gives CDGPS/Vision the possibility to provide a significant improvement of attitude estimation accuracy for large baseline, or a significant reduction of the baseline requirements needed to achieve a given attitude accuracy level.

For the sake of clarity, since the developed navigation algorithms can work with any DGPS solution, in the following the definition "DGPS/Vision" will be adopted, and only when necessary we will refer to the CDGPS/Vision method.

This chapter is organized as follows: related work is presented in section 3.1; in section 3.2 the DGPS/Vision logical architecture is described by introducing the assumptions, challenges and strategies in order to exploit DGPS/Vision measurements for navigation purposes; the adopted algorithms are presented in detail in section 3.3; in section 3.4 the potential of the developed DGPS/Vision concept is analyzed; finally testing and validation strategy and experimental results are presented in section 3.5 and section 3.6

3.1 Related Work

Related work mainly concerns two areas of investigation and technical development, i.e., accurate attitude estimation for small and micro UAVs, and cooperative navigation in UAV swarms.

Concerning the improvement of attitude estimation performance for small UAVs, several authors propose algorithmic developments aimed at better attitude estimation accuracy for mini- and micro-UAVs [25, 26]. While the proposed solutions bring an improvement with respect to standard estimation techniques, experimental analyses point out that processing alone cannot overcome limitations of low performance sensors.

A more direct approach for accurate attitude estimation consists in exploiting high performance avionics. Miniaturized tactical grade IMUs (e.g., [27, 28]) are commercially available and are compatible with installation on mini and (most of) micro UAVs, though not at reduced cost. They are usually based on high performance Micro Electro-Mechanical Systems (MEMS) technology, while some Fiber Optic Gyro (FOG) solutions are also available, though limited to mini UAVs because of larger mass and size budgets. In general, when gyroscope accuracy allows measuring Earth rotation rate, this eliminates the need of magnetometers to estimate heading. These sensors enable accurate attitude determination, with roll and pitch errors usually smaller than heading one.

A popular solution for very accurate heading consists in embarking dual GNSS antenna architectures [29, 16] and then relying on carrier phase differential GNSS processing between the antennas (whose installation geometry is fixed and known by calibration). In practical terms, a baseline larger than 1 meter is needed to attain a heading estimation accuracy better than 0.5 degrees [16]. Challenges related to heading estimation by dual antenna architectures include geometric constraints and measurement availability issues. In fact, a baseline of 1 meter or larger may be hard to achieve on most micro UAVs, selected antennas need to have geodetic grade accuracy due to the necessity of a precise definition of their phase centers, and vibration issues may result from using lightweight mounting structures. Furthermore, high accurate estimation is achievable only when integer ambiguity is solved, which depends on GNSS

constellation configuration and operating environment.

Vision-inertial odometry can also be used for accurate attitude estimation within a given time interval, if initial conditions are accurately known [30, 31, 32]. Implementation challenges for UAVs in outdoor environments involve flight in variable illumination conditions and at relatively high altitude.

UAV swarming currently represents a wide and very active area of research [33], with many efforts on formation control, optimal swarm deployment [34], cooperative planning [35], and cooperative navigation. Regarding the latter, most of the research is focused on cooperative localization and/or simultaneous localization and mapping (SLAM) in GPS-denied environments [36, 37].

As stated above, the proposed framework exploits multi-vehicle cooperation to address a different problem, i.e., improving navigation performance when flying under nominal GNSS coverage.

3.2 Cooperative Navigation Architecture

In this work cooperation is exploited to improve the navigation performance of formation flying UAVs in outdoor environments. In particular, let us assume that a formation of at least two UAVs is flying cooperatively. The following definitions are used throughout this chapter to distinguish between two types of platforms

Chief Vehicle whose absolute navigation performance is to be improved. This is equipped with standard navigation equipments such as MEMS inertial/magnetic sensors and a GPS antenna/receiver, and with a vision system (single or multiple cameras).

Deputy Vehicle whose objective is to provide aiding measurements to the chief. The main requirements for deputy vehicle(s) are to embark GPS antennas/receivers, and to fly in formation with the chief.

Focusing the attention on GPS (though the discussion is general to all satellite navigation systems), the main idea is to improve the absolute navigation performance of the chief by exploiting DGPS with deputies and relative sensing by vision. In particular, while the conceived data fusion architecture enables position, velocity and attitude estimation, the focus is set on exploiting cooperation and spatial diversity of the formation for accurate and robust attitude estimation. Indeed, due to the mathematical structure of the adopted EKF (subsection 3.3.4), improving attitude estimation accuracy indirectly brings benefits to position and velocity performance. It is worth noting that, throughout the paper, attitude is parameterized by three successive rotations 321 (heading, pitch, and roll) from the North East Down (NED) reference frame to the Body Reference Frame (BRF).

3.2.1 Assumptions and Requirements

The main assumptions is that all vehicles fly under nominal GPS coverage, that is in outdoor environments that are not subjected to intentional or unintentional jamming. Then, it is assumed that positioning accuracy is the same for all the vehicles. This underlines again that the main interest of this work is relevant to accurate attitude estimation. Indeed, the concept can be extended to scenarios with different positioning accuracies, and, in that case, DGPS can directly improve chief absolute positioning accuracy.

In the proposed concept, formation control is basically aimed at keeping the deputies within the Field of View (FOV) of chief vision system, in order to enable vision-based line of sight estimation. Formation control can also be used to optimize attitude measurement covariance, as it will be made clear in what follows. In all cases, tight formation control is not necessary, and the geometries required for cooperative navigation can be obtained by conventional guidance approaches.

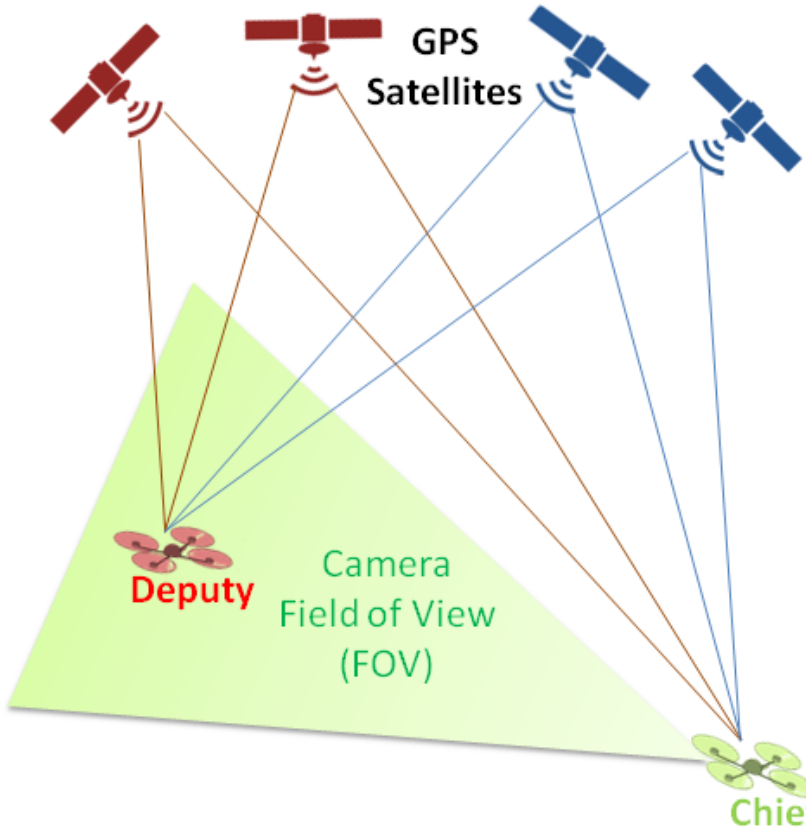

Figure 3.1: Conceptual view of the cooperative navigation scenario in the case of single deputy UAV.

It is worth noting that the distinction between chief and deputy is only functional to the objective of the proposed algorithm, that is improving navigation performance for the chief. Indeed, if GPS observables are exchanged among the vehicles, and if each vehicle is able to track at least another UAV by one or more onboard cameras, each vehicle can exploit cooperation to improve its absolute navigation performance (i.e., each vehicle can be a chief exploiting information from other deputies). A conceptual view of the operation scenario is shown in Figure 3.1.

3.2.2 Communications and synchronization issues

The proposed cooperative navigation technique can be used either in real time or in post processing phase. In the former case, proper communication links have to be foreseen among vehicles.

The need of inter-vehicle communications, and in general of accurate data synchronization (compensating for communication delays in real time applications), might appear as a challenge for the proposed cooperative attitude estimation strategy.

However, the availability of GPS measurements allows accurate and simple synchronization, with residual uncertainties of the order of a very few milliseconds, at most. In fact, all GPS data are time-referenced by GPS receivers, with latencies that are of the order of 1 millisecond. Triggering image acquisitions on the basis of the GPS receiver output enables accurate image timing, also thanks to the high frame rate of latest generation of CMOS/CCD sensors.

As concerns communication delays in real time applications, since the data are time-referenced through the GPS time, the synchronization accuracy is the same whether the processing is performed on-line or in post processing phase. The only difference is that in the first case it is necessary to compensate communication latencies by adopting a method like the negative time measurement update [38] which is an assessed approach for multi-sensor navigation systems integrating vision-based information.

3.2.3 Processing strategies

The key idea to estimate attitude of a chief UAV is to exploit a number of deputy UAVs acting simultaneously as flying antennas and as visual features. DGPS processing provides chief-to-deputies baselines (and thus, the corresponding unit vectors) directly in a stabilized NED reference frame, while vision processing

gives unit vectors in the chief BRF. DGPS and vision-based information can be used in the navigation filter in different ways, such as:

1. directly integrating line-of-sight information in NED and BRF within the estimation process (which works for any number of deputies);

2. using the Three-axis Attitude Determination (TRIAD) algorithm [39] to provide an attitude measurement which is then integrated in the navigation filter (which works for two deputies);

3. using the Quaternion Estimation (QUEST) algorithm [40] to provide an attitude measurement which is then integrated in the navigation filter (which works for more than two deputies).

In this chapter, both the loosely coupled approach based on the TRIAD algorithm, and the tight integration of line-of-sight information within a purposely customized navigation algorithm based on EKF are presented. As anticipated above, this choice has the significant advantage of requiring (at a minimum) only a single deputy UAV to be tracked. A single line-of-sight does not enable straightforward attitude estimation since, as it is intuitive, it does not give any information along its direction. However, depending on the chief-to-deputy geometry, it provides useful information on the attitude error vector. The data fusion algorithm exploits this information and provides its output at high frequency while optimally combining the input data. Moreover, it gives a robust navigation solution in spite of temporary GPS/vision/communication dropouts. Detailed mathematical derivation is given in Section 3.3.

3.3 Algorithm Formulation

Figure 3.2 shows the DGPS/Vision logical architecture where the main processing steps performed on-board the chief vehicle are highlighted (grey blocks).

In the considered architecture, deputy vehicles only need GPS receivers whose output is GPS observables, while the chief vehicle, besides being equipped with a GPS receiver, an IMU and a three-axis magnetometer, is equipped with camera(s) in order to detect and track deputy vehicles.

The core of the algorithm is the multi-sensor fusion which integrates measurements coming from inertial sensors, magnetometers and the on-board GPS receiver with measurements derived by the vision-based tracking and the DGPS, that is chief-deputy LOS in Camera Reference Frame (CRF) and chief-deputy unit vectors in NED respectively. In this section, the DGPS/Vision mathematical formulation and relative integration within the sensor fusion algorithm are presented. In what follows, italic type is used for scalar quantities, italic type with a single underline is used for (generic) vectors, and italic type with double underline is used for matrixes. The symbol "tilde" is used to mean estimated quantity (e.g., $\tilde{R}$), while the symbol "hat" is used for unit vectors (e.g., $\hat{r}$). Apices are used to individuate the reference axes along which vector components are evaluated (e.g., r^{NED}). The symbol $\underline{\underline{R}}_b^n$ individuates the rotation matrix from reference "b" to reference "n".

3.3.1 Vision-based tracking

The vision-based tracking algorithm provides the chief-deputy LOS in the chief BRF. In general, the problem to address is a classical airborne tracking one, for which different solutions are available [41]. However, the considered framework differs from non cooperative visual tracking scenarios such as the ones assumed in sense and avoid [42, 43], since target distance and physical configuration are accurately known. Moreover, regardless of what happened in previous frames, the target detection algorithm can be cued by GPS data and currently estimated chief attitude (Figure 3.2), so that a relatively small search window is always individuated, which can improve target detection reliability and significantly

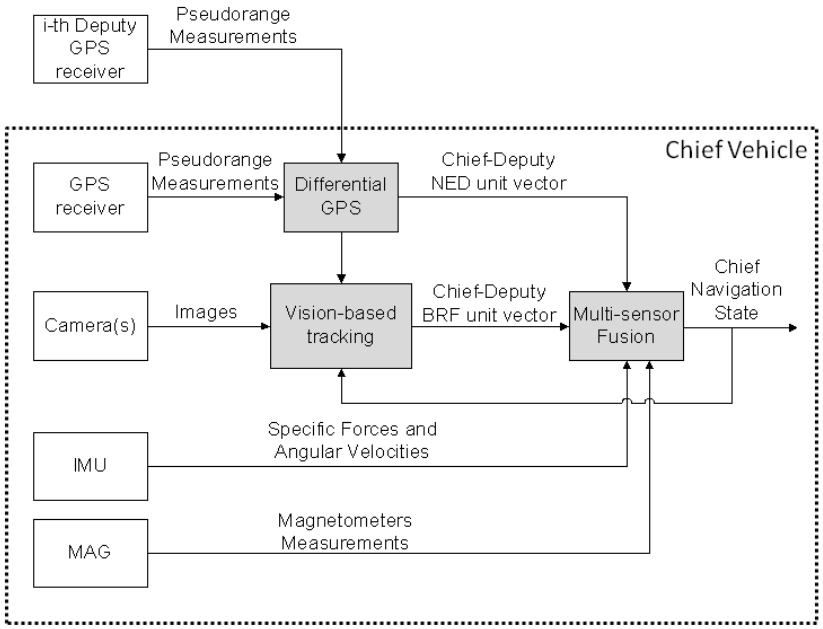

Figure 3.2: Logical architecture of the cooperative navigation algorithm.

reduce processing time. Various techniques include mean-shift color tracking approach [44] or a spatial patch tracking approach such as the Kanade-Lucas-Tomasi (KLT) feature tracker [45, 46].

In the experiments presented in this thesis, once the first frame is acquired by the camera system available on board the chief UAV, the first step of the target detection strategy is to choose the template to be searched in the image. This is done exploiting the range information about the target provided by the relative positioning block, taking into account that a database of template images of the deputy UAVs has been collected experimentally. In this respect, it is worth recalling that the focus has been here set on medium/large UAV-UAV distances, thus the templates shall occupy a limited number of pixels in the image, e.g., ranging from a few tens of pixels to a few pixels.

Once the template is chosen, the Normalized Cross Correlation (NCC) approach is adopted to identify the position of the target UAV in the image plane. However, as already mentioned, the NCC coefficient (γ) is computed over a limited portion of the image in order to limit the computational load and reduce the risk of false alarms. This region of the image plane can be defined by predicting the position of the deputy based on the absolute attitude information of the chief UAV (provided by the on board navigation system) and on the relative positional data (obtained from the differential GPS block).

Once the deputy is detected, a new template, centered at the estimated target position, is extracted from the current frame, and the tracking step can be started. The proposed tracking approach is obtained by combining template matching and morphological filtering [47] which are carried out sequentially over a limited image region. Specifically, the tracking search area is defined by predicting the position of the deputy in the current frame based on the target LOS estimated at the previous frame (provided by either detection or tracking algorithms) as well as the variation of the attitude of the chief UAV from the

previous frame (provided by the on board navigation system).

The vision-based tracking algorithm provides the pixel coordinates (u_i,v_i) of the i-th deputy within images acquired by the chief camera(s). The normalized pixel coordinates (u_i^n, v_i^n) of the i-th deputy are then obtained by applying the intrinsic camera model [48] which takes into account the focal length, the principal point coordinates, the radial and tangential distortion coefficients, and the skew coefficient. Consequently Azimuth and Elevation and the chief to i-th deputy unit vectors in CRF are computed as follows

$$Az_{i,CRF} = \tan^{-1}(u_i^n) \tag{3.1}$$

$$El_{i,CRF} = \tan^{-1}(-v_i^n \cos(Az_{i,CRF})) \tag{3.2}$$

$$\hat{r}_i^{CRF} = \begin{bmatrix} \hat{r}_{i,1}^{CRF} \\ \hat{r}_{i,2}^{CRF} \\ \hat{r}_{i,3}^{CRF} \end{bmatrix} = \begin{bmatrix} \cos(El_{i,CRF})\cos(Az_{i,CRF}) \\ \cos(El_{i,CRF})\sin(Az_{i,CRF}) \\ -\sin(El_{i,CRF}) \end{bmatrix} \tag{3.3}$$

where r_i^{CRF} is the unit vector of components ($\hat{r}_{i,1}^{CRF}\hat{r}_{i,2}^{CRF}\hat{r}_{i,3}^{CRF}$) in CRF (whose axes are defined considering the sequence boresight-right-down).

The unit vectors in BRF, are obtained by performing the following transformation

$$\hat{r}_i^{BRF} = \underline{\underline{R}}_c^b \hat{r}_i^{CRF} \tag{3.4}$$

where $\underline{\underline{R}}_c^b$ is the known rotation matrix from CRF to BRF and $\hat{r}_i^{BRF}$ is the unit vector in BRF.

It is worth noting that, vision-based tracking performance for given chief/deputy platforms basically depends on the range to deputies, on environmental conditions (impacting deputy appearance, contrast and background homogeneity),

and on camera(s) parameters, such as quantum efficiency and Instantaneous Field of View (IFOV). Moreover, camera FOV limits the maximum reachable angular separation between deputies.

In order to increase the detection range performance for a given sensor, the IFOV can be reduced increasing optics focal length, and thus reducing the overall FOV and the possibility to detect widely separated deputies. The trade-off between coverage and detection range can be tackled by installing higher resolution sensors and/or multiple camera systems.

3.3.2 Differential GPS

As far as the differential GPS is concerned, this can be implemented in different ways [49, 9]. In more detail, two possible solutions can be adopted: Code-based Differential-GPS; and carrier phased DGPS.

A lower accuracy can be obtained even with single frequency carrier phase differential processing, provided that the integer ambiguity is solved.

As far as the code-based DGPS, this provides a lower accuracy in estimating the relative position but requires hardware that is affordable for commercial micro-UAVs, less observables to be exchanged between different vehicles (basically only pseudoranges from common satellites in view) and much lighter processing.

During this research activity, both code-based and carrier-phased DGPS have been investigated adopting single frequency GPS receivers.

3.3.2.1 Code-based DGPS

As already mentioned, this solution requires low-cost GPS receivers and a light processing.

A basic estimate of code-based DGPS relative positioning accuracy can be obtained multiplying typical Diluition of Precision (DOP) values by the average

User Equivalent Range Error (UERE) accuracy in DGPS operating scenarios. Indeed, this is a conservative approach since pseudorange measurements correlation is increased in differential architectures. This computation leads to a typical 1-sigma accuracy of the order of 0.99 m (horizontal) and 1.86 m (vertical) [50, 49].

The solution adopted in this activity is a Double Difference (DD) code-based DGPS [49], which offers significant advantages due to the cancellation of receivers and satellites clock biases, as well as most of the ionospheric and tropospheric propagation delays.

To derive the chief-deputy unit vector in the NED reference frame, it is assumed that the chief and the i-th deputy are in view of the same n satellites and consequently their pseudorange measurements are available which allow to calculate single and DD observables. In particular, considering two GPS satellites, one of which named pivot, DD observables are obtained as follows

$$PR_{ci}^{ps} = (PR_i^s - PR_i^p) - (PR_c^s - PR_c^p) \tag{3.5}$$

where the superscript p refers to the pivot GPS satellite, which is chosen to be the one with the highest elevation, s refers to the generic satellite ($s = 1, ..., n-1$), the subscripts c and i represent the chief and the i-th deputy vehicle GPS receiver respectively, PR_i^s stands for the pseudorange estimated by the i-th receiver with respect to the s-th satellite, and a similar interpretation holds for the other estimated pseudoranges.

The DD observation model is a non linear function of the baseline $\Delta\underline{r}_i^{ECEF}$ between the chief and i-th deputy in the Earth Centered Earth Fixed (ECEF) reference frame as shown in the following equation

$$PR_{ci}^{ps} = \rho_{ci}^{ps} + \nu_{ci}^{ps} =$$
$$\|\underline{R}_s - (\underline{r}_c + \Delta\underline{r}_i^{ECEF})\| - \|\underline{R}_s - \underline{r}_c\| - \|\underline{R}_p - (\underline{r}_c + \Delta\underline{r}_i^{ECEF})\| + \|\underline{R}_p - \underline{r}_c\| + \nu_{ci}^{ps} \tag{3.6}$$

where ρ_{ci}^{ps} represents the DD between the true pseudoranges, $\underline{r}_c$ is the chief ECEF position, $\underline{R}_p$ and $\underline{R}_s$ are the pivot and s-th satellites ECEF positions and ν_{ci}^{ps} are the non-common mode pseudorange errors. The problem of finding $\Delta\underline{r}_i^{ECEF}$ is solved applying a recursive least square estimation method based on the linearization of the DD observation model [49]. The i-th baseline vector $\Delta\underline{r}_i^{NED}$ in the NED reference frame, with origin in the chief center of mass is then given by:

$$\Delta\underline{r}_i^{NED} = \underline{\underline{R}}_e^n \Delta\underline{r}_i^{ECEF} \tag{3.7}$$

where $\underline{\underline{R}}_e^n$ is the rotation matrix from the ECEF to the navigation frame NED that depends on the chief longitude λ and geodetic latitude μ

$$\underline{\underline{R}}_e^n = \begin{bmatrix} -\sin\mu\cos\lambda & -\sin\mu\sin\lambda & \cos\mu \\ -\sin\lambda & \cos\lambda & 0 \\ -\cos\mu\cos\lambda & -\cos\mu\sin\lambda & -\sin\mu \end{bmatrix} \tag{3.8}$$

Having the chief-deputy baseline vector $\Delta\underline{r}_i^{NED}$ it is straightforward to compute the corresponding unit vector $\hat{r}_i^{NED}$ in NED.

3.3.2.2 Carrier phase DGPS

CDGPS techniques are widely used in both terrestrial, airborne and space application to improve the performance of baseline determination, and precise positioning goals.

Well-assessed techniques, e.g. Real-Time Kinematic (RTK) [51, 52] and EKF-based approaches, are available for dual frequency receivers, leading to

cm-scale accuracy for static terrestrial users up to hundreds km baselines. In space applications, very precise relative positioning, in the order of 10 cm has been demonstrated for formation flying satellites application, [53] characterized by baselines longer than 200 km. Concerning single-frequency users, less assessed results are available [54] with cm-scale accuracy demonstrated on static receivers only.

The possibility to exploit CDGPS information on board mini/micro UAVs derives from the large availability of commercial single frequency receivers providing carrier phase information [19]. Indeed, even dual frequency receivers tailored for small UAS are increasingly available at relatively low cost [20]. From the performance point of view, the potential availability of cm-level baseline estimation accuracy gives CDGPS/Vision the possibility to provide a great improvement of attitude estimation accuracy for large baseline, or a significant reduction of the baseline required to achieve sub-degree accuracy.

Achieving this potential requires considering several issues, such as:

- GNSS-related: processing time, accuracy, continuity, availability and integrity of the differential solution;
- non GNSS-related: error sources whose impact cannot be neglected if a cm-level solution is desired, such as residual data synchronization errors, lever arm effects, and camera angular resolution.

Also in this case, to derive chief-deputy unit vector in the NED reference frame, it is assumed that the chief and the i-th deputy are in view of the same n satellites and consequently their pseudorange and Carrier Phase (CP) measurements are available wich allow to calculate single and DD observables.

In particular, CP and pseudorange observation equations can be written neglecting both ionospheric and tropospheric DD delays [55] as

$$PR_{ci}^{ps} = \rho_{ci}^{ps} + \nu_{ci}^{ps} \tag{3.9}$$

$$L_{ci}^{ps} = \rho_{ci}^{ps} + \lambda_1 n_{ci}^{ps} + \epsilon_{ci}^{ps} \tag{3.10}$$

where PR and L are the pseudo-range and carrier-phase DD measurements respectively, estimated assuming that p is the pivot satellite and $(s = 1, ..., n-1)$ is the index of any other satellite in view by the chief-deputy couple. Hence, n is the number of common satellites in the chief and the deputy UAVs FOV. Again, ν and ϵ are the measurement thermal noises for PR and CP respectively. n_{ci}^{ps} is the double difference ambiguity that multiplies the L1 wavelength λ_1.

The unknown in (Equation 3.9) and (Equation 3.10) are the baseline and the double difference ambiguities.

One of the advantages of double difference measurements is related to the properties of the ambiguities nature. The ambiguities are constant as long as tracking is not lost or a cycle slip occurs, so data over multiple time epochs can be used to estimate them. Moreover, ambiguities are integer numbers, hence equation (Equation 3.10), can be exactly compensated for the effect of the ambiguity, at least in principle.

A common solution [53] for solving equations (Equation 3.9) and (Equation 3.10) is processing the DD measurements by an EKF. A traditional limitation of standard EKF implementations is that the estimated elements of the state vector are real numbers. Therefore, the filter is only able to obtain a real estimate of the Integer Ambiguities (IA). Such estimates are typically referred to as float ambiguities. The result is that the float ambiguities estimated by the filter are real and not integer numbers generating an error in baseline estimation via equations (Equation 3.9) and (Equation 3.10). The error can be significantly reduced replacing the float ambiguities with the corresponding integer ones. This can be accomplished by an integer least square method, e.g. the least square ambiguity decorrelation adjustment (LAMBDA) [56]. In the following, the EKF for baseline estimation and its integration with the LAMBDA

estimator is presented. The latter poses several challenges, besides the improved complexity of the filter. Indeed, integer ambiguities estimated with LAMBDA must be validated before being used, since an error in integer ambiguity fixing can result in filter divergence.

CDGPS - EKF Structure The EKF used for CDGPS baseline estimation, is an evolution of the one introduced by [57]. The filter, which flow chart is depicted in Figure 3.3, uses the DD GPS measurements presented in Equation 3.9 and Equation 3.10 in the correction step. Thus, the measurement vector $\underline{y}$ includes the $n-1$ pseudoranges and CP measurements, whereas the filter state vector $\underline{x}$ includes the unknown of equations Equation 3.9 and Equation 3.10, and is composed by $6+(n-1)$ components, i.e. the baseline $\Delta\underline{r}_i^{ECEF}$, its derivative $\Delta\underline{\dot{r}}_i^{ECEF}$ and the $n-1$ float ambiguities a. Hence, $\underline{x}$ and $\underline{y}$ can be written as

$$\underline{x} = \begin{bmatrix} \Delta\underline{r}_i^{ECEF} \\ \Delta\underline{\dot{r}}_i^{ECEF} \\ a_{ci}^{p1} \\ \vdots \\ a_{ci}^{p(n-1)} \end{bmatrix}, \underline{y} = \begin{bmatrix} PR_{ci}^{p1} \\ \vdots \\ PR_{ci}^{p(n-1)} \\ L_{ci}^{p1} \\ \vdots \\ L_{ci}^{p(n-1)} \end{bmatrix} \tag{3.11}$$

No dynamics is provided for the baseline except its derivative propagates as a random walk, that is $\Delta\underline{\ddot{r}}_i^{ECEF} = \underline{w}_{acc}$, where $\underline{w}_{acc}$ is the white noise on the baseline acceleration. Whilst, the ambiguities are assumed to be constant characterized by unknown initial value. The measurement matrix $\underline{\underline{H}}$ used to estimate the EKF gain that connects the measurements to the state vector, is evaluated performing linearization of Equation 3.9 and Equation 3.10 around the available baseline estimate.

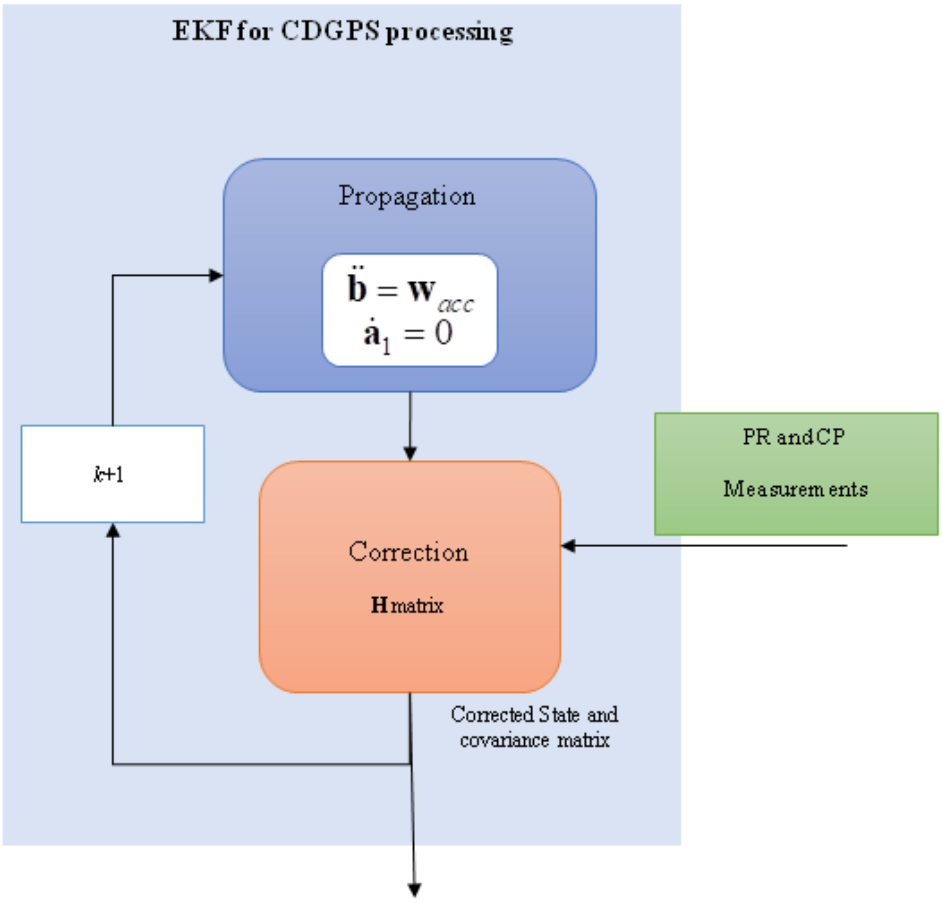

Figure 3.3: CDGPS EKF flow chart.

The accuracy of the baseline estimated by the EKF depends on CP residuals and the satellites-receivers geometry. The CP residuals are obtained by substituting EKF estimates in Equation 3.10 and quantifying the level of uncertainty of filter state vector components. The CP residuals ΔL_{ci}^{ps} are mapped into the baseline error thanks to the DOP coefficients extracted from the $\underline{\underline{H}}$ matrix [58].

CDGPS - EKF Integration with LAMBDA The EKF presented in the previous section estimates the ambiguities as real numbers generating residual errors in the baseline estimation. In order to reduce the baseline error, the

integer nature of DD ambiguities must be exploited. The costs to pay for baseline accuracy improvement are

- a more complex filter to be implemented, able to integrate LAMBDA into the EKF;
- a significant loss of robustness against wrong integer estimates, that easily leads to filter divergence.

The scheme in Figure 3.4 integrates the EKF in Figure 3.3 with the LAMBDA estimator, which returns the integer ambiguities starting from the float estimated by the EKF. The integer ambiguities estimated by LAMBDA are validated and used to correct the current state vector.

The central step in this algorithm is the integer ambiguities validation step, which is in charge of avoiding the wrong integer ambiguities to be fixed. When dual-frequency GPS receivers are adopted, standard RTK techniques can be used to perform robust integer ambiguities validation. When single frequency receivers are adopted, no standard solution exists to deal with the problem of integer validation especially in the case of moving receivers.

The use of integer ambiguity tests is a standard solution in dual-frequency receivers. Tests can be classified as

- Global approaches: if all the IA are simultaneously validated (a list of the most common Global validation tests can be found in [59]). These "vector" validation tests operate on the whole vector of IA, and do not discriminate between IA within the vector, that is, if only one IA within the vector is deemed erroneous, the whole IA vector does not pass the test. On the other hand, when not all the IA are correctly fixed, there is the possibility that a subset of the IA vector

is instead correct.

- Partial approaches: are concerned with discriminating between the single IA, i.e. separating the correct from the incorrect ones. The partial integer validation allows therefore to fix the correct IA before all the ambiguities in the vector become correct, easing the filter estimation, and, as a consequence, this approach should be preferred with respect to the Global one. Most of the partial tests available in literature allow correctly estimating the ambiguity for dual frequency receivers [60, 61].

The LAMBDA 3.0 software [62] includes the possibility to operate with partial estimation, i.e. Partial Ambiguity Resolution (PAR) with single frequency receivers.

3.3.3 TRIAD algorithm

As already mentioned, the focus of this work has been set on both loosely coupled approach based on the TRIAD algorithm and tight integration of line-of-sight information within a customized EKF. In particular, when the loosely coupled approach is adopted, two deputies are required in order to obtain a direct inertial- and magnetic-independent attitude information.

As far as the TRIAD algorithm is concerned, this is an analytical method to determine the rotation matrix between two reference frames. In particular, given two nonparallel reference unit vectors $\hat{V}_1$ and $\hat{V}_2$ in a primary reference frame and two corresponding observation unit vectors $\hat{W}_1$ and $\hat{W}_2$ represented with respect to a secondary frame, TRIAD starts defining two orthonormal triads of vectors $[\hat{r}_1, \hat{r}_2, \hat{r}_3]$ and $[\hat{o}_1, \hat{o}_2, \hat{o}_3]$ given by

$$\hat{r}_1 = \hat{V}_1, \hat{r}_2 = \frac{\hat{V}_1 \times \hat{V}_2}{|\hat{V}_1 \times \hat{V}_2|}, \hat{r}_3 = \hat{r}_1 \times \hat{r}_2 \tag{3.12}$$

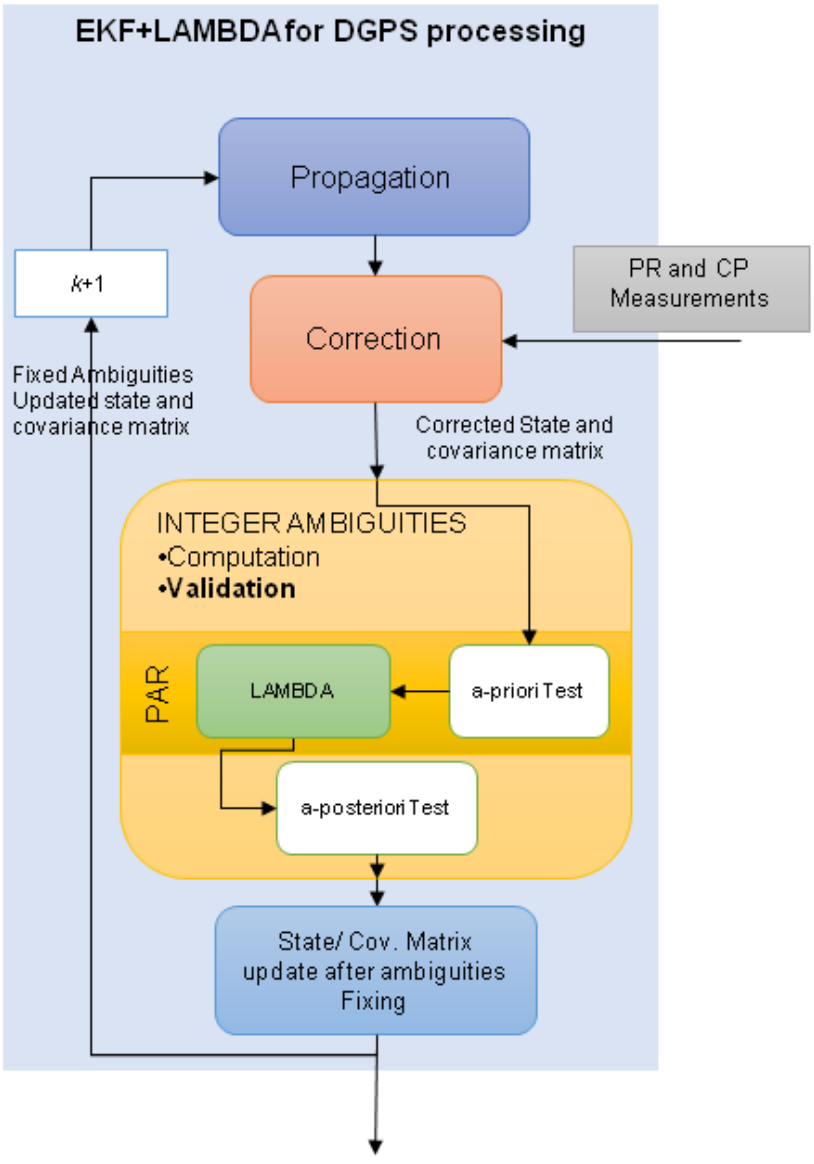

Figure 3.4: CDGPS EKF+LAMBDA flow chart.

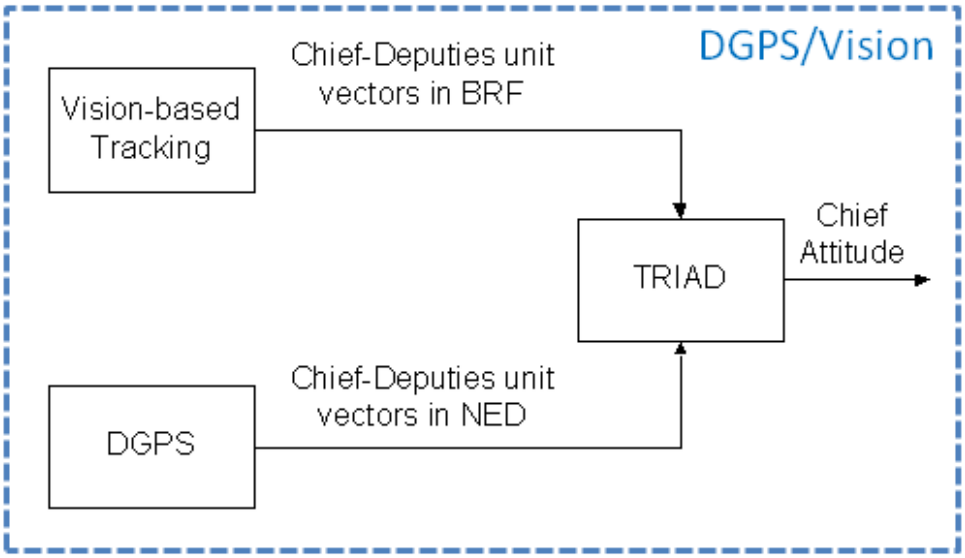

Figure 3.5: DGPS/Vision logical scheme.

$$\hat{o}_1 = \hat{W}_1, \hat{o}_2 = \frac{\hat{W}_1 \times \hat{W}_2}{|\hat{W}_1 \times \hat{W}_2|}, \hat{o}_3 = \hat{o}_1 \times \hat{o}_2 \tag{3.13}$$

and determines the unique orthogonal matrix $\underline{\underline{R}}$ which converts from the primary to the secondary reference frame as follows

$$\underline{\underline{R}} = \underline{\underline{M}}_{obs} \underline{\underline{M}}_{ref}^T \tag{3.14}$$

where $\underline{\underline{M}}_{obs} = [\hat{o}_1, \hat{o}_2, \hat{o}_3]$ and $\underline{\underline{M}}_{ref} = [\hat{r}_1, \hat{r}_2, \hat{r}_3]$ are 3 x 3 matrices.

As shown in Figure 3.5, the two vector pairs needed by the DGPS/Vision method to compute the attitude matrix are the chief-to-deputies BRF and NED unit vectors which are computed as explained in the previous sections. In particular, once the attitude is estimated by TRIAD, the estimate can be included as an additional measurement in a classical EKF-based aided navigation algorithm [9].

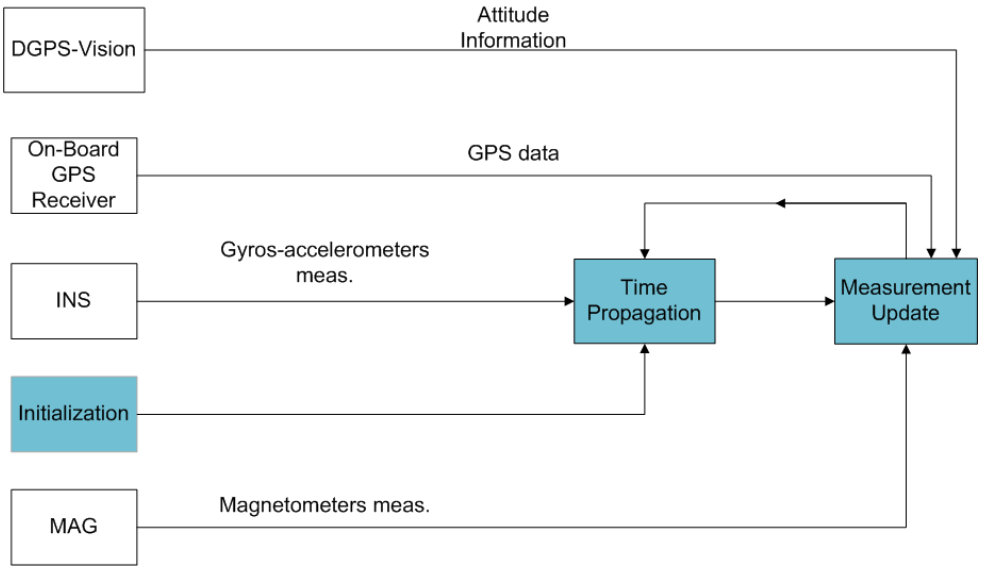

Figure 3.6: Extended Kalman Filter flow chart.

3.3.4 Extended Kalman Filter (EKF)

The core of the algorithm is the multi-sensor fusion approach which is based on augmenting a standard EKF for GPS/Inertial Navigation System (INS) integration (presented in [9]) with additional update measurements based on the proposed cooperative navigation concept.

The flow chart of the implemented filter is shown in Figure 3.6, where initialization, time propagation, and measurement update are highlighted.

In the following the filter structure and the two considered approaches (that is, loosely coupled and tightly coupled) are presented.

3.3.4.1 State vector

The state error vector $\delta\underline{x}$ comprises 9 components: the absolute position error vector $\delta\underline{p}$ expressed in geodetic coordinates (latitude error $\delta\phi$, longitude error $\delta\psi$, altitude error δh), the INS velocity error vector expressed in NED $\delta\underline{v}$ (North δv_n, East δv_e, Down δv_d), and the INS attitude error vector expressed in NED $\underline{\rho}$ (North ϵ_n, East ϵ_e, Down ϵ_d).

The state vector is thus

$$\delta\underline{x} = \begin{bmatrix} \delta\underline{p} \\ \delta\underline{v} \\ \underline{\rho} \end{bmatrix} \begin{matrix} \delta\underline{p} = [\delta\phi & \delta\psi & \delta h]^T \\ , \delta\underline{v} = [\delta v_n & \delta v_e & \delta v_d]^T \\ \underline{\rho} = [\epsilon_n & \epsilon_e & \epsilon_d]^T \end{matrix} \tag{3.15}$$

Within the EKF initialization phase, the nine initial conditions for the error state vector components and the associated covariance matrix are specified as

$$\delta\underline{\hat{x}}_0 = 0 \tag{3.16}$$

$$\underline{\underline{P}}_0 = E[\delta\underline{x}_0 \delta\underline{x}_0^T] \tag{3.17}$$

Initial covariance basically depends on the assumed accuracy for the onboard sensors, while the error state vector is re-initialized to zero after each measurement update.

3.3.4.2 System propagation

During the propagation phase, accelerometers and gyroscopes outputs are integrated through standard non linear INS mechanization equations expressed in the navigation frame [63]. This provides the reference trajectory and attitude used to define the linearized model for the navigation error

$$\begin{bmatrix} \delta\dot{\underline{p}} \\ \delta\dot{\underline{v}} \\ \dot{\underline{\rho}} \end{bmatrix} = \underline{\underline{F}} \begin{bmatrix} \delta\underline{p} \\ \delta\underline{v} \\ \underline{\rho} \end{bmatrix} + \begin{bmatrix} \underline{0}_{3x3} & \underline{0}_{3x3} \\ -\underline{\underline{R}}_b^n & \underline{0}_{3x3} \\ \underline{0}_{3x3} & -\underline{\underline{R}}_b^n \end{bmatrix} \begin{bmatrix} \delta\underline{f}^b \\ \delta\underline{\omega}_{ib}^b \end{bmatrix} \tag{3.18}$$

where $\underline{0}_{3x3}$ is the 3 x 3 null matrix, $\underline{\underline{R}}_b^n$ is the rotation matrix from the BRF to the NED reference frame, $\delta\underline{f}^b$ is the error vector of specific forces measured by the accelerometers and $\delta\underline{\omega}_{ib}^b$ is the error vector of angular rate measurements. The 9 x 9 continuous time system dynamic matrix $\underline{\underline{F}}$ is reported in Appendix A.

The error state covariance matrix $\underline{\underline{P}}_k$ (at time t_k) is propagated according to the following discrete-time equation

$$\underline{\underline{P}}_{k+1}^{-} = \underline{\underline{\Phi}}_k \underline{\underline{P}}_k \underline{\underline{\Phi}}_k^T + \underline{\underline{Q}}_{dk} \tag{3.19}$$

where $\underline{\underline{\Phi}}_k$ is the 9 x 9 discrete-time transition matrix that is given by $\underline{\underline{\Phi}}_k = e^{\underline{\underline{F}}\tau}$ with τ being the sampling time, and $\underline{\underline{Q}}_{dk}$ is the discrete-time process noise covariance matrix which models inertial errors and thus depends on the embarked gyroscopes and accelerometers.

3.3.4.3 Measurement update (Loosely Coupled)

In the loosely coupled approach, the measurement update phase takes place when GPS measurements and/or attitude estimates from the TRIAD algorithm are available. As already mentioned, this means that at least two deputies are required in order to derive the chief's attitude.

As regards DGPS/Vision, attitude estimates derived from TRIAD can be directly used in

$$\underline{\underline{R}}_n^b = \hat{\underline{\underline{R}}}_n^b (\underline{\underline{I}} - [\underline{\rho}\times]) \tag{3.20}$$

Equation 3.20 represents the transformation from the predicted attitude matrix ($\hat{\underline{\underline{R}}}_n^b$) to the attitude matrix computed using the TRIAD method ($\underline{\underline{R}}_n^b$), accurate to first order, where the skew-symmetric matrix $[\underline{\rho}\times]$ is expressed as

$$[\underline{\rho}\times] = \begin{bmatrix} 0 & -\epsilon_{DGPS/Vision,d} & \epsilon_{DGPS/Vision,e} \\ \epsilon_{DGPS/Vision,d} & 0 & -\epsilon_{DGPS/Vision,n} \\ -\epsilon_{DGPS/Vision,e} & \epsilon_{DGPS/Vision,n} & 0 \end{bmatrix} \tag{3.21}$$

Thus, when all the information sources are available, the measurement residual vector, representing the difference between the actual measurements (GPS pseudoranges, DGPS/Vision attitude, magnetometer-based heading) and the measurements predicted on the basis of the propagated state vector, can be

written as

$$\delta\underline{y} = \begin{bmatrix} \delta PR_1 \\ \cdots \\ \delta PR_n \\ \epsilon_{DGPS/Vision,n} \\ \epsilon_{DGPS/Vision,e} \\ \epsilon_{DGPS/Vision,d} \\ \epsilon_{mag,d} \end{bmatrix} \tag{3.22}$$

where δPR_s is the pseudorange measurement residual for the s-th satellite computed as the difference between the measured range for the s-th satellite and a pivot satellite, minus the predicted difference (n measurements are available if $n+1$ satellites are in view), $\epsilon_{DGPS/Vision,n}$, $\epsilon_{DGPS/Vision,e}$ and $\epsilon_{DGPS/Vision,d}$ are the attitude measurement residuals relevant to DGPS/Vision, and $\epsilon_{mag,d}$ is the observation residual relevant to magnetic heading measurement.

As a consequence the linearized observation model at time t_k is

$$\delta\underline{y} = \underline{\underline{H}}_k \delta\underline{x} \tag{3.23}$$

where

$$\underline{\underline{H}}_k = \begin{bmatrix} \underline{\underline{H}}_n & \underline{\underline{0}}_{n\times 3} & \underline{\underline{0}}_{n\times 3} \\ \underline{\underline{0}}_{3\times 3} & \underline{\underline{0}}_{3\times 3} & \underline{\underline{I}}_3 \\ \underline{0} & \underline{0} & \begin{bmatrix} 0 & 0 & 1 \end{bmatrix} \end{bmatrix} \tag{3.24}$$

$\underline{0}$ is a 1×3 null elements vector, $\underline{\underline{0}}_{n\times 3}$ is a $n \times 3$ null matrix, $\underline{\underline{I}}_3$ is a 3×3 identity matrix and

$$\underline{\underline{H}}_n = \begin{bmatrix} \underline{h}_1 \underline{\underline{R}}_n^e \underline{\underline{D}} \\ \cdots \\ \underline{h}_n \underline{\underline{R}}_n^e \underline{\underline{D}} \end{bmatrix} \tag{3.25}$$

is an $n \times 3$ matrix, where $\underline{h}_s$ is the difference between the two line-of-sight vectors in the ECEF reference frame, one from the s-th GPS satellite to the vehicle and the other from the pivot satellite to the vehicle, $\underline{\underline{R}}_n^e$ is the rotation

matrix from the navigation frame to ECEF, and $\underline{\underline{D}}$ is the matrix converting polar coordinates to linear coordinates within the navigation frame.

The number of components of the measurement residual vector given in Equation 3.22 is properly reduced at time instants when measurements from a subset of sensors are available (for example, pseudoranges only) or it is reduced to accommodate only attitude measurements coming from DGPS/Vision, when the DGPS/Vision heading accuracy excludes the need of integrating magnetometer data.

When measurements are available, the navigation state is corrected according to

$$\delta \underline{x}_{corr} = \underline{\underline{K}}_k \delta \underline{y} \tag{3.26}$$

where the Kalman gain $\underline{\underline{K}}_k$ is given by

$$\underline{\underline{K}}_k = \underline{\underline{P}}_k^- \underline{\underline{H}}_k^T (\underline{\underline{H}}_k \underline{\underline{P}}_k^- \underline{\underline{H}}_k^T + \underline{\underline{R}}_k)^{-1} \tag{3.27}$$

and the measurement noise covariance matrix $\underline{\underline{R}}_k$ is

$$\underline{\underline{R}}_k = \begin{bmatrix} \underline{\underline{R}}_{GPS} & \underline{\underline{0}}_{n\times 3} \\ \underline{\underline{0}}_{3\times n} & \underline{\underline{R}}_k^{DGPS/Vision} \\ \underline{0}_{1\times n} & \begin{bmatrix} 0 & 0 & \sigma^2_{\epsilon_{mag,d}} \end{bmatrix} \end{bmatrix} \tag{3.28}$$

where $\underline{\underline{0}}$ are null matrices which dimensions are reported in the subscripts, $\sigma^2_{\epsilon_{mag,d}}$ is the variance relevant to magnetic heading measurement, $\underline{\underline{R}}_{GPS}$ is the $n\times n$ GPS measurement covariance matrix and $\underline{\underline{R}}_k^{DGPS/Vision}$ is the 3×3 DGPS/Vision attitude measurement covariance matrix at time t_k.

In particular, $\underline{\underline{R}}^{GPS}$ is given by

$$\underline{\underline{R}}^{GPS} = \begin{bmatrix} 2 & 1 & 1 & \cdots & 1 \\ 1 & 2 & 1 & \cdots & 1 \\ \vdots & \vdots & \vdots & \ddots & \vdots \\ 1 & 1 & 1 & \cdot & 2 \end{bmatrix} \sigma^2_{PR} \tag{3.29}$$

where σ^2_{PR} is the variance of the measurement noise for the pseudorange measurements, and $\underline{\underline{R}}_k^{DGPS/Vision}$ is

$$\underline{\underline{R}}_k^{DGPS/Vision} = \begin{bmatrix} \sigma^2_{k,\epsilon_{DGPS,Vision,n}} & 0 & 0 \\ 0 & \sigma^2_{k,\epsilon_{DGPS,Vision,e}} & 0 \\ 0 & 0 & \sigma^2_{k,\epsilon_{DGPS,Vision,d}} \end{bmatrix} \tag{3.30}$$

where $\sigma^2_{k,\epsilon_{DGPS,Vision,n}}$, $\sigma^2_{k,\epsilon_{DGPS,Vision,e}}$ and $\sigma^2_{k,\epsilon_{DGPS,Vision,d}}$ are the variances relevant to the DGPS/Vision attitude measurements (at time t_k).

As shown above, $\underline{\underline{R}}_k$ depends on magnetometers and pseudorange uncertainties, which can be assumed to be constant during the flight, and on TRIAD attitude estimation errors which need to be updated on the basis of the formation geometry.

In our case, the "classical" TRIAD covariance matrix, whose analytical expression is reported in [64], cannot be used, due to the fact that the derivation is based on the assumption that line of sight errors have an axially symmetric distribution around the respective unit vector. In fact, as shown in [49] the DGPS line-of-sight error in NED does not have an axially symmetric distribution, due to the difference in GPS performance between the horizontal plane and the vertical direction. Consequently, the solution adopted to obtain TRIAD attitude estimation uncertainties, has been to build up look up tables based on numerical simulations carried out for different formation geometries [11]. To this end, for a given chief attitude and formation geometry, DGPS and optical measurements are simulated by random extractions, and the resulting attitude measurement error is analyzed with statistical tools.

3.3.4.4 Measurement update (Tightly Coupled)

In this section, the focus is only set on the tight integration of DGPS/Vision measurements within the EKF.

Considering the generic i-th deputy, the vision-based tracking algorithm provides chief to deputy unit vectors in BRF ($\hat{r}_i^{BRF}$), while the DGPS provides chief to i-th deputy unit vectors in NED ($\hat{r}_i^{NED}$). They are related through the equation

$$\hat{r}_i^{BRF} = \underline{\underline{R}}_n^b \hat{r}_i^{NED} \tag{3.31}$$

where $\underline{\underline{R}}_n^b$ is the current (true) attitude matrix. To first order, $\underline{\underline{R}}_n^b$ is related to the estimated attitude matrix ($\underline{\underline{\tilde{R}}}_n^b$) by

$$\underline{\underline{\tilde{R}}}_n^b = \underline{\underline{R}}_n^b (\underline{\underline{I}} + [\underline{\rho}\times]) \tag{3.32}$$

where $\underline{\underline{I}}$ is the identity matrix and $[\underline{\rho}\times]$ is reported in Equation 3.21.

From Equation 3.31 and Equation 3.32 it is thus possible to write

$$\hat{r}_i^{BRF} = \underline{\underline{\tilde{R}}}_n^b (\underline{\underline{I}} - [\underline{\rho}\times]) \hat{r}_i^{NED} \tag{3.33}$$

Considering that for a generic vector $\underline{u}$

$$\underline{\rho} \times \underline{u} = [\underline{\rho}\times]\underline{u} = -[\underline{u}\times]\underline{\rho} \tag{3.34}$$

exchanging the order of the vector cross product terms in Equation 3.33, the following is obtained

$$\hat{r}_i^{BRF} - \underline{\underline{\tilde{R}}}_n^b \hat{r}_i^{NED} = \underline{\underline{\tilde{R}}}_n^b [\hat{r}_i^{NED}\times]\underline{\rho} = \underline{\underline{H}}_{DGPS/Vision,i}\underline{\rho} \tag{3.35}$$

which can be re-written as

$$\delta \underline{z}_{DGPS/Vision,i} = \underline{\underline{H}}_{DGPS/Vision,i}\underline{\rho} \tag{3.36}$$

where the residual ($\delta \underline{z}_{DGPS/Vision,i}$) is

$$\delta \underline{z}_{DGPS/Vision,i} = \hat{r}_i^{BRF} - \underline{\underline{\tilde{R}}}_n^b \hat{r}_i^{NED} \tag{3.37}$$

and the measurement matrix is given by

$$\underline{\underline{H}}_{DGPS/Vision,i} = \underline{\underline{\tilde{R}}}_n^b [\hat{r}_i^{NED}\times] \tag{3.38}$$

As far as the covariance matrix $\underline{\underline{R}}_{DGPS/Vision,i}$ is concerned, assuming uncorrelated DGPS and electro-optical errors, this can be estimated as

$$\underline{\underline{R}}_{DGPS/Vision,i} = \underline{\underline{R}}_{DGPS,i} + \underline{\underline{R}}_{Vision,i} \tag{3.39}$$

$\underline{\underline{R}}_{Vision,i}$ is obtained by first writing the unit vector covariance matrix in the Camera Reference Frame

$$\underline{\underline{R}}_{Vision,i,CRF} = \begin{bmatrix} \sigma^2_{x_{Vision,CRF,i}} & \sigma_{xy_{Vision,CRF,i}} & \sigma_{xz_{Vision,CRF,i}} \\ \sigma_{xy_{Vision,CRF,i}} & \sigma^2_{y_{Vision,CRF,i}} & \sigma_{yz_{Vision,CRF,i}} \\ \sigma_{xz_{Vision,CRF,i}} & \sigma_{yz_{Vision,CRF,i}} & \sigma^2_{z_{Vision,CRF,i}} \end{bmatrix} \tag{3.40}$$

with

$$\begin{aligned} \sigma^2_{x_{Vision,CRF,i}} &= \left(\frac{\partial \hat{r}^{CRF}_{x,i}(Az_{CRF,i}, El_{CRF,i})}{\partial Az_{CRF}} \right)^2 \sigma^2_{Az_{CRF}} + \cdots \\ &\quad \left(\frac{\partial \hat{r}^{CRF}_{x,i}(Az_{CRF,i}, El_{CRF,i})}{\partial El_{CRF}} \right)^2 \sigma^2_{El_{CRF}} \\ \sigma_{xy_{Vision,CRF,i}} &= \left(\frac{\partial \hat{r}^{CRF}_{x,i}(Az_{CRF,i}, El_{CRF,i})}{\partial Az_{CRF}} \right) \cdots \\ &\quad \left(\frac{\partial \hat{r}^{CRF}_{y,i}(Az_{CRF,i}, El_{CRF,i})}{\partial Az_{CRF}} \right) \sigma^2_{Az_{CRF}} + \cdots \\ &\quad \left(\frac{\delta \hat{r}^{CRF}_{x,i}(Az_{CRF,i}, El_{CRF,i})}{\partial El_{CRF}} \right) \cdots \\ &\quad \left(\frac{\partial \hat{r}^{CRF}_{y,i}(Az_{CRF,i}, El_{CRF,i})}{\partial El_{CRF}} \right) \sigma^2_{El_{CRF}} \end{aligned} \tag{3.41}$$

and so on for the other entries, and then propagating uncertainties through Equation 3.4 as follows

$$\underline{\underline{R}}_{Vision,i} = \underline{\underline{R}}^b_c \underline{\underline{R}}_{Vision,i,CRF} (\underline{\underline{R}}^b_c)^T \tag{3.42}$$

where $\underline{\underline{R}}^b_c$ is the (known) rotation matrix from camera to body reference frame. In the above relations, $\sigma_{Az_{CRF}}$ and $\sigma_{El_{CRF}}$ can be assumed equal to camera IFOV.

As concerns $\underline{\underline{R}}_{DGPS,i}$, the starting point for the derivation is given by the assumed uncertainties on the baseline NED components. As an example, typical horizontal and vertical accuracy for a given DGPS processing approach can be considered, or current satellites number and dilution of precision conditions can be exploited to have a more refined estimate. Code-based or carrier-phase based DGPS will of course provide different uncertainty values.

Let us call $\sigma_{N,i}$, $\sigma_{E,i}$, $\sigma_{D,i}$ the baseline components uncertainties, and let us assume them uncorrelated.

Considering the chief-to-(i-th) deputy DGPS baseline in NED $\Delta\underline{r}_i^{NED} = \underline{\underline{R}}_e^n \Delta\underline{r}_i^{ECEF}$ whose components are $(x_{n,i}, x_{e,i}, x_{d,i})$ the chief-to-deputy unit vector components are given by

$$\hat{r}_i^{NED} = \begin{bmatrix} \dfrac{x_{n,i}}{\sqrt{x_{n,i}^2 + x_{e,i}^2 + x_{d,i}^2}} \\ \dfrac{x_{e,i}}{\sqrt{x_{n,i}^2 + x_{e,i}^2 + x_{d,i}^2}} \\ \dfrac{x_{d,i}}{\sqrt{x_{n,i}^2 + x_{e,i}^2 + x_{d,i}^2}} \end{bmatrix} \tag{3.43}$$

DGPS unit vector uncertainties in NED are thus given by

$$\underline{\underline{R}}_{DGPS,i,NED} = \underline{\underline{J}} \begin{bmatrix} \sigma_{N,i}^2 & 0 & 0 \\ 0 & \sigma_{E,i}^2 & 0 \\ 0 & 0 & \sigma_{D,i}^2 \end{bmatrix} \underline{\underline{J}}^T \tag{3.44}$$

where

$$\underline{\underline{J}} = \begin{bmatrix} \dfrac{\partial \hat{r}_x^{NED}(\Delta r_i^{NED})}{\partial x_n} & \dfrac{\partial \hat{r}_x^{NED}(\Delta r_i^{NED})}{\partial x_e} & \dfrac{\partial \hat{r}_x^{NED}(\Delta r_i^{NED})}{\partial x_d} \\ \dfrac{\partial \hat{r}_y^{NED}(\Delta r_i^{NED})}{\partial x_n} & \dfrac{\partial \hat{r}_y^{NED}(\Delta r_i^{NED})}{\partial x_e} & \dfrac{\partial \hat{r}_y^{NED}(\Delta r_i^{NED})}{\partial x_d} \\ \dfrac{\partial \hat{r}_z^{NED}(\Delta r_i^{NED})}{\partial x_n} & \dfrac{\partial \hat{r}_z^{NED}(\Delta r_i^{NED})}{\partial x_e} & \dfrac{\partial \hat{r}_z^{NED}(\Delta r_i^{NED})}{\partial x_d} \end{bmatrix} \tag{3.45}$$

And to rotate it in BRF we have to use the estimated attitude matrix as follows

$$\underline{\underline{R}}_{DGPS,i} = \underline{\underline{\tilde{R}}}^{b}_{n} \underline{\underline{R}}_{DGPS,i,NED} (\underline{\underline{\tilde{R}}}^{b}_{n})^{T} \tag{3.46}$$

Considering the full residual measurement vector for the EKF $\delta\underline{z}$, when all measurements (pseudoranges, DGPS/Vision, and magnetometers) are available and used, it is given by

$$\delta\underline{z} = \begin{bmatrix} \delta PR_1 \\ \cdots \\ \delta PR_n \\ \delta z_{DGPS/Vision,1,1} \\ \delta z_{DGPS/Vision,2,2} \\ \delta z_{DGPS/Vision,3,3} \\ \cdots \\ \delta z_{DGPS/Vision,nd,1} \\ \delta z_{DGPS/Vision,nd,1} \\ \delta z_{DGPS/Vision,nd,1} \\ \epsilon_{mag,d} \end{bmatrix} = \underline{\underline{H}}_{k} \delta\underline{x} \tag{3.47}$$

where:

- nd: DGPS/Vision vector residuals are available, being nd the number of deputies in view;

- $\epsilon_{mag,d}$ is the scalar measurement residual relevant to magnetic heading measurement;

- $\underline{\underline{H}}_{k}$ is the measurement matrix given by

$$\underline{\underline{H}}_{k} = \begin{bmatrix} \underline{\underline{H}}_{n} & \underline{\underline{0}}_{n\times 3} & \underline{\underline{0}}_{n\times 3} \\ \underline{\underline{0}}_{3nd\times 3} & \underline{\underline{0}}_{3nd\times 3} & \underline{\underline{H}}_{DGPS/Vision} \\ \underline{0} & \underline{0} & \begin{bmatrix} 0 & 0 & 1 \end{bmatrix} \end{bmatrix} \tag{3.48}$$

in which $\underline{0}$ is a 1×3 null elements vector, $\underline{\underline{0}}_{n\times 3}$ is the $n \times 3$ null matrix, $\underline{\underline{I}}_3$ is a 3×3 identity matrix, $\underline{\underline{H}}_n$ is given by Equation 3.25 and

$$\underline{\underline{H}}_{DGPS/Vision} = \begin{bmatrix} \underline{\underline{H}}_{DGPS/Vision,1} \\ \cdots \\ \underline{\underline{H}}_{DGPS/Vision,nd} \end{bmatrix} = \begin{bmatrix} \underline{\underline{\tilde{R}}}_n^b [\hat{r}_1^{NED} \times] \\ \cdots \\ \underline{\underline{\tilde{R}}}_n^b [\hat{r}_{nd}^{NED} \times] \end{bmatrix}_{3nd\times 3} \tag{3.49}$$

The full measurement covariance matrix is given by

$$\underline{\underline{R}}_k = \begin{bmatrix} \underline{\underline{R}}_{n\times n}^{GPS} & \underline{\underline{0}}_{n\times 3nd} & \underline{0}_{n\times 1} \\ \underline{\underline{0}}_{3nd\times n} & \underline{\underline{R}}_{3nd\times 3nd}^{DGPS/Vision} & \underline{0}_{3nd\times 1} \\ \underline{0}_{1\times n} & \underline{0}_{1\times 3nd} & \sigma^2_{\epsilon_{mag,d}} \end{bmatrix} \tag{3.50}$$

with

$$\underline{\underline{R}}_{3nd\times 3nd}^{DGPS/Vision} = \begin{bmatrix} \underline{\underline{R}}_{DGPS/Vision,1} & & \underline{\underline{0}} \\ & \cdots & \\ \underline{\underline{0}} & & \underline{\underline{R}}_{DGPS/Vision,nd} \end{bmatrix} \tag{3.51}$$

Measurement update phase is carried out using standard Kalman filtering equations, i.e., when measurements are available, the navigation state and the error state covariance matrix P_k^+ are corrected according to

$$\delta \underline{x}_{update} = \underline{\underline{K}}_k \delta \underline{z} \tag{3.52}$$

and

$$\underline{\underline{P}}_k^+ = (\underline{\underline{I}} - \underline{\underline{K}}_k \underline{\underline{H}}_k) \underline{\underline{P}}_k^- \tag{3.53}$$

where the Kalman gain $\underline{\underline{K}}_k$ is given by Equation 3.27.

Also in this case, as in the loosely coupled approach, magnetic measurements are used in the update phase only if the current value of the (9,9) entry of the error state covariance matrix is above a threshold.

3.4 DGPS/Vision potential and trade-offs

The key concept of the considered architecture is to complement a navigation filter that integrates single vehicle-based measurements with additional information provided by the distributed nature of the formation. This permits to overcome onboard inertial sensors shortcomings thanks to the availability of magnetic- and inertial-independent attitude information. In fact, while DGPS processing is used to estimate the baseline vectors between the chief and the deputies in a stabilized NED reference frame, vision-based processing allows camera(s) embarked on the chief to detect and track deputies, thus providing LOS information in CRF.

If we assume that the rotation matrix between CRF and BRF is known with negligible uncertainty, it can be used to convert LOS information from CRF into BRF. This can happen both for strapdown (constant rotation matrix) and gimbaled installation (variable rotation matrix) provided that accurate off-line alignment is carried out, and gimbal rotation angles are accurately estimated.

As already mentioned, knowledge of chief-to-deputies unit vectors in both NED and BRF contains attitude information whose uncertainty depends on DGPS and vision accuracy, and on the actual formation geometry.

Basic trade-offs and performance bounds for DGPS/Vision processing can be understood by a straightforward analytical approach, if we assume a simplified geometry. Let us consider a horizontal 2-vehicle formation with the deputy separated from the chief by a given baseline L along North direction. Let us also assume that chief attitude angles (heading, pitch and roll) are all null. Being the chief-to-deputy LOS along the roll axis, it only provides information related to heading and pitch angles. At a first level of approximation, if the baseline is large enough, angular uncertainties of differential GPS estimates are given by

$$\sigma_{DGPS,angle,hor} \cong 2 \arctan\left(\frac{\sigma_{DGPS,lin,hor}}{2L\sqrt{2}}\right) \tag{3.54}$$

$$\sigma_{DGPS,angle,vert} \cong 2 \arctan\left(\frac{\sigma_{DGPS,lin,vert}}{2L}\right) \tag{3.55}$$

assuming that the DGPS error distribution is the same in all horizontal directions. By simply considering the camera geometric resolution, and assuming a square detector, the camera IFOV at a distance L covers an area LIFOV x LIFOV on the scene where LIFOV is given by

$$L_{IFOV} \cong 2L \tan\left(\frac{IFOV}{2}\right) \tag{3.56}$$

This parameter influences the dimensions of the target that can be reliably tracked. Then, heading and pitch uncertainty can be estimated combining DGPS and vision uncertainties in horizontal and vertical dimensions:

$$\sigma_{heading} \cong \sqrt{\sigma^2_{DGPS,angle,hor} + IFOV^2} \tag{3.57}$$

$$\sigma_{pitch} \cong \sqrt{\sigma^2_{DGPS,angle,vert} + IFOV^2} \tag{3.58}$$

Using typical differential GPS uncertainties (1 m horizontal and 2 m vertical error for code-based DGPS, 0.02 and 0.04 m for CDGPS) and realistic camera IFOVs (from 0.02° to 0.1°), we get the results shown in Figure 3.7.

These diagrams show that a baseline of the order of 100 m is needed for sub-degree attitude estimation when using DGPS, with the potential of very fine accuracy increasing the baseline or adopting CDGPS.

The LIFOV diagram shows that these baselines are compatible with typical angular resolutions and vehicle dimensions encountered in small UAVs. When DGPS/CDGPS errors tend to vanish, it is the camera IFOV that bounds the attitude error from below.

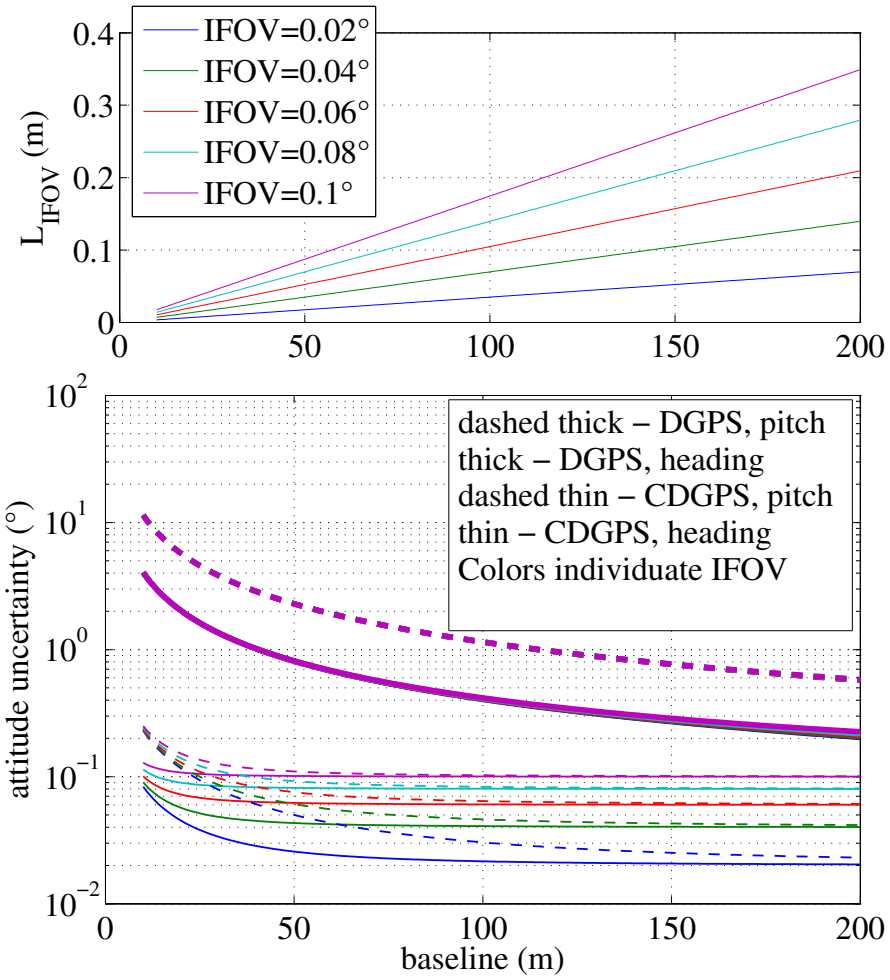

Figure 3.7: Basic trade-offs and performance limits for DGPS/Vision based attitude estimation.

3.5 Testing and Validation Strategy

Within this research activity, several experimental tests have been performed during which data have been gathered from different sensors and platforms in order to evaluate the performance of the developed DGPS/Vision concepts.

3.5.1 Experimental Setup

Tests have been conducted with two different experimental setups in which

1. two fixed ground antennas have been used as surrogate deputy vehicles;
2. a multirotor vehicle has played the role of flying deputy, while two fixed ground antennas have been adopted as surrogate deputy vehicle and Ground Control Point (GCP).

During all these tests the chief vehicle has been a Pelican from Ascending Technologies (Figure 3.8). In particular, the Pelican quadrotor, besides being equipped with a controller, a set of onboard sensors (Table 3.1) and an onboard computer (AscTec Mastermind, Ascending Technologies), has been customized with a miniaturized 752×480 electro optical sensor (BlueFox MLC200wC, Matrix Vision) and an additional uBlox GPS Receiver (LEA 6T, uBlox) which provides raw measurements that are used in the DGPS processing.

The additional GPS receiver and the optical sensor have been connected to the Mastermind computer via a Universal Serial Bus (USB) link, while other raw and calibrated/processed sensor data are gathered via the Universal Asynchronous Receiver-Transmitter (UART) connection between Mastermind and autopilot.

The acquisition software that runs on the Mastermind has been coded in C/C++ and gathers all the necessary data with an accurate time-tag based on GPS time and the Central Processing Unit (CPU) clock. In particular, IMU

Figure 3.8: Chief vehicle (Customized Ascending Technologies Pelican).

data are acquired with the aid of the Asctec Communication Interface (ACI) at a frequency of 100 Hz while images and GPS raw data are gathered simultaneously at a frequency of 1 Hz.

As regards deputies, tests have been conducted by using two ground stations equipped with an AV59 antenna (Trimble) and BD960 receiver (Trimble) (Figure 3.9) which acted as surrogate deputies, and a computer which is used to save all GPS raw data as it is done on the chief vehicle. BD960 is a dual frequency

Table 3.1: Pelican Navigation Sensors.

Component	**Model**
Gyroscopes	Analog Devices ADXRS610
Accelerometer	Memsic R9500
Barometer	NXP MPXA6115A
Compass	Honeywell HMC5843
PS Receiver	uBlox LEA-6S

receiver, however only L1 signals have been taken into account.

The hardware architecture for the first set of tests is shown in Figure 3.10.

The second set of tests has been conducted in an outdoor area, in which a customized version of the 3DR X8+ multirotor has been used as flying deputy (Figure 3.11). The X8+ has been equipped with an auxiliary GPS system (the same installed on the chief vehicle) and an Odroid XU4 embedded CPU for data processing and storage. In addition, the two ground antennas/receivers have been used as fixed deputies and/or GCP. As a consequence, in addition to the hardware architecture shown in Figure 3.10, a flying deputy is introduced into the experimental setup (Figure 3.12)

3.5.2 Flight Tests

The first set of tests has been carried out in an outdoor area that allows baselines among chief and deputies of the order of 100 meters. As noted above, this is necessary to reduce the DGPS angular error and, thus, improve attitude determination accuracy.

These tests have been designed to compare DGPS/Vision estimates with heading measurements based on the onboard magnetometers and the output of the real time data fusion algorithm running on Pelican autopilot, based on a filter which combines accelerometers, gyroscopes and magnetometers. In particular, among the flights that have been conducted, two tests have been chosen as representative of attitude dynamics and varying formation geometry, as follows

Test 1 an almost constant horizontal formation geometry (Figure 3.13) has been kept, with a baseline between the two deputies of the order of 40 meters, and the chief at a distance slightly larger than 100 meters from the two ground antennas (Figure 3.14). A number of attitude maneuvers has been commanded, including four 360° heading rotations and 1 Hz heading

Figure 3.9: Ground antennas/receivers used as deputy vehicles.

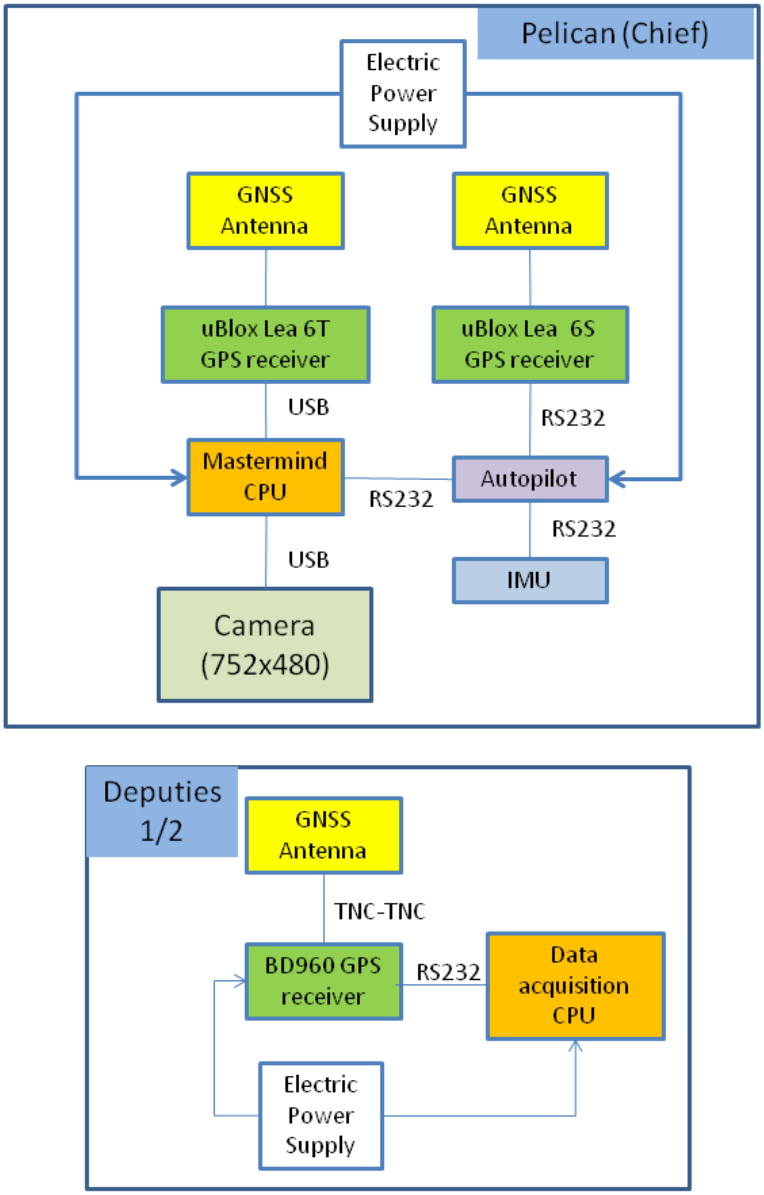

Figure 3.10: Hardware Architecture (first experiments).

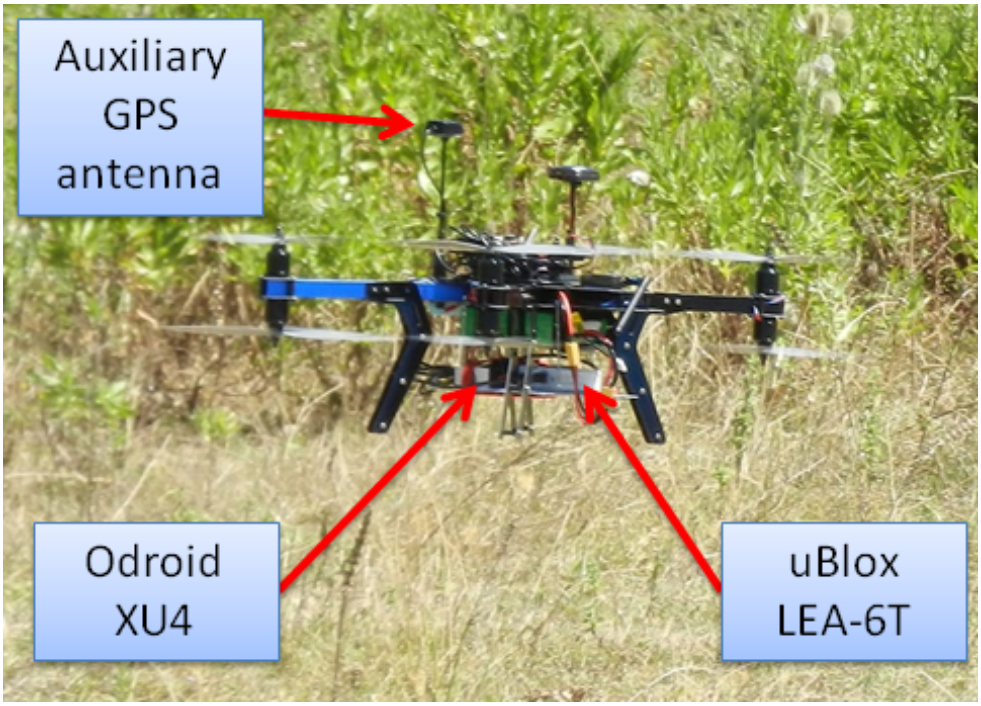

Figure 3.11: Customized X8+ multirotor (flying deputy).

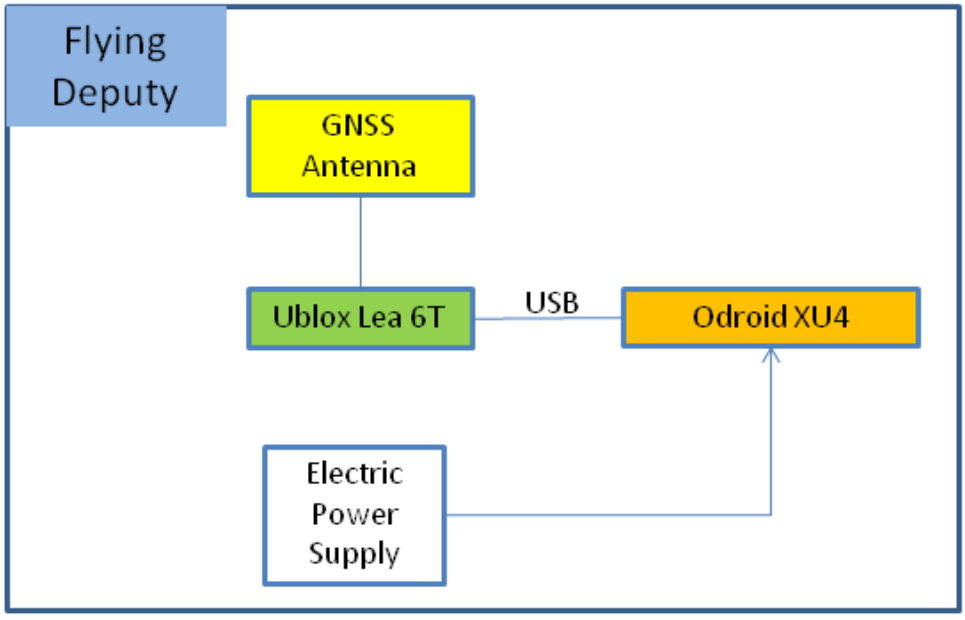

Figure 3.12: Additional Hardware (Test 3).

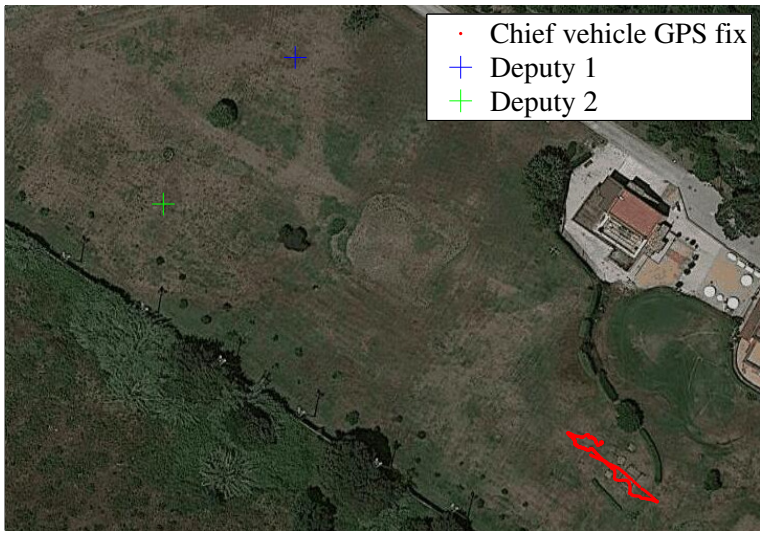

Figure 3.13: Formation geometry Test 1.

oscillation with about 30° amplitude. This test has been selected to point out the different levels of robustness of onboard fusion and DGPS/Vision with respect to flight dynamics history.

Test 2 the chief vehicle has been commanded to fly along a path of about 200 meters (Figure 3.15), thus generating a significant change of formation geometry in NED coordinates. The two ground antennas have been positioned in order to provide a baseline of about 100 meters with respect to the chief vehicle at the starting and end point of the flight path (Figure 3.16). This test has been selected to point out the effects on the onboard filter and on DGPS/Vision estimates of both flight dynamics history and magnetic effects.

The second set of tests has been performed in an outdoor area where the two ground antennas, the X8+, and the Pelican have been involved. During these tests, both DGPS strategies (namely CDGPS and code-based DGPS) have been

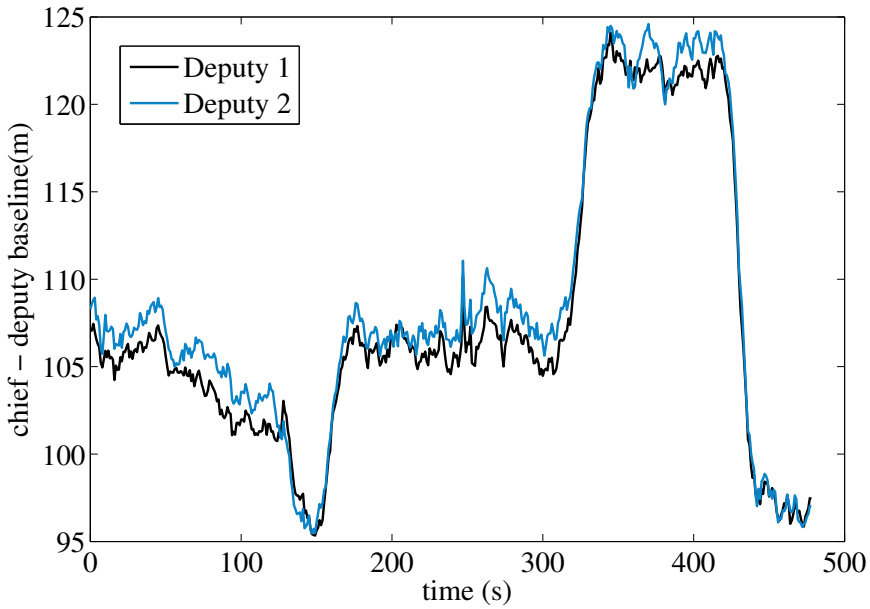

Figure 3.14: Chief-deputies baselines Test 1.

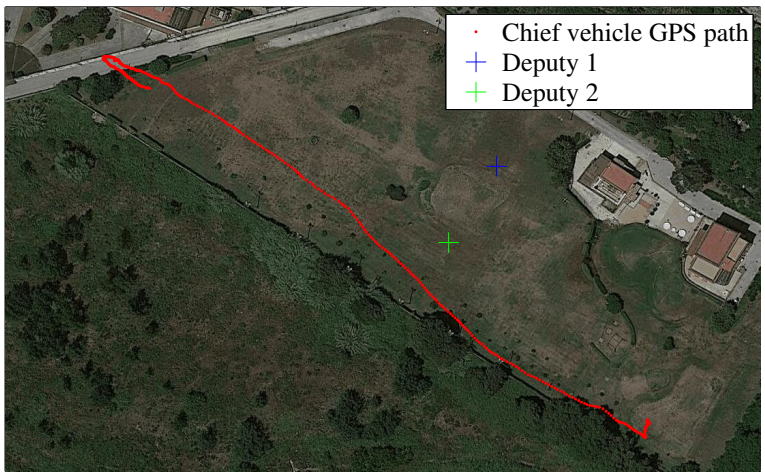

Figure 3.15: Formation geometry Test 2.

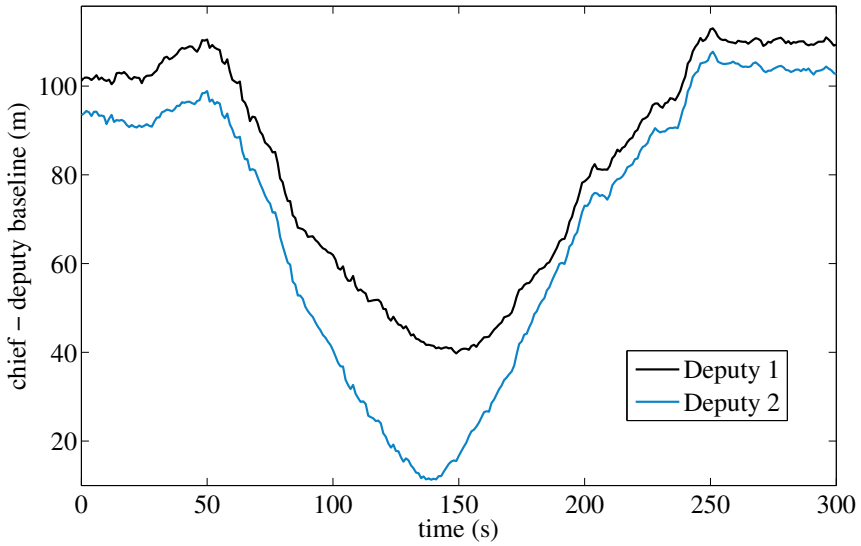

Figure 3.16: Chief-deputies baselines Test 2.

adopted, and the estimated attitude has been compared with the one given by the Pelican navigation filter.

Among different tests, one has been considered in order to show the potential of the developed approach in terms of accuracy and capability to provide drift-free estimates, as follows

Test 3 an almost horizontal formation geometry (Figure 3.17) has been kept during a flight of about 500 seconds, during which the Pelican was commanded to perform heading rotation maneuvers with different rates. In fact, several fast 360° heading rotations have been commanded while most of the flight was characterized by slow heading rotations in order to keep the deputies within the chief camera FOV. Baselines variation is shown in Figure 3.18, where the maximum baseline length between the chief (Pelican) and the flying deputy (X8+) is of about 130 meters, while, the maximum baseline lengths of the fixed deputy and the GCP with respect to the pelican are both of about 160 meters. During this test, the flying deputy

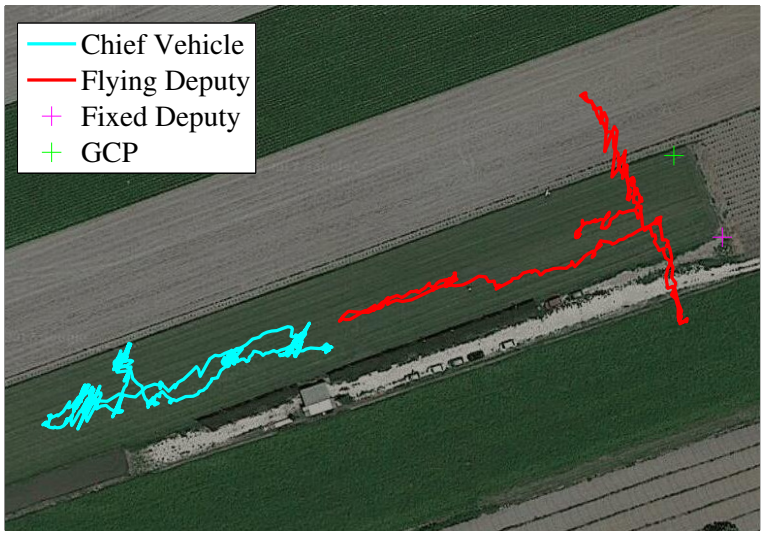

Figure 3.17: Formation geometry Test 3.

vehicle (X8+) and the fixed deputy (ground antenna) are exploited to obtain attitude information, whereas the second ground antenna is used as GCP in order to have a benchmark to evaluate the accuracy of the proposed approach.

3.5.3 Pointing/Attitude Accuracy Evaluation Strategy

Given the sub-degree attitude determination accuracy obtained by the DGPS/Vision method for the baselines experimented during flight tests, in particular for the heading angle, it is nontrivial to find a reference measurement that provides a ground truth of better accuracy level. In fact, this level of accuracy can be reached installing a tactical grade IMU on board the Pelican, or a dual antenna navigation system [16, 65], or using very accurately geoferenced ground control points.

Besides the high cost, dual antenna navigation systems have a significant

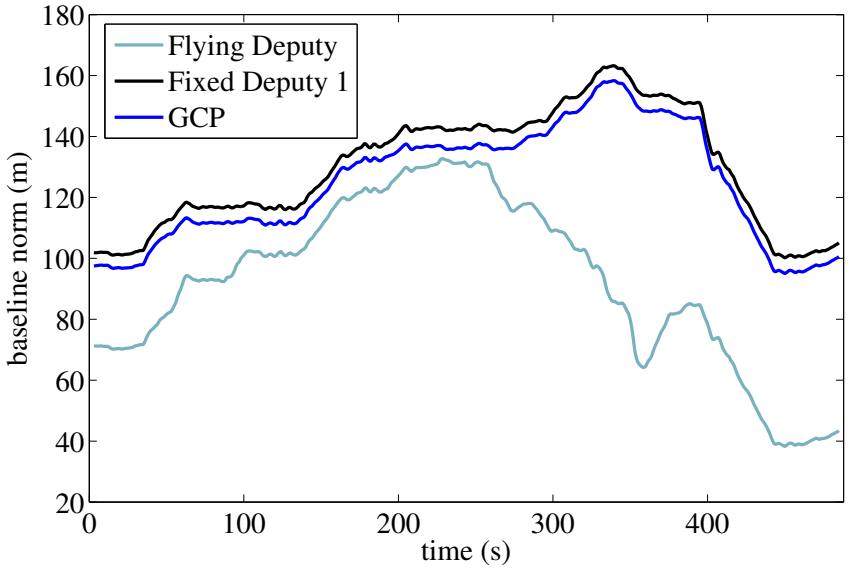

Figure 3.18: Chief-deputies baselines Test 3.

limit related to the necessity to install the two antennas with a sufficiently large baseline (1 meter or more), which is hard to obtain onboard the Pelican. Also tactical grade IMUs represent a non-optimal solution due to the high cost and weight.

To this end, two similar strategies have been adopted in order to evaluate the DGPS/Vision attitude accuracy.

- In Test 1, the position of a GCP which is visible in the acquired images (Figure 3.19) has been identified on an open source 1:1000 georeferenced map [66] (planar error of the order of 25 to 50 cm). The idea is to compute azimuth and elevation in the navigation frame of the identifiable GCP, to be used as reference measurements to evaluate the pointing accuracy.

- In Test 3, a ground-based GPS antenna has been used as GCP (Figure 3.20) for pointing accuracy evaluation, which can then be related to attitude determination performance.

The logical scheme of the pointing accuracy, when the GPS antenna is used as GCP, is reported in Figure 3.21 where the main processing steps are highlighted.

The main difference between the two validation strategies is the adopted approach for the evaluation of the (attitude independent) reference measurements, that is, the ECEF relative position vector $\Delta\underline{r}^{ECEF}$ between the Pelican and the GCP.

In fact, in the first approach, this vector is evaluated as the difference between the Pelican and the georeferenced GCP positions (Figure 3.22)

$$\Delta\underline{r}^{ECEF} = \begin{bmatrix} x_{GCP}^{ECEF} - x_{Pelican}^{ECEF} \\ y_{GCP}^{ECEF} - y_{Pelican}^{ECEF} \\ z_{GCP}^{ECEF} - z_{Pelican}^{ECEF} \end{bmatrix} = \begin{bmatrix} \Delta x \\ \Delta y \\ \Delta z \end{bmatrix} \tag{3.59}$$

where x_{GCP}^{ECEF}, y_{GCP}^{ECEF} and z_{GCP}^{ECEF} are the ECEF coordinates of the GCP (provided by the map) and $x_{Pelican}^{ECEF}$, $y_{Pelican}^{ECEF}$, $z_{Pelican}^{ECEF}$ are the Pelican ECEF coordinates given by the on-board GPS receiver.In the second approach, this vector is computed by DGPS processing (Figure 3.21).

This vector in ECEF ($\Delta\underline{r}^{ECEF}$) is then converted in NED ($\Delta\underline{r}^{NED}$) following Equation 3.7 from which it is straightforward to calculate the reference Azimuth (Az_{Ref}) and Elevation (El_{Ref}) in NED which are used as attitude independent measurements.

For what concerns the attitude dependent measurements, this is obtained starting from the Pelican-to-GCP LOS in BRF ($\hat{r}^{BRF}$) which is obtained by detecting on each image the GCP (Figure 3.19, Figure 3.20) and applying Equation 3.4.

$\hat{r}^{BRF}$ is then transformed in two unit vectors, one, $\hat{r}^{NED,DGPS/Vision}$ applying the rotation matrix $\underline{\underline{R}}_b^{n,DGPS/Vision}$ computed by exploiting DGPS/Vision information, and the other one, $\hat{r}^{NED,Pelican}$ applying the $\underline{\underline{R}}_b^{n,Pelican}$ computed by the Pelican navigation filter as follows

$$\begin{aligned} \hat{r}^{NED,DGPS/Vision} &= \underline{\underline{R}}_b^{n,DGPS/Vision} \hat{r}^{BRF} \\ \hat{r}^{NED,Pelican} &= \underline{\underline{R}}_b^{n,Pelican} \hat{r}^{BRF} \end{aligned} \tag{3.60}$$

Also in this case, from these two attitude dependent unit vectors it is straightforward to obtain azimuth ($Az_{DGPS/Vision}$, $Az_{Pelican}$) and elevation ($El_{DGPS/Vision}$, $El_{Pelican}$) angles.

Consequently, azimuth and elevation errors are given by

$$\begin{aligned} \Delta Az_{DGPS/Vision} &= Az_{DGPS/Vision} - Az_{Ref} \\ \Delta Az_{Pelican} &= Az_{Pelican} - Az_{Ref} \end{aligned} \tag{3.61}$$

$$\begin{aligned} \Delta El_{DGPS/Vision} &= El_{DGPS/Vision} - El_{Ref} \\ \Delta El_{Pelican} &= El_{Pelican} - El_{Ref} \end{aligned} \tag{3.62}$$

Two important factors for effective application of the proposed accuracy evaluation strategy regard the uncertainty of the reference measurements (Az_{Ref}, El_{Ref}), and the relation between the attitude measurement uncertainties and the computed azimuth and elevation angles ($Az_{DGPS/Vision}$; $Az_{Pelican}$, $El_{DGPS/Vision}$; $El_{Pelican}$).

As regards the first point, the accuracy of the reference measurements depends on the adopted strategy. In fact

1. The georeferenced map has a planar sub-metric accuracy, while the error on Pelican positioning depends on horizontal accuracy of standalone GPS. Due to the large distance from the GCP (about 600 m), the linear uncertainty of the baseline is converted into a relatively small angular error. For the sake of concreteness, if one assumes 6 meters of horizontal relative positioning error, the worst case uncertainty on the reference azimuth measurement (i.e., error vector normal to the Pelican-GCP line of sight) is given by

$$\sigma_{Az_{Ref}} = \tan^{-1}\left(\frac{6}{600}\right) \approx 0.01 rad = 0.57^\circ \tag{3.63}$$

As mentioned above, the focus of these tests is mainly on heading performance, as a consequence only the processing strategy and results concerning azimuth in NED are relevant.

2. The baseline estimation error, due to DGPS, is of the order of 1 and 2 meters (code-based DGPS), or 0.05 and 0.2 meter (CDGPS) in horizontal and vertical directions respectively. Due to the large distance from the GCP (about 100 meters), the linear uncertainty of the baseline is converted into a small angular error. For the sake of concreteness, uncertainties on the reference azimuth and elevation measurements (at 100 meters) are given by

$$\begin{aligned} \sigma_{Az_{Ref}} &= \tan^{-1}\left(\frac{1}{100}\right) \approx 0.01 rad = 0.57^\circ \\ \sigma_{El_{Ref}} &= \tan^{-1}\left(\frac{2}{100}\right) \approx 0.02 rad = 1.14^\circ \end{aligned} \tag{3.64}$$

If a code-based solution is applied, or

$$\begin{aligned} \sigma_{Az_{Ref}} &= \tan^{-1}\left(\frac{0.05}{100}\right) \approx 0.03^\circ \\ \sigma_{El_{Ref}} &= \tan^{-1}\left(\frac{0.2}{100}\right) \approx 0.11^\circ \end{aligned} \tag{3.65}$$

with a CDGPS solution.

As concerns the relation between azimuth and heading, it is intuitive that for quasi-horizontal baseline and for small roll and pitch angles (as it indeed happens in the considered flight tests), azimuth accuracy depends primarily on heading measurement performance, with very little effect produced by the other errors. The same applies to the elevation which mainly depends on pitch measurement performance if the angle between the roll axis and the direction to the GCP is small. This can be demonstrated analytically by deriving a first order error budget.

In particular, starting from the equations of the computed azimuth and elevation as a function of unit vectors in NED it is possible, both for DGPS/Vision

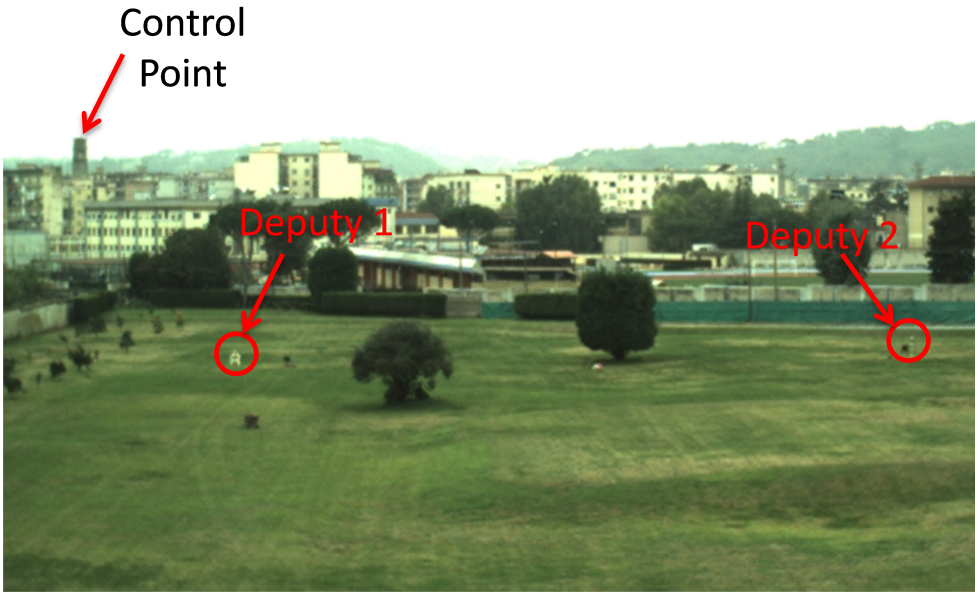

Figure 3.19: Example of image acquired from the chief vehicle showing the observation geometry during Test 1 and 2.

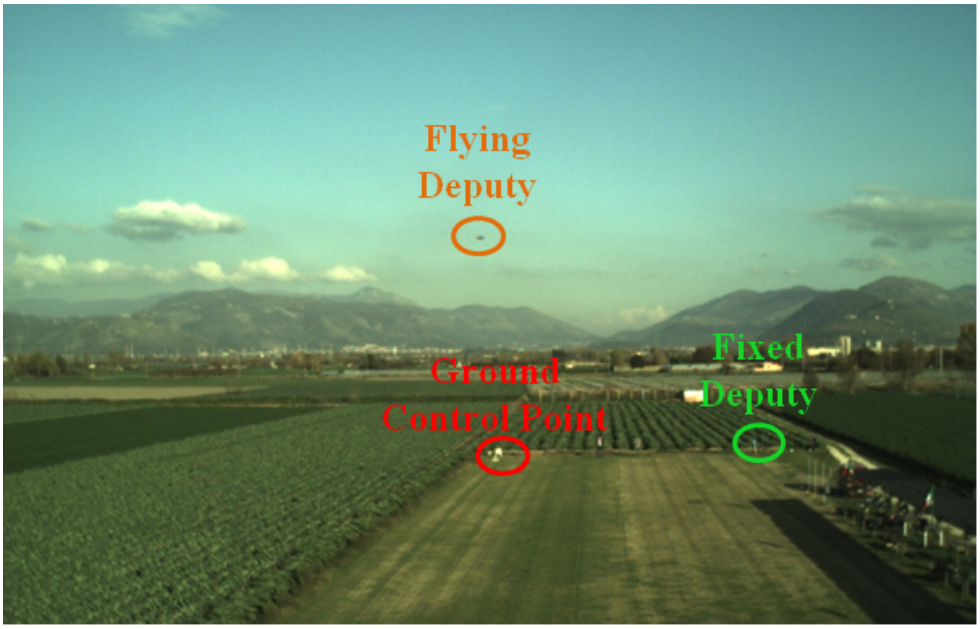

Figure 3.20: Example of image acquired from the chief vehicle showing the observation geometry during Test 3.

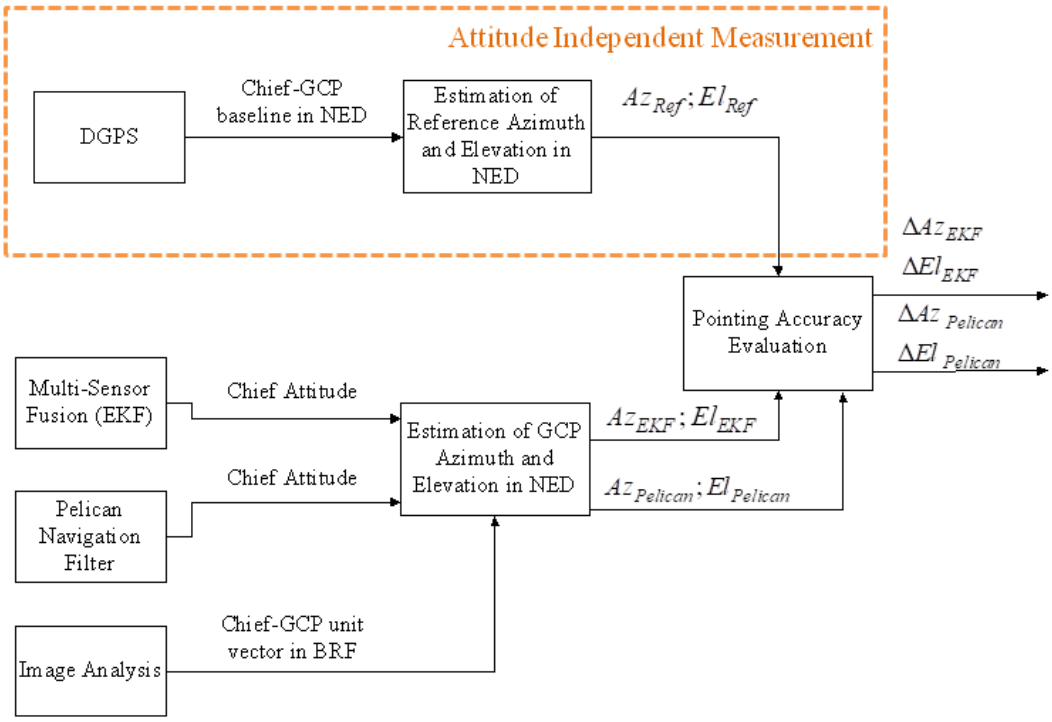

Figure 3.21: Pointing accuracy logical scheme.

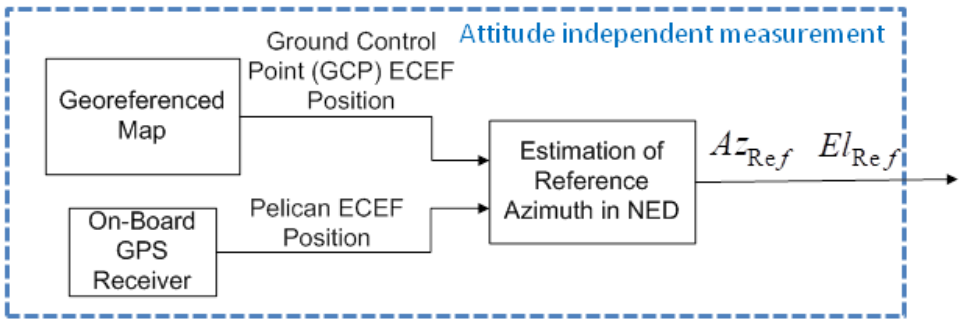

Figure 3.22: Attitude independent measurement from georeferenced GCP.

and Pelican navigation filter, to express the azimuth and elevation uncertainties as

$$\sigma_{Az}^2 \cong \left(\frac{\partial Az}{\partial \psi}\right)^2 \sigma_\psi^2 + \left(\frac{\partial Az}{\partial \theta}\right)^2 \sigma_\theta^2 + \left(\frac{\partial Az}{\partial \phi}\right)^2 \sigma_\phi^2 + \cdots \left(\frac{\partial Az}{\partial Az_{CRF}}\right)^2 \sigma_{Az_{CRF}}^2 + \left(\frac{\partial Az}{\partial El_{CRF}}\right)^2 \sigma_{El_{CRF}}^2 \tag{3.66}$$

$$\sigma_{El}^2 \cong \left(\frac{\partial El}{\partial \psi}\right)^2 \sigma_\psi^2 + \left(\frac{\partial El}{\partial \theta}\right)^2 \sigma_\theta^2 + \left(\frac{\partial El}{\partial \phi}\right)^2 \sigma_\phi^2 + \cdots \left(\frac{\partial El}{\partial Az_{CRF}}\right)^2 \sigma_{Az_{CRF}}^2 + \left(\frac{\partial El}{\partial El_{CRF}}\right)^2 \sigma_{El_{CRF}}^2 \tag{3.67}$$

where ψ, θ and ϕ are heading, pitch, and roll, respectively, while Az_{CRF} and El_{CRF} are the GCP azimuth and elevation angles computed in the camera reference frame.

The squared derivatives can be computed analytically. and they measure the sensitivity of azimuth and elevation uncertainties on the input errors, and depend themselves on ψ, θ, ϕ, Az_{CRF} and El_{CRF}.

For the sake of concreteness, in view of the analyzed experiments, assuming CRF coincident with BRF, null chief attitude angles, $Az_{CRF} = -20°$, and $El_{CRF} = -5°$, values of the computed derivatives are sown in Table 3.2.

This table shows that the main contributions to azimuth pointing error are the uncertainties on ψ and Az_{CRF}.

Even degree-level errors on roll and pitch have a limited contribution, since they are strongly attenuated. On the other hand, since uncertainties in Az_{CRF} and El_{CRF} are related to the camera IFOV and thus of the order of 0.05° in the considered case, the final uncertainty on azimuth pointing is given by a small amplification of the heading one.

Similarly, Table 3.2, shows that the main contributions to elevation pointing error are the uncertainties on θ and El_{CRF}, though a larger coupling with roll angle is present.

Table 3.2: Pointing error derivatives.

	Azimuth Error	Elevation Error
$\left(\frac{\partial}{\partial\psi}\right)^2$	1	0
$\left(\frac{\partial}{\partial\theta}\right)^2$	$9 \cdot 10^{-4}$	0.9
$\left(\frac{\partial}{\partial\phi}\right)^2$	$7 \cdot 10^{-3}$	0.1
$\left(\frac{\partial}{\partial Az_{CRF}}\right)^2$	1	0.5
$\left(\frac{\partial}{\partial El_{CRF}}\right)^2$	0	1.4

In conclusion, this analysis shows that, for the considered experimental conditions, azimuth and elevation accuracy evaluation represents a good benchmark to evaluate and compare heading and pitch estimation performance respectively.

3.6 Experimental Results

During the experimental tests, images acquired by the (forward-looking) camera and GPS data have been gathered on-board the chief at 1Hz frequency and IMU data at about 100Hz, in addition, GPS measurements from the ground antennas have been acquired at 5Hz, while, when involved in the testing strategy, GPS data have been stored on-board the flying deputy at 1Hz.

Performance analysis is thus based on off-line processing, and GPS time is used for accurate data synchronization, avoiding the need of a communication link among flying and ground systems.

Indeed, when considering real time implementation of the developed data fusion algorithm, communication delays can occur. However, due to the short range LOS communication architecture, and the small amount of data to be shared (only GPS observables from the deputies), it is expected that these delays will be short, and real time communication can be effectively achieved by

technologies available onboard small and even micro-UAVs. In addition, taking into account the typical dynamics of small and Micro-UAVs, this problem can be overcome by adopting a negative-time measurement update approach in which, when the delayed measurement arrives (with an accurate time stamp), state and covariance updates are calculated at the measurement time and propagated to the current time [67, 68]. This requires accurate data time tagging, and to keep in memory a sliding window where navigation data are stored. The considered time window dimensions correspond to the largest possible latencies. This processing can be considered compatible with the computational resources currently available onboard small UAVs.

In the following, experimental data are analyzed to highlight the performance of the novel DGPS/Vision algorithm and the consequent advantage of relying on magnetic- and inertial-independent accurate attitude information.

3.6.1 Differential GPS

To assess the performance of the differential-GPS strategies described in subsection 3.3.2, baselines are estimated in static and dynamic conditions.

Considering the CDGPS solution, carrier phase residuals are used as index for evaluating the performance of the filter described in subsubsection 3.3.2.2.

The static configuration is assessed using data coming out from the two ground antennas. Results are depicted in Figure 3.23 which shows (with different colors) the CP residuals for each available couple of GPS satellites, where both strategies (EKF and EKF+LAMBDA) showed in subsubsection 3.3.2.2 are used.

When static receivers are used, the strategy that fixes the ambiguities (LAMBDA) shows an advantage in baseline estimation. The ambiguities that are correctly estimated show a sudden drop of the corresponding CP residuals (see red and purple lines in Figure 3.23). It is important to note that not all the ambiguities are fixed: this is the case of yellow and green lines that do

not show any jump. This means that the relevant ambiguities are not fixed in the processed time span. Indeed, the ambiguity thresholds have been carefully selected to avoid false ambiguities fixing, while guaranteeing that a reasonably large set of ambiguities is fixed and thus improving the performance in baseline estimation with respect to the simple EKF filter.

CP residuals of baseline estimation for two flying receivers are shown in Figure 3.24, in this case data from Pelican and X8+ GPS receivers are used to compare the filters performance. Comparing the two plots in Figure 3.24, it is possible to highlight that no improvement is provided by combining the EKF with LAMBDA. During the experiment, the receivers experienced a significant amount of cycle slips (both on Pelican and on X8+). Recurring slips (one each 4 seconds on average) cancel out the advantage of the combined EKF + LAMBDA filter because (1) the high slip rate makes the correct ambiguities estimation and fixing harder and (2) even if ambiguities are fixed they are rapidly discarded because of the occurrence of a new slip.

As a consequence, the EKF-only algorithm depicted in Figure 3.3 has been preferred due to the lower computational burden.

The baseline norm of the receiver couples estimated with CDGPS technique is shown in Figure 3.25 and it is compared with the DGPS processing presented in subsubsection 3.3.2.1. As expected, even if CDGPS and DGPS solutions are in general in good agreement, CDGPS is much smoother than DGPS one. The results suggest, as shown in Figure 3.25 and Figure 3.26 that using the CDGPS, the accuracy in estimating the baseline is an order of magnitude better than the DGPS one.

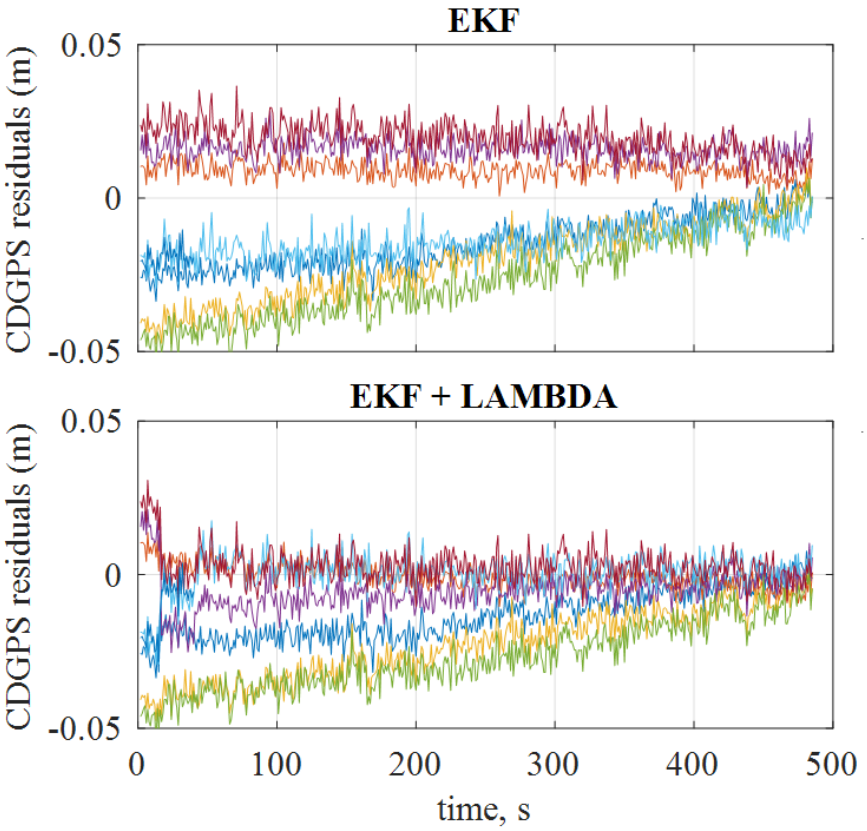

Figure 3.23: CP residuals of EKF and EKF+LAMBDA filters (static receivers).

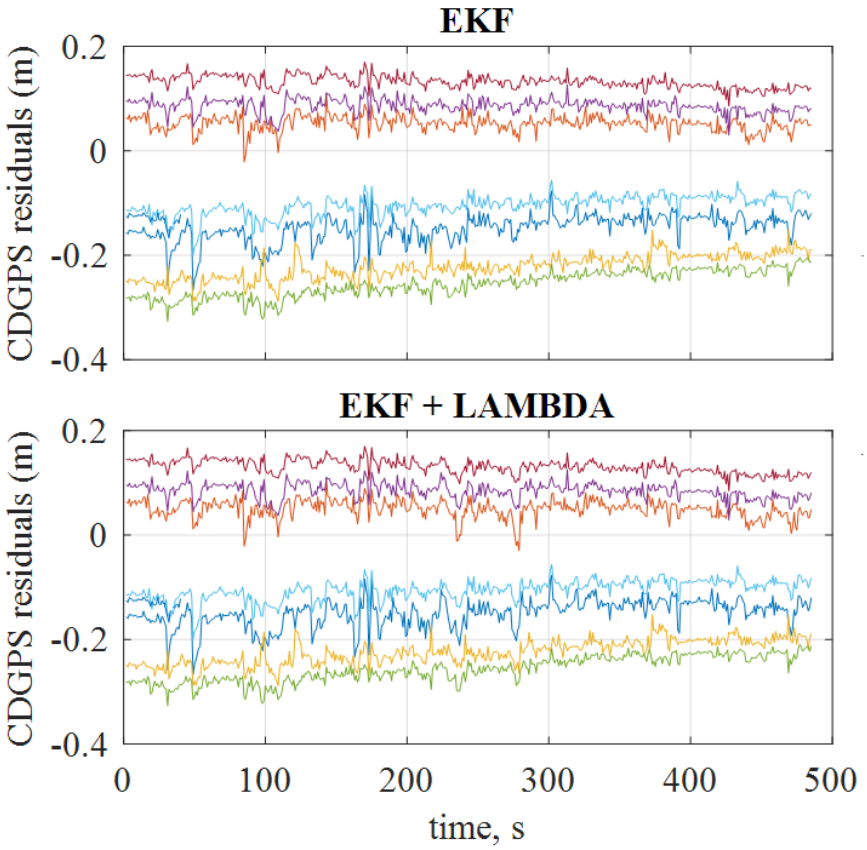

Figure 3.24: CP residuals of EKF and EKF+LAMBDA filters (dynamic receivers).

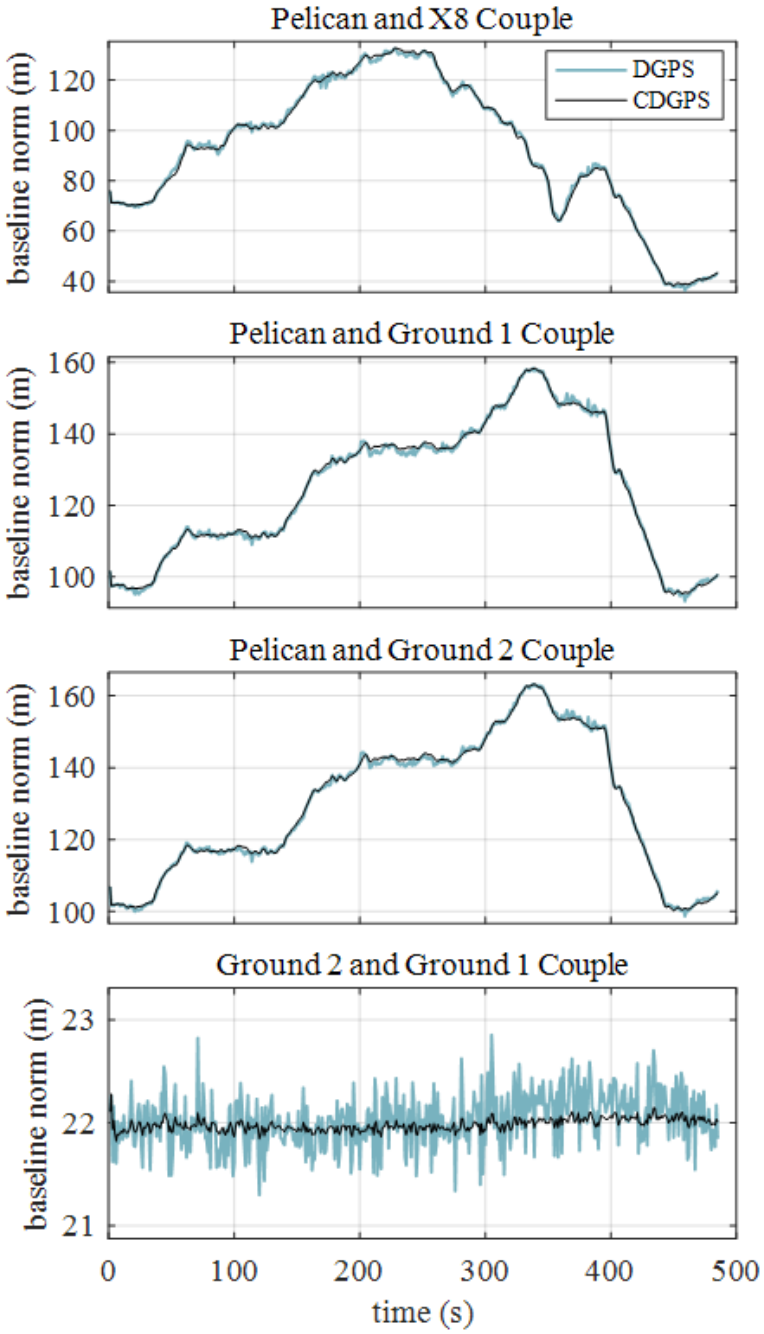

Figure 3.25: Estimated CDGPS and DGPS Baseline Norm.

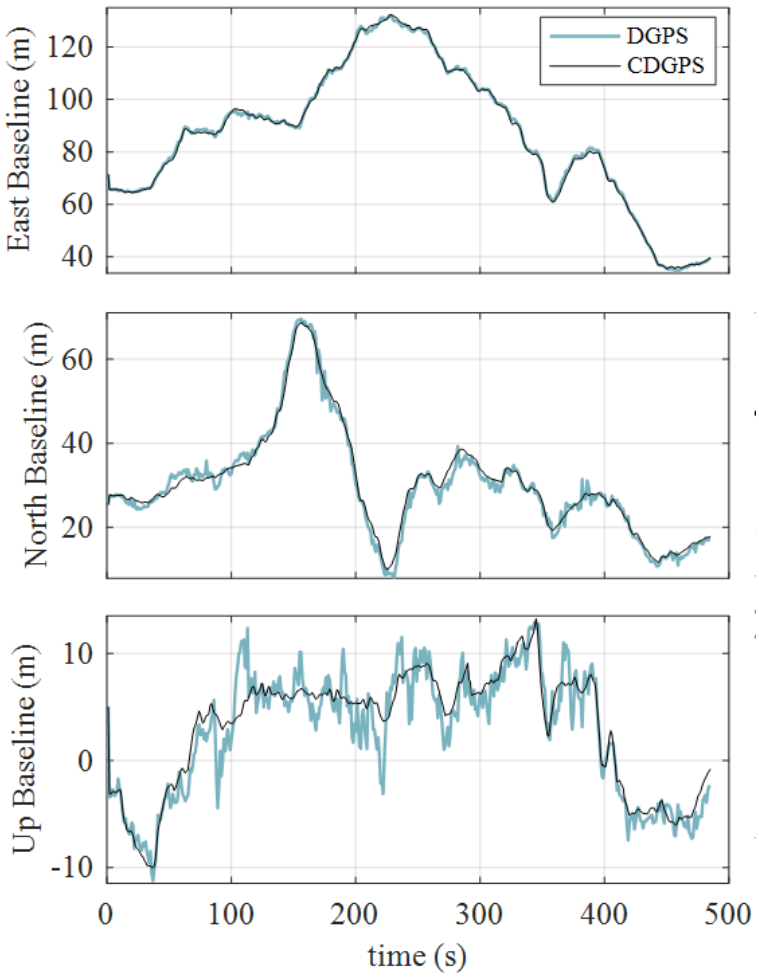

Figure 3.26: Pelican-X8 couple baseline components in ENU.

3.6.2 Loosely coupled approach

The EKF loosely coupled approach has been tested with experimental data acquired during Test 1 and 2.

As already mentioned, in order to estimate the attitude through the TRIAD algorithm, two deputies are required. In Test 1 and 2, the role of deputies has been played by the two ground antennas and only the code-based DGPS solution has been adopted. In Test 1, the position of the GCP for pointing accuracy analysis (subsection 3.5.3) has been obtained on an open source 1:1000 georeferenced map.

It is worth noting that these tests have been mainly designed to compare heading estimates coming out from the DGPS/Vision method, the Pelican navigation filter and magnetometers. This is of great importance considering challenges in estimating heading angle by using low cost MEMS inertial and magnetic sensors, in particular due to possible magnetic disturbances.

3.6.2.1 Test 1

This dynamic test has been performed to evaluate the effects of relatively aggressive heading maneuvers on both the EKF and the Pelican navigation filter.

Baselines longer than 100 meters have been kept during most of the flight (Figure 3.14), in particular, as shown in Figure 3.27, after a very smooth flight of almost 230 seconds, three 360° heading rotations have been commanded. It is worth noting that, during the 360° heading rotations, the DGPS/Vision attitude measurements are not continuously available due to the impossibility to maintain the deputies within the camera FOV. However, the developed filtering architecture can compensate for temporary measurement losses using inertial measurements to propagate attitude estimates.

From a practical point of view, short DGPS/Vision outages, such as the ones experimented during the presented test, do not impact in a significant way the

heading estimation performance.

In the following, to get a clearer insight into the DGPS/Vision performance and robustness, it is worthwhile to focus the attention on three flight segments (ellipses), as indicated in Figure 3.27. In fact, while the proposed EKF, aided by DGPS/Vision measurements which are independent from magnetic and inertial information, does not show dependence from flight dynamics and history, the Pelican navigation filter shows significant limits particularly at the end of the heading rotation maneuvers.

In Figure 3.28 the low frequency rotations of the heading angle during the first time interval does not introduce any significant disturbance and consequently the Pelican navigation filter algorithm follows quite well the heading given by the MEMS magnetometer. The first flight segment lies before the heading rotation maneuvers (Figure 3.27). Within this time interval, the difference of about 5.3° (Table 3.3) between heading estimates obtained via DGPS/Vision and Pelican navigation filter is almost constant. This difference is mainly due to magnetic biases. In addition, Figure 3.29 shows a good consistency between magnetometer-based and Pelican navigation filter estimates (Table 3.3).

Focusing on the flight segment immediately after the three heading rotations, it is interesting to evaluate the response of the Pelican navigation filter and the customized EKF to abrupt maneuvers. In fact, as shown in Figure 3.29, after the three rotations, the EKF heading estimate has a behavior similar to the one experimented during the smooth flight phase, keeping an offset of about 7.1° (see Table 3.3) with respect to the magnetometer based heading. Being strongly impacted by DGPS/Vision measurements, EKF has a very limited dependence on the experimented dynamics. On the other hand, the Pelican navigation filter shows a significant drift mainly due to the low weight given to magnetometer-based measurements and to the coarse gyroscopes accuracy, leading to large error accumulation. The difference between the Pelican navigation filter and the EKF

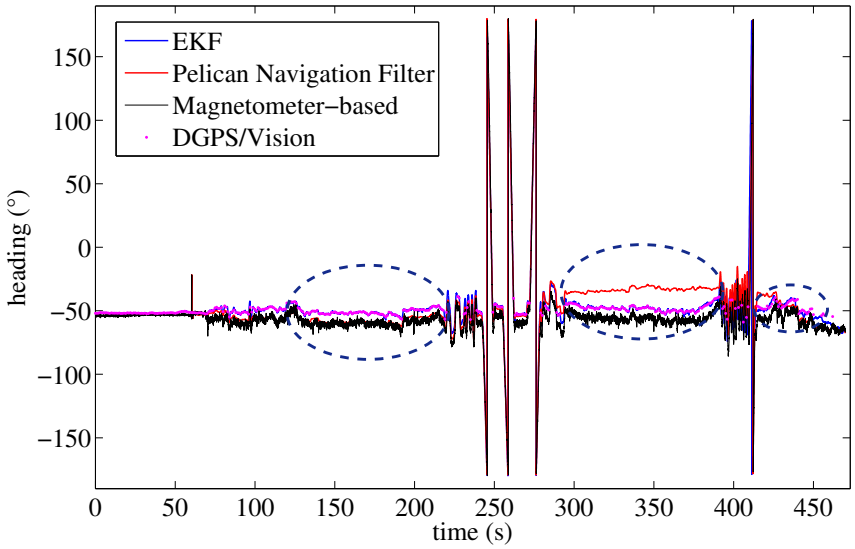

Figure 3.27: Heading as a function of time (Test 1).

heading estimates reaches a maximum value of about 20° (Figure 3.29), while an offset of 23° is also generated between the heading estimated by the Pelican navigation filter and the one estimated using the magnetometer (Table 3.3). Only at the end of the flight, the Pelican navigation filter slowly reduces its offset with respect to the EKF and magnetometer based heading.

As shown in Table 3.3, only after several tens of seconds, and further maneuvers (third time interval, Figure 3.30), the Pelican navigation filter solution recovers the offset with respect to DGPS/Vision and magnetometer-based heading, thus achieving a final performance level that resembles the one experimented in the first flight segment. During all the flight test, the difference, of about 7° (Table 3.3), between DGPS/Vision and magnetometer-based heading does not show significant variations. In summary, compared with classical attitude determination techniques, this test confirms the potential of DGPS/Vision to provide small noise measurements which are completely independent from attitude dynamics history.

Time intervals 1 and 2 have been chosen in order to show the accuracy achiev-

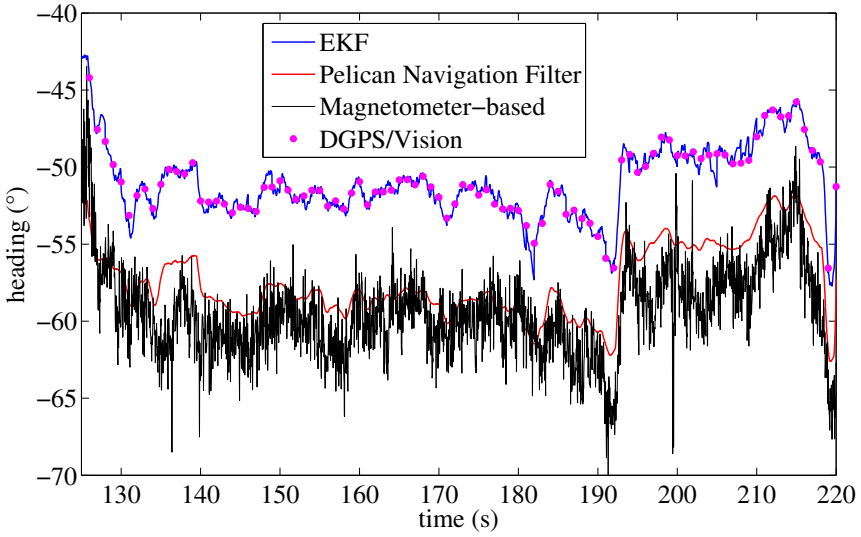

Figure 3.28: Heading angle as a function of time (Test 1 - first time interval.)

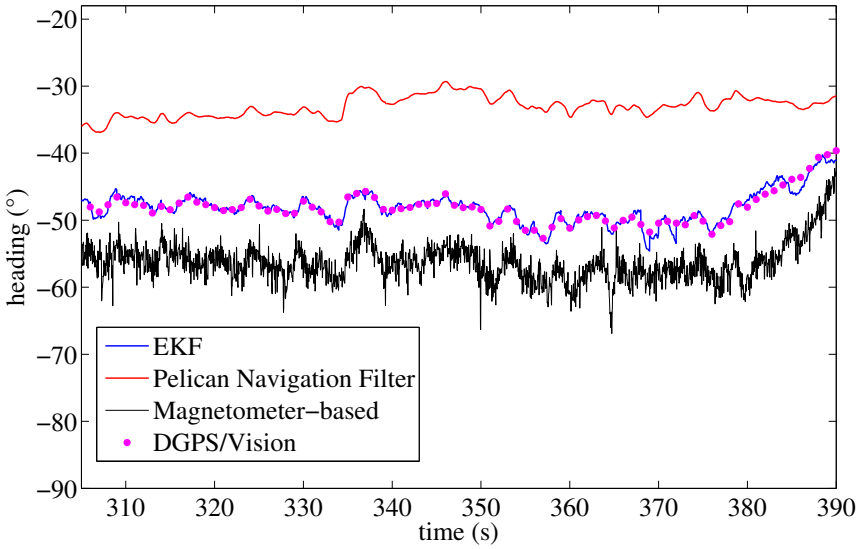

Figure 3.29: Heading angle as a function of time (Test 1 - second time interval).

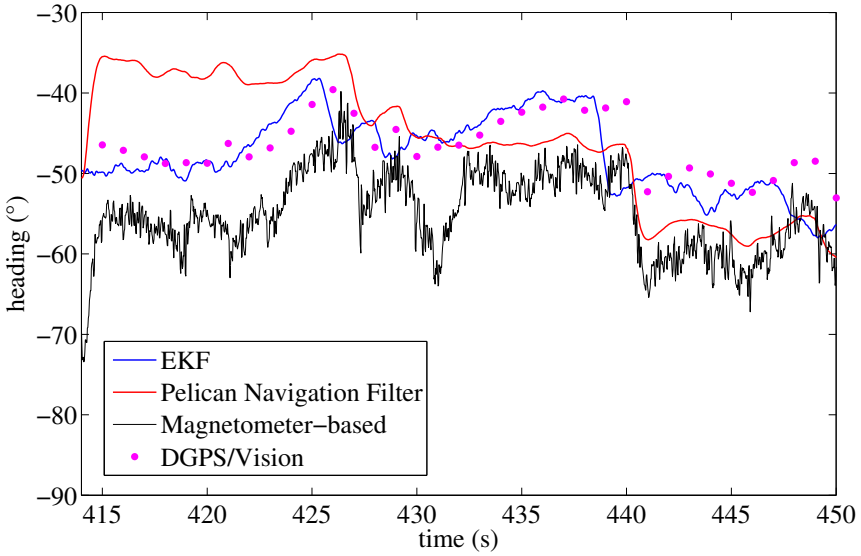

Figure 3.30: Heading angle as a function of time (Test 1 - third time interval).

Table 3.3: Test 1 heading comparison (mean values in degrees).

Time Intervals	EKF	Magnetometer	Pelican Navigation Filter	Diff. between EKF and Magnetometer	Diff. between EKF and Pelican
1	-52.9	-60.2	-58.2	7.3	5.3
2	-49.2	-56.3	-33.1	7.1	-16.1
3	-47.5	-54.7	-45.9	7.2	-1.6

able by integrating attitude estimates, derived by DGPS/Vision measurements, within the customized EKF.

The adopted accuracy evaluation strategy has been described in subsection 3.5.3, in particular, here the attitude independent measurement is obtained detecting a GCP on a 1:1000 georeferenced map.

Figure 3.31 and Figure 3.32 show the computed errors in these two time intervals for the attitude estimated by DGPS/Vision (TRIAD), EKF and Pelican navigation filter.

Considering the first time interval (Figure 3.31), the EKF and the DGPS/Vision show similar performance, with sub-degree azimuth errors and a standard deviation over the mean azimuth error of about 0.3°. On the contrary, the Pelican navigation filter shows a mean azimuth error of about 4.4°.

Considering the second time interval (Figure 3.32) after the three 360° heading rotations, the EKF and DGPS/Vision mean error remains sub-degree while the Pelican navigation filter one increases to about 17.6°. These results show that, unlike the Pelican navigation filter, the EKF errors do not show a clear dependence on flight dynamics history, and fall within the uncertainty of the reference azimuth measurements.

3.6.2.2 Test 2

This test has been conducted mainly to analyze the effect of the DGPS/Vision heading estimate within the EKF, in a scenario with changing aircraft orientation within the Earth magnetic field (Figure 3.15).

During this test, a number of attitude maneuvers (e.g., yaw rate oscillations) have also been commanded (Figure 3.33). As before, EKF and DGPS/Vision results are compared to Pelican navigation filter output and to magnetometer-based estimates.

As shown in section 3.4, a horizontal baseline of about 100 meters is needed

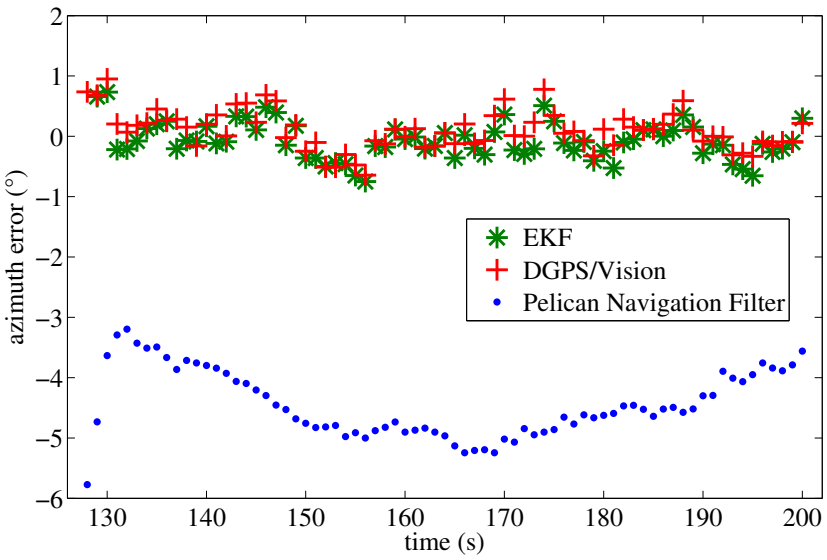

Figure 3.31: Azimuth error as a function of time (Test 1 - first time interval).

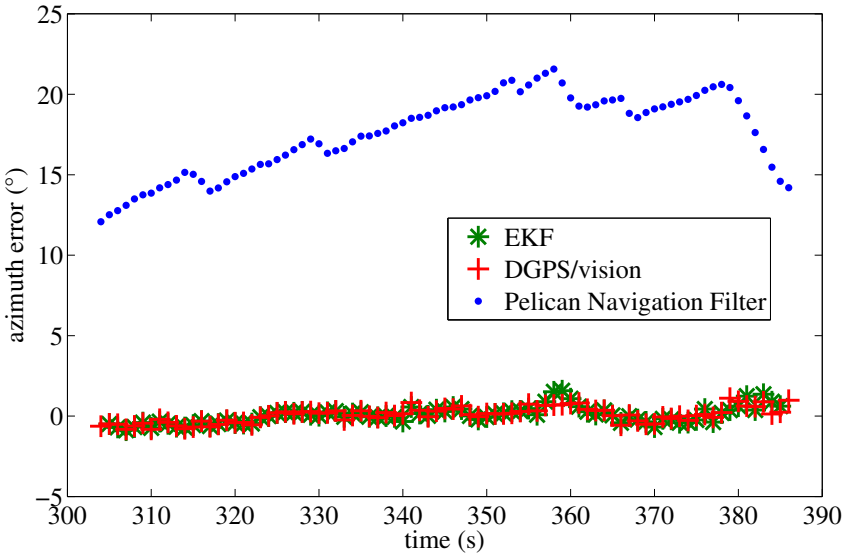

Figure 3.32: Azimuth error as a function of time (Test 1 - second time interval).

to have a DGPS/Vision heading accuracy of the order of 0.4°. This baseline has been achieved in the initial and final phase of the dynamic test (Figure 3.16): these two flight segments, highlighted with ellipses in Figure 3.33, are thus focused in this analysis. The heading variation between the considered time intervals is of about 140°, as a result, the GCP used for pointing accuracy analysis was out of FOV for most of the time, hence, for this test pointing accuracy analysis is not performed.

Heading behavior is analyzed in Figure 3.34 (first time interval) and Figure 3.35 (second time interval), which depict EKF and DGPS/Vision estimates together with onboard navigation filter and magnetic heading.

In both flight segments, the EKF is initialized with Pelican navigation filter output, and after a fast transient phase a difference of several degrees is generated between EKF and onboard navigation filter. The heading difference also changes in time, which basically derives from the combined effect of gyroscopes bias instability and magnetic uncertainties.

As regards the comparison of the two flight segments, first of all the absolute difference between magnetic heading and onboard navigation filter shows a large change (2.4° during the first flight segment and 15.5° during the second flight segment), basically due to the flight history and the experimented dynamics. More importantly, the mean difference between EKF and onboard navigation filter also shows a significant change, in fact the absolute difference is about 4.9° during the first flight segment and 8.4° in the second flight segment. While residual misalignment between camera and IMU would generate a constant difference, this variation is basically due to the effect of magnetometers biases and residual uncompensated on board magnetic fields, which changes as a function of the aircraft heading during flight.

This is also evident if EKF output is compared with magnetic heading. In fact, in both Figure 3.34 and Figure 3.35, if we filter out the high frequency

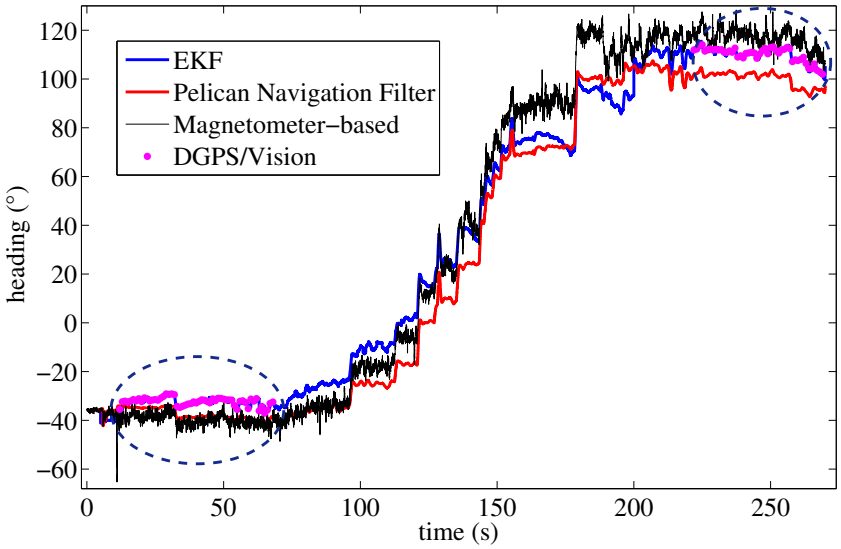

Figure 3.33: Heading as a function of time (Test 2).

Table 3.4: Heading comparison (mean values in degrees) Test 2.

Time Intervals	EKF	Magnetometer	Pelican Navigation Filter	Diff. between EKF and Magnetometer	Diff. between EKF and Pelican
1	-32.4	-39.7	-37.3	7.3	4.9
2	109.5	116.6	101.1	-7.1	8.4

noise that characterizes magnetometer output, magnetic heading has an offset, with respect to the EKF, which changes sign and value. In fact, in the first flight segment the difference between the EKF and the magnetic heading is 7.3° while in the second flight segment the difference is −7.1°.

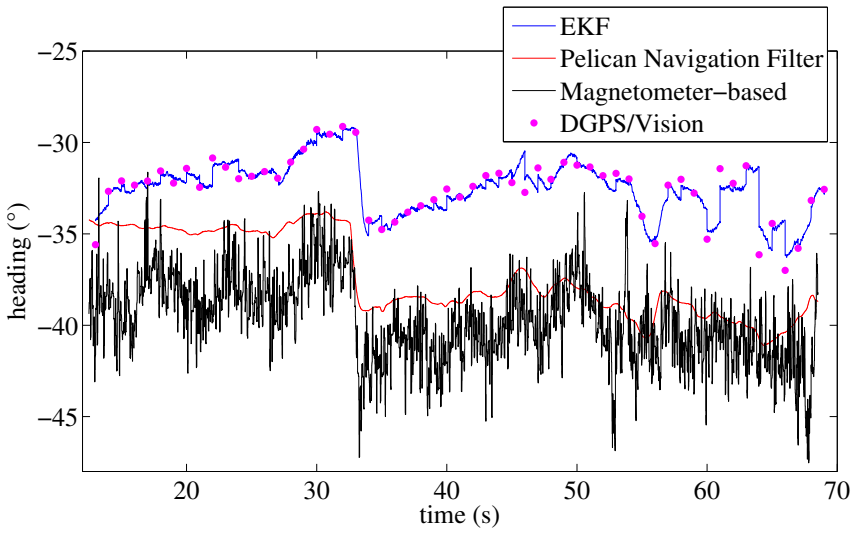

Figure 3.34: Heading as a function of time (Test 2 - first time interval).

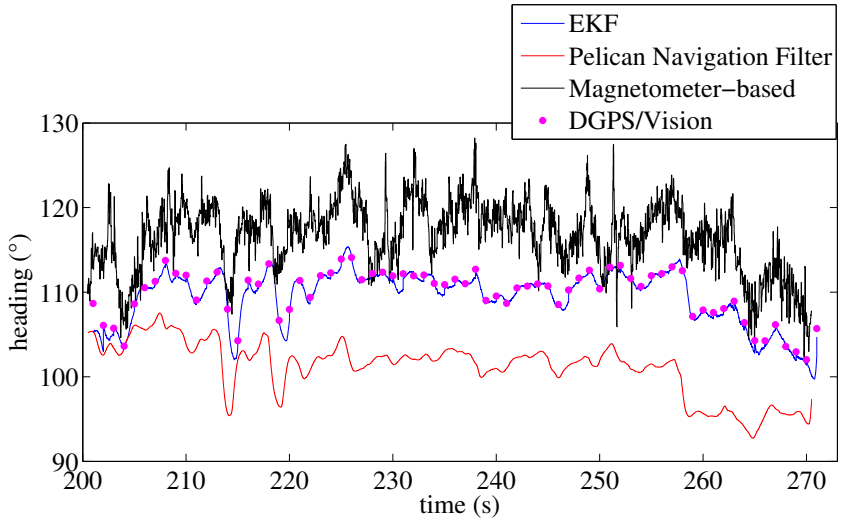

Figure 3.35: Heading as a function of time (Test 2 - second time interval).

3.6.3 Tightly coupled approach

Tight integration of DGPS/Vision measurements within the EKF has been tested on experimental data acquired during Test 3.

The basic testing strategy has consisted in changing baseline length and formation geometry, while always keeping the flying deputy within the FOV of the chief onboard camera. A further driver for certain flight geometries has been the need to keep also ground antennas within the FOV for most of the flight. GPS flight paths and position of ground antennas are shown in Figure 3.17.

Given also the focus on heading performance estimation, heading maneuvers have been essentially commanded to the chief, with different rates. In fact, some fast 360° rotations have been commanded to verify the capability of the proposed approach to track fast dynamics and to analyze possible drift accumulation phenomena, while most of the flight has been characterized by slow angular velocities, which are difficult to track due to the high gyroscope noise. Furthermore, heading rotations have been also commanded to estimate magnetic effects, though the need of keeping ground antennas within the FOV has limited the range of variation for chief heading. In Figure 3.18 the baselines between the chief and the ground antennas (larger than 100 meters) and the one with the flying vehicle (varying between 70 and 130 meters) are shown.

During the test DGPS/vision measurements are available for most of the considered time, only some isolated losses are produced by the impossibility to detect antennas within images. In fact, as regards the flying deputy, temporary losses are primarily due to sudden changes of illumination and/or camera shutter times, whose effects are amplified by the low flight altitude and the strong contrast between sky and ground image regions. Instead, line of sight losses for the ground antennas are essentially due to the limited camera FOV and the maneuvers executed during the test.

The tightly coupled EKF (subsubsection 3.3.4.4) has been run integrating 1

LOS, derived by adopting a code-based DGPS solution, or 2 LOS in which both code-based DGPS and CDGPS solutions have been considered. EKF results are compared to Pelican navigation filter output and the pointing accuracy analysis is conducted. During this test, the flying deputy vehicle (X8) and the fixed deputy (ground antenna) are exploited to obtain attitude information, whereas the second ground antenna is used as GCP in order to have a benchmark to evaluate the accuracy of the proposed approach.

Starting from the code-based DGPS, the EKF integrating 1 LOS or 2 LOS is run through the whole flight, and it is initialized with the first measurement coming from the Pelican navigation filter. In order to increase readability, Figure 3.36 shows the heading angle during the whole flight in which the 360 degrees heading rotations have been cut and also magnetometer based estimates are included. In Figure 3.36 it is possible to appreciate how the Pelican navigation filter presents a significant drift while the offset between EKF heading estimates and the magnetometer based one remains almost constant.

In order to clarify some aspects of the proposed method, that is the independence of DGPS/Vision measurements from magnetic and inertial information, it is worthwhile to focus the attention on four flight segments as indicated in Figure 3.36 (ellipses).

The first considered flight segment (Figure 3.37 (a) up) is before the 360 degrees heading rotation maneuvers. During this time interval, the onboard navigation filter presents a drift with respect to the proposed EKF reaching a maximum offset of about 20 degrees. This behavior is mainly due to the commanded slow heading rotation maneuvers and, hence, the low angular velocities that fall within the gyroscopes noise, making it difficult for the onboard navigation filter to follow the real heading dynamics. On the other hand, the proposed EKF, aided by DGPS/Vision measurements, does not present drift and shows a trend similar to the magnetometer-based heading (though magnetometer so-

lution is noisier) with an almost constant bias of about 7 degrees. The pointing accuracy analysis (Figure 3.37 (a) bottom) clearly demonstrates the different accuracy of the two heading estimates. 1LOS and 2LOS EKF do not show significant differences in this phase, due to the geometry which provides a good heading information also with a single LOS. In fact, local differences among the two EKF are mostly due to temporary losses of the flying deputy.

The second flight segment following the 360 degrees heading rotation maneuvers (Figure 3.36) covers the time interval between 100 and 175 seconds. The general behavior is similar to Figure 3.37 (a), but an increased offset is generated between the EKF and the onboard navigation filter (up to about 60 degrees) due to the effects of experimented dynamics, i.e., the drift accumulated during fast rotations. As before, EKF and magnetometer-based estimates (which are both insensitive to the flight history) present an absolute difference of about 7 degrees.

In Figure 3.37 (b) up the different behavior of the two considered EKF, in the interval between 107 and 113 seconds, has been put in evidence. This difference is due to the fact that, immediately after rotations, due to the illumination conditions measurements from the fixed deputy are available a little in advance with respect to the flying deputy. This means that in this time interval the green line is equivalent to the case of a single line-of-sight. Again, pointing analysis (In Figure 3.37 (b) bottom) demonstrates that sub-degree accuracy can be attained as soon as cooperative aiding measurements are available.

In Figure 3.37 (c) (third flight segment) faster heading rotations help the pelican navigation filter to follow the real dynamics. As a consequence, at the end of the considered interval, the pelican navigation filter recovers some of the offset with respect to the EKF estimates reaching a final value of about 15 degrees. In addition, if one compares EKF and magnetometer-based solutions in the time interval that goes from about 210 seconds up to 245 seconds, where the

maximum heading angle is reached, the offset is of about 10 degrees. This result confirms that the origin of this difference lies in the effect of uncompensated magnetometer biases and onboard magnetic fields, which are constant in the body reference frame and thus generate an effect on heading estimation error which strongly depends on quadrotor orientation within the Earth's magnetic field.

The fourth flight segment (Figure 3.37 (d)) is characterized by a low frequency profile of the heading angle. The absolute difference between EKF and magnetometers is again of about 7 degrees due to the Pelican heading being of the order of the one experimented in the first part of the test. Regarding the pelican navigation filter, due to the experienced dynamics, the offset remains almost constant till the end of the considered time interval.

Both in the third and in the forth flight segment, pointing analysis results do not show significant differences with respect to the considerations formulated on the first part of the experiment.

Although formation geometries and experimental tests have been mainly designed to optimize and analyze heading angle estimation performance, for the sake of completeness in Figure 3.38 and Figure 3.39 pitch and roll angles as estimated by the EKF and the on-board navigation filter are shown. Both pitch and roll diagrams show a good similarity between different measurements.

In particular, the roll estimate from the 1 LOS EKF is very similar to the Pelican navigation filter, as a result of the fact that the LOS to the flying deputy is always close to the forward aircraft direction, and the baseline is not large enough to guarantee some accuracy improvement. A difference can be detected for the 2 LOS EKF, where the (limited) angular separation between deputies can be exploited, though the information content is relatively limited.

As regards pitch, LOS measurements have some more impact on the EKF solution, generating degree-level differences with respect to the Pelican navigation

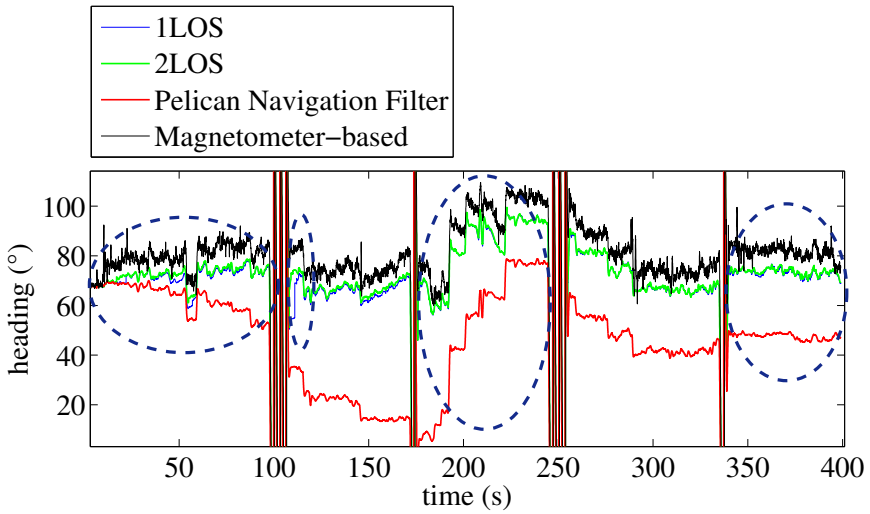

Figure 3.36: Heading as a function of time (Test 3).

filter.

Table 3.5 summarizes pointing accuracy results relevant to the whole flight. In general, for the considered formation geometries, including DGPS/Vision measurements permits reducing both azimuth and elevation root mean square errors.

Error statistics are consistent with basic system budgets (Figure 3.37), also considering that they actually comprise flight phases with temporary losses of cooperative measurements. Since the baselines and the flight geometries change during the flight, both benchmark accuracy and sensitivity coefficients tend to change. On average during the whole flight, sub-degree accuracy in reference azimuth, and degree-level accuracy in reference elevation, can be assumed.

Thus, differences in azimuth error can be considered as statistically significant, showing that the 2 LOS filter outperforms the 1 LOS EKF. As stated above, this is basically due to the larger availability of at least a single aiding LOS, more than to the additional information provided by the second LOS. The

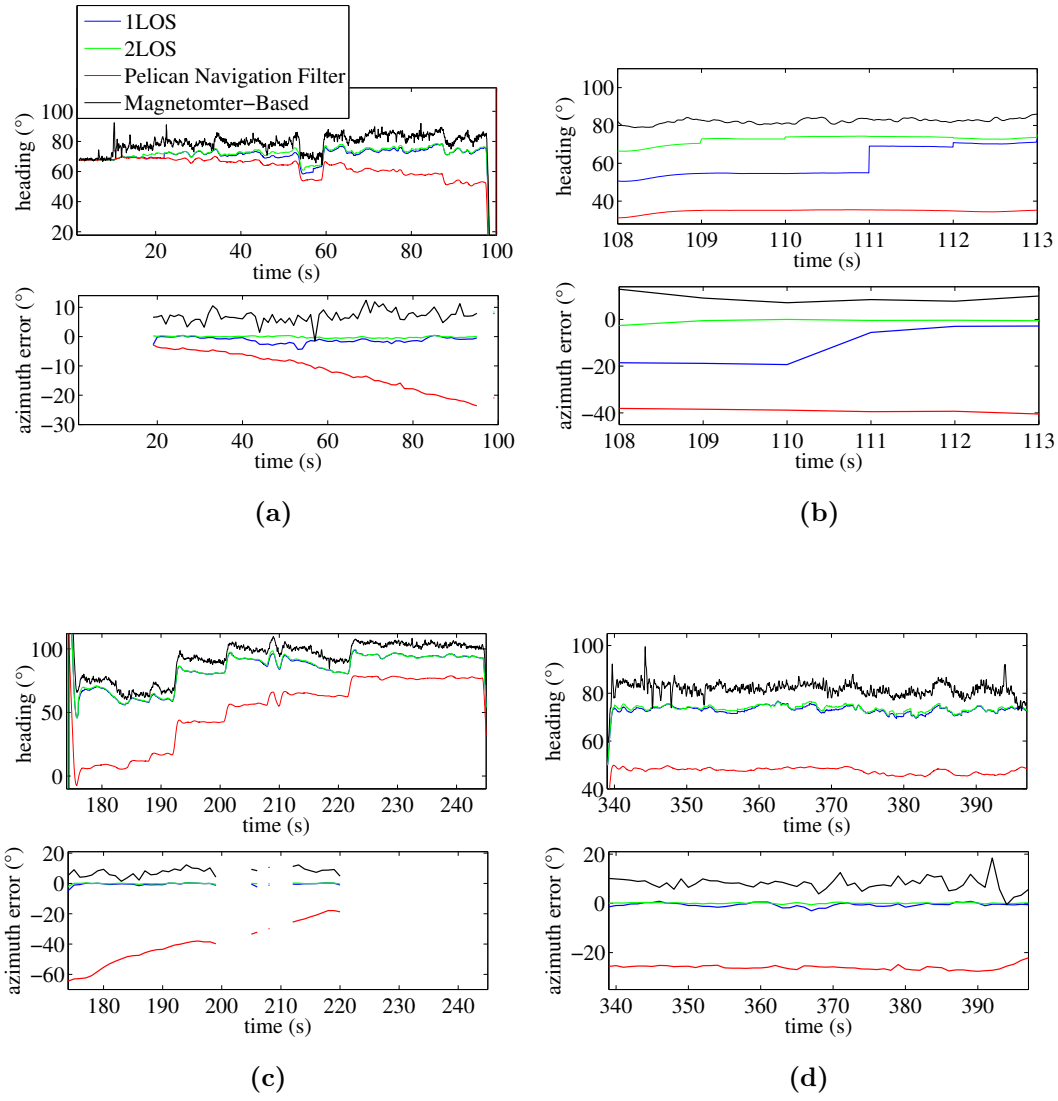

Figure 3.37: Heading angle as a function of time during (a) first (b) second (c) third (d) fourth flight segments.

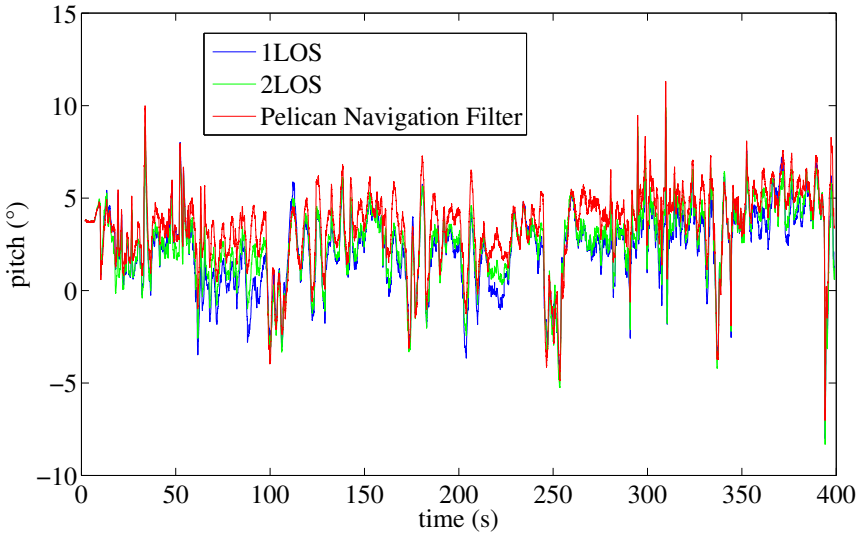

Figure 3.38: Pitch as a function of time (Test 3).

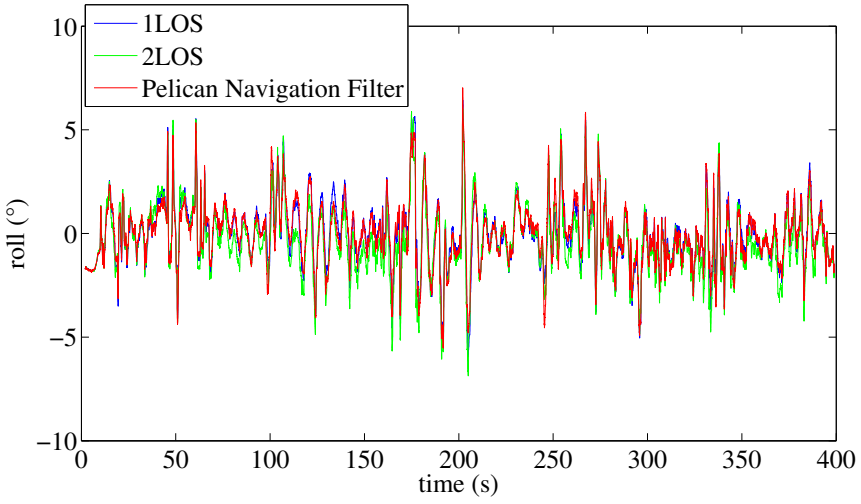

Figure 3.39: Roll as a function of time (Test 3).

Table 3.5: Pointing Accuracy Statistics.

		Azimuth Error [◦]	Elevation Error [◦]
1 LOS	Mean	−0.8	−0.4
	Std	1	0.8
	RMSE	1.2	0.9
2 LOS	Mean	−0.06	−0.04
	Std	0.7	0.6
	RMSE	0.7	0.6
Pelican Navigation Filter	Mean	−28	0.9
	Std	14	0.8
	RMSE	32	1.2

average performance of the Pelican navigation filter in azimuth differs by more than an order of magnitude.

As regards elevation, again the 2 LOS filter shows the best performance in terms of Root Mean Square Error (RMSE), followed by the 1 LOS EKF and the Pelican navigation filter. In this case, the limited performance differences, and the larger benchmark uncertainty, allow concluding that degree-level accuracy is achievable by all developed architectures.

Given the higher accuracy achievable when 2 LOS are integrated within the EKF, in the following it is also interesting to analyze the performance of the DGPS/Vision processing when 2 LOS and the CDGPS solution are adopted. To this end, in Figure 3.40 and Figure 3.41 a comparison between the attitude accuracy achievable with the code-based DGPS, and CDGPS is performed.

Again, azimuth accuracy depends primarily on heading measurements performance, while the elevation accuracy depends on pitch and roll performance.

From Figure 3.40 and Figure 3.41 it is clear that the higher accuracy (horizontal and vertical) of the CDGPS solution increases the yaw, pitch and roll attitude

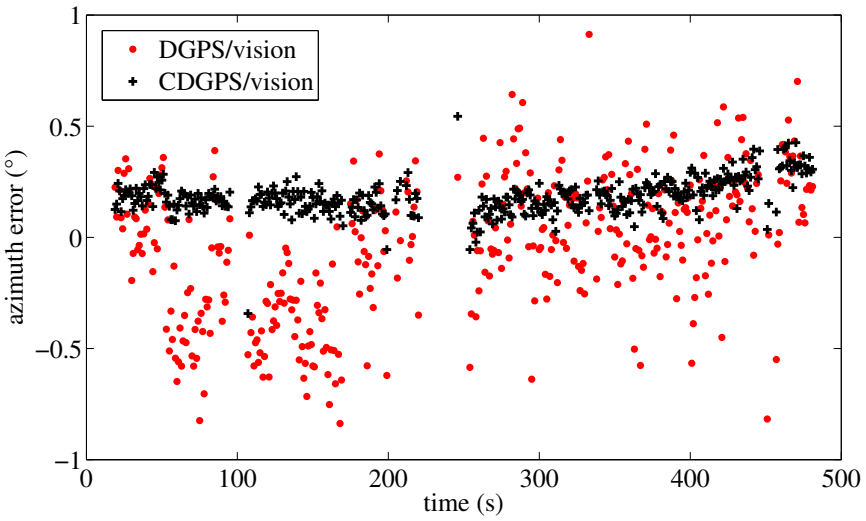

Figure 3.40: DGPS/Vision vs. CDGPS/Vision azimuth error as a function of time (Test 3).

accuracy. In fact, by analyzing the azimuth (heading) error, the CDGPS/Vision presents a mean error of 0.1 degrees with a standard deviation of about 0.08 degrees (Table 3.6), far better than the one achieved by adopting a code-based DGPS (standard deviation of about 0.7 degrees Table 3.5).

A similar result is shown for pitch and roll performance where a significant improvement is provided by the CDGPS/Vision measurements due to the increased vertical accuracy of the CDGPS solution with respect to the code-based DGPS one. In fact, the standard deviation of the CDGPS/Vision elevation error is 0.18 degrees (Table 3.6), while the DGPS/Vision presents a standard deviation of 0.6 degrees (Table 3.5).

In conclusion, experimental results show that the integration of the CDGPS solution, within the cooperative navigation approach, permits achieving high accurate attitude estimates which can bring significant advantages to all those applications where fine sensor pointing is required.

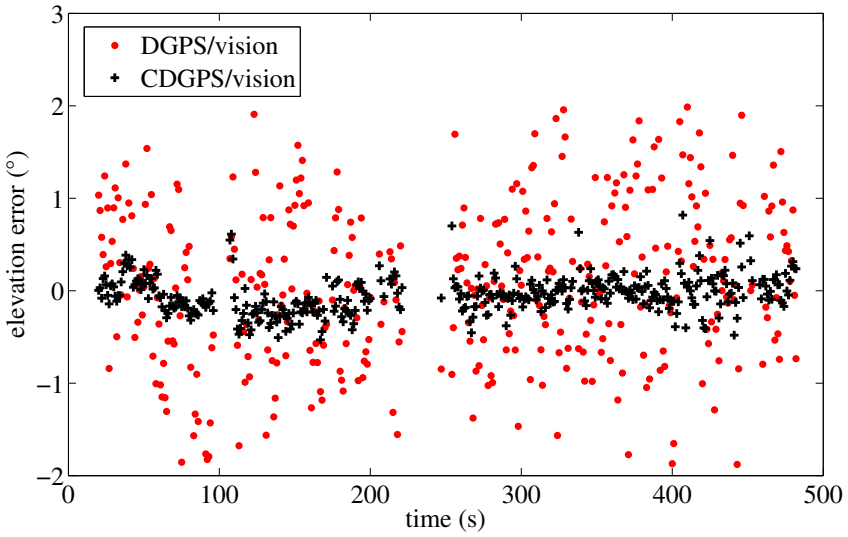

Figure 3.41: DGPS/Vision vs. CDGPS/Vision elevation error as a function of time (Test 3).

Table 3.6: Pointing Accuracy Statistics CDGPS.

		Azimuth Error [∘]	Elevation Error [∘]
2 LOS CDGPS/Vision	Mean	0.1	−0.05
	Std	0.08	0.2
	RMSE	0.2	0.2

Chapter 4

Cooperative Navigation in GPS-Challenging Environments

While in the previous chapter it was assumed that all UAVs of the formation were flying under nominal GPS coverage, here, the focus is set on UAV navigation in environments where it is difficult, or impossible, for GPS receivers to track satellite signals. These environments are defined as GPS-challenging or GPS-denied, respectively [69]. In fact, in certain cases, UAVs missions involve operations in particular environments such as natural and urban canyons, or mixed outdoor-indoor settings, that can determine multipath or shadowing of the GPS satellite signal. As a consequence, the GPS receiver can be unable to generate a position fix, since less than four pseudoranges are available [9].

The absence of a valid position fix prevents the navigation system to bound the errors deriving from successive integration of inertial sensors measurements. Furthermore, since small UAVs are usually equipped with low performance low cost inertial MEMS sensors, position error drift is fast, making the system unreliable for many applications.

In these conditions, it is necessary to rely on a non-GPS backup or alternative navigation system, that is, a system which combines inertial sensors information

with those provided by an aiding sensor.

The solution adopted in this research activity is based on coupling cooperative navigation and vision-based techniques. In particular, in [70], a micro-UAV flying in GPS denied/challenged conditions is supported by (at least one) cooperative aircraft under nominal GPS coverage, thanks to position information broadcast and vision-based relative sensing (which avoids the need of inter-vehicle ranging systems to be installed on all the vehicles). As it is intuitive, while exploiting two or more cooperative UAVs allows triangulating the position of the micro-UAV in GPS denied conditions, in general aiding measurements from a single cooperative UAV do not allow eliminating position error drift, due to the absence of direct information provided along the LOS. This issue can be solved either integrating valid pseudorange measurements in the navigation filter, or exploiting ad hoc commanded motion of the cooperative vehicle under GPS coverage.

A second approach, proposed in [71], consists in combining within a sensor fusion algorithm cooperative navigation with vision-inertial SLAM, in order to compensate drawbacks of each method and effectively counteract position error drift.

4.1 Related Work

As already mentioned, in GPS-challenging environments, additional aiding information must be provided to reduce or eliminate the navigation error drift. Several approaches can be used to this aim [72], such as vision-aided navigation [73, 74], positioning based on cell phone signals [75], and cooperative navigation [76].

Over the past decade, computer vision has played an important role in both control and navigation of UAVs [77]. Vision-aided navigation methods are usu-

ally based on the use of a single camera (monocular) or multiple cameras (stereo). Stereo-vision systems have been successfully applied for micro-UAVs navigation [78, 79], but the baseline between cameras limits the possible altitude range [80]. Monocular vision also offers a good solution in terms of weight, accuracy and cost, however, the need to solve the scale factor makes it necessary to fuse data with other sensors [81].

In general, visual-inertial navigation and simultaneous localization and mapping (SLAM) represent widely investigated topics in literature [73, 74, 82]. In spite of assessed theoretical foundations and processing strategies, issues for implementation onboard micro-UAVs still remain involving possible localization ambiguities, consistency of self formulated uncertainty estimates, computational load (and thus real time capabilities) and sensitivity to illumination and environmental conditions. Moreover, as a matter of fact optical/inertial measurements cannot avoid scale drift phenomena, unless flight is constrained in a relatively limited area, which limits mapping errors for the geolocated ground features. A possible solution for scale drift phenomena consists in integrating range sensors such as radar or LIDAR altimeters, which however may pose other challenges related to available onboard budgets and the three-dimensional structure of the mission environment [82].

A further solution is represented by positioning systems based on cell phone signals, in which the ubiquity of cell phone towers is exploited to infer the position of UAVs. In fact, knowledge of position coordinates of the cell phone towers allows a traditional multi-lateration approach to determine the UAVs position [72]. The two major advantages of this approach are that, positions of cell phone towers are known in urban settings and that the necessary technology to extract information from cell phone signals already exists. The main drawbacks are related to signal coverage which may be sparse in certain geographical areas and that many technical issues concerning the multi-lateration method need more

research and studies.

All the aforementioned techniques involve a single vehicle architecture, a different approach consists in exploiting cooperative navigation, taking advantage from companion aircraft within a multi-UAV scenario. Cooperative navigation approaches differ in terms of informations exchanged among the vehicles (i.e. in terms of sensors adopted for generating the navigation solution and/or in terms of the relative measurements).

Many researchers involved in cooperative systems have focused their attention on the task of Cooperative Localization (CL). This is of paramount importance in applications in which a precise formation geometry is required. In [83] cooperative navigation in GPS-denied areas is performed acquiring overlapping images of the scene from different UAVs in which at least one of them has GPS coverage. Once blob features [84] have been matched among those images, it is possible to recover UAVs relative positions and consequently the absolute position of each vehicle. A similar approach has been followed in [85] and [86] in which overlapping views are processed in order to evaluate relative positions in swarms.

The main drawback of all these vision-based approaches is the necessity to detect and track natural or manmade features in a sequence of overlapping images which require a static and textured scene in good illumination conditions.

Another cooperative navigation approach [72], requires positions broadcast from UAVs and range measurements obtained from signal round trip timing. In this way, the combined range and location information can help mitigate the error growth of the low-cost IMU on board the UAVs.

This work derives from a different approach, which consists in exploiting cooperative navigation, where a micro-UAV flying in GPS denied/challenged conditions is supported by (at least one) cooperative aircraft under nominal GPS coverage, thanks to position information broadcast and vision-based relative

sensing (which avoids the need of inter-vehicle ranging systems to be installed on all the vehicles). As it will be clarified in the following, this approach reduces formation keeping requirements, with respect to the above mentioned CL techniques, and permits to exploit the motion of the cooperative vehicle under GPS coverage to increase navigation observability.

4.2 Cooperative Navigation Approaches

As stated above, in this chapter cooperation is exploited to improve UAVs autonomy in GPS-challenging environments. The proposed architecture couples cooperative navigation and vision-based techniques, and is based on the idea of carrying out complex missions by distributing functions among different flight platforms.

In particular, a formation of at least two cooperating UAVs is considered. In the following, one or more UAVs are defined as "father(s)", the other(s) are named as "son(s)".

It is assumed that

- reliable continuous position measurements are available at father(s), i.e., father aircraft are flying in outdoor areas and are not susceptible to GPS signal absorption, jamming, and multipath phenomena, or, in case of temporary GPS signal corruption, high accuracy avionics are embarked on board the father in order to bound position drifts;

- son UAVs operate in GPS-challenging environments, thus they are not able to exploit at least four valid pseudorange measurements and use them to obtain a reliable GPS position fix.

As better detailed in the following, in some cases it will be assumed that less than four valid pseudorange measurements are also available at son UAVs,

in order to analyze the effect of this additional information in the considered navigation architecture. From a practical point of view, this means that proper strategies are adopted to avoid using unreliable measurements.

In this section two navigation architectures are presented. The first one integrates only measurements coming from cooperative UAVs, while the second one combines within a sensor fusion algorithm cooperative navigation with vision-inertial SLAM.

4.2.1 Cooperative Navigation

The main objective of the developed architectures and algorithms is to allow safe and reliable navigation for son UAVs by exploiting line-of-sight information available at formation level.

A conceptual view of the considered scenario, in the case of a 2 vehicle formation, is shown in Figure 4.1. For the sake of image clarity, Figure 4.1 shows the father UAV flying at higher altitude than the son. Indeed, the implemented concept may not require this altitude difference, whose necessity basically depends on the mission scenario and the three-dimensional structure of the environment. Thus, the implemented concept has some differences with respect to the one of asymmetric formations based on high flying/low flying vehicles [76], and the difference between father and son is based only on their operating environment in terms of GPS coverage. Also, the developed concept can be achieved by identical, similar, or significantly different aircraft (e.g., rotary and fixed wing aircraft).

It is clear that a fundamental prerequisite, for these cooperative navigation architectures, is that the LOS between son and father(s) must not present any obstruction. In fact, LOS, allows father and son UAVs to interact by means of two basic mechanisms:

- Information sharing: it is assumed that a proper data link exists be-

tween father and son to allow the transmission of the required information, mainly the father GPS-based position estimate. Furthermore, when the father vehicle is in charge of air-to-air visual tracking, the estimated son-to-father visual LOS is also transmitted to the son. Indeed, from the navigation point of view, this is a one-way information exchange. Instead, communication from the son to the father has to be foreseen if cooperative navigation is integrated with autonomous cooperative guidance;

- Relative sensing: as anticipated above, it is assumed that this is based on machine vision. Though cameras cannot provide direct range measurements, they represent an appealing solution for the problem at hand. High resolution cameras based on CCD or CMOS detectors represent a well assessed technology that is accessible at low cost and with very small size, weight, and power budgets. Furthermore, within the limits of the trade-off between angular coverage and resolution, they can work with a rather large field of view (FOV), thus reducing or eliminating the necessity of sensor pointing. Depending on the considered coverage and scenario, they can also work with more than a single father/son. Finally, the angular information can be properly integrated with other information sources and/or dynamic strategies, in order to ensure observability and thus to fulfil navigation accuracy requirements.

In general, in the case of a temporary loss of LOS or communications/tracking, cooperative aiding cannot be exploited. The resulting navigation error drift will then depend on duration of outages and the performance of son avionics systems.

Given these basic principles, two different architectural solutions can be envisaged. In fact, the optical system aimed at relative sensing can be installed either on board the father, or on the son UAV. Both approaches have pros and cons.

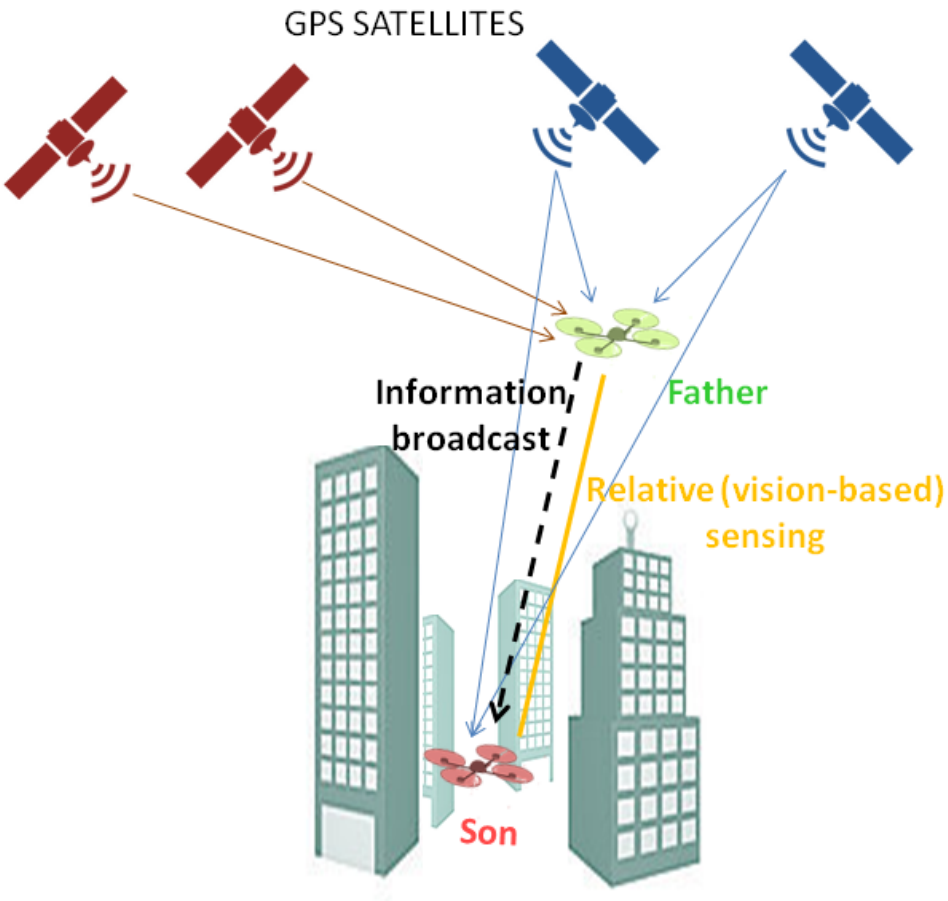

Figure 4.1: Conceptual view of cooperative navigation scenario in GPS-challenging environments.

The first approach allows tracking and navigation to be carried out separately. In fact, the tracking task is performed by the father, within a relatively common vision-based air-to-air target tracking problem. Conceptually, the LOS derived in this way depends only on the current son position. On the other hand, measurement covariance includes position and attitude/pointing uncertainty of the father. This choice may be convenient if the father vehicle has better navigation and optical sensing performance than the son, i.e., it can exploit more accurate inertial sensors and/or optical cameras and gimbals with larger detection range and better pointing accuracy. However, some tracking issues may arise if the son has to be tracked against a cluttered background.

A single bearing measurement obtained in this way cannot be directly exploited for son positioning, as it does not give any information along the LOS (we are assuming that it is not possible to estimate range accurately on the basis of son appearance in the images). Having two fathers it is possible to directly triangulate son position. More than two fathers enable triangulation with a least squares approach. However, an interesting approach for son positioning on the basis of single LOS information consists in exploiting passive ranging strategies [87] to make range observable. Basically, it is necessary that the father maneuvers generating an acceleration component in the direction orthogonal to the LOS. Once the range is considered observable (based on the estimated covariance of the tracking filter), the range information can be transferred, thus effectively giving 3d position information to the son. In all cases, when the information about absolute position of the father and relative LOS is transmitted to the son, this is used within the son navigation filter as an additional aiding measurement.

In the second approach, both vision-based tracking and navigation computations are carried out on the son vehicle. This may imply that the son UAV requires additional optical sensors and processing capabilities, with respect to

the ones needed for mission execution. Miniaturization of cameras and processing units can make the concept applicable even on very small UAVs, although it is likely that the son UAV will embark (compared with the father) less performing cameras installed in strapdown configuration or within less performing gimbals. In spite of these possible hardware differences, vision-based tracking issues can be reduced by a more favourable operating environment, when the father flies against sky background. The LOS information derived by the son includes both attitude and position information, as it resembles the classical concept of vision-aided navigation, although with mobile flying features whose absolute position is provided in broadcast, instead of being known a priori, or triangulated exploiting own-ship motion. Having several fathers is thus equivalent to exploiting several features. A key difference with classical vision-aided navigation is that father dynamics can be exploited to the navigation advantage, implementing a concept similar to passive ranging. This son-centered approach to cooperative navigation requires only father position to be transmitted. Basically, besides GPS, only a data link capability is requested, which could exist without any specialized hardware (e.g., ADS-B Out equipment could suffice for cooperative navigation needs). Furthermore, in theory a single father can be simultaneously exploited by several sons, and even non-cooperative UAVs with broadcasting capability could be used as "fathers of opportunity".

In this thesis, the son-centered cooperative navigation approach has been developed. It is also considered the case of a single father UAV, in order to minimize system complexity and investigate son navigation performance in the case of single LOS aiding alone or combined with valid pseudorange measurements and/or father maneuvers.

4.2.2 Cooperative Navigation and vision-based SLAM

The main idea behind this approach is to allow safe autonomous navigation for the son UAV by simultaneously exploiting standalone vision-aided localization and vision-based cooperative navigation techniques. This permits to overcome limitations of both techniques, reducing the position error drift.

The difference with respect to the above mentioned approach is that, here the son vehicle is equipped with a vision sensor (e.g., a nadir looking camera) to detect and track manmade or natural features along the flight path, and to perform visual SLAM based on these features (Figure 4.2).

Regarding cooperative navigation this consists again of two main components: information sharing; relative sensing.

From the technological point of view, while in theory a single camera can be used to track both ground features and the father vehicle, it is likely that a multi-camera architecture is needed on board the son Figure 4.2.

The LOS information derived by the son includes again both attitude and position information. Indeed, the additional information content provided by the son-to-father LOS may appear limited compared with the number of features typically employed in visual SLAM processing. However, a key difference with respect to ground based features is that father absolute position is provided in broadcast instead of being triangulated exploiting own-ship motion, and as such it is not sensitive to error accumulation phenomena. Also, the father UAV can be properly maneuvered to increase the son navigation state observability.

4.3 Logical Architectures and Algorithms

As regards the algorithmic architecture, a sensor fusion approach is developed which combines inertial (INS)/magnetic (MAG) measurements, cooperative LOS measurements and, if available, standalone vision-based estimates to improve

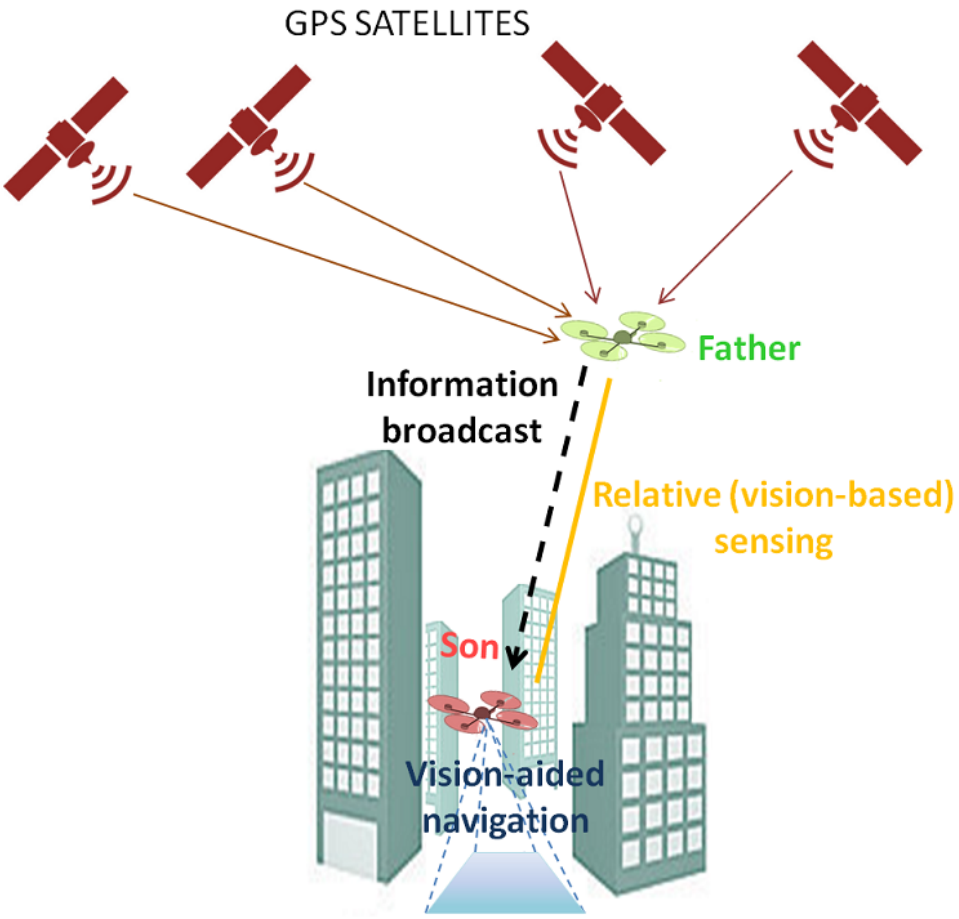

Figure 4.2: Conceptual view of cooperative navigation and SLAM scenario in GPS-challenging environments.

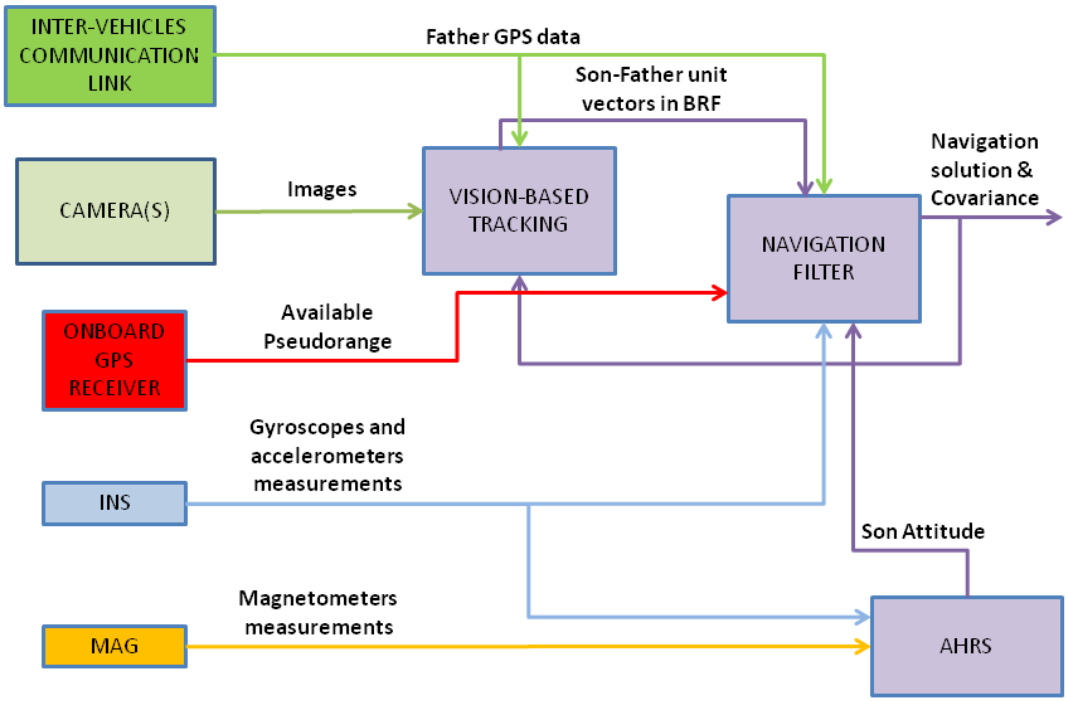

Figure 4.3: Logical architecture of line-of-sight approach in GPS-Challenging environment.

navigation accuracy and integrity.

Figure 4.3 and Figure 4.4 show the logical architectures of the two proposed approaches. In both cases, the core of the algorithm is the navigation filter that runs on the son vehicle.

In particular, the EKF combines inputs from the onboard inertial and magnetic sensors, measurements coming out from an attitude and heading reference system (AHRS) filter, son-to-father unit vector in BRF as evaluated by vision-based tracking, and GPS-based father position information. In addition, in the first architecture shown in Figure 4.3, also GPS pseudorange measurements (if available) are integrated within the EKF, while in Figure 4.4, we assume that there is no GPS coverage and a SLAM-based monocular pose estimation is adopted as aiding system.

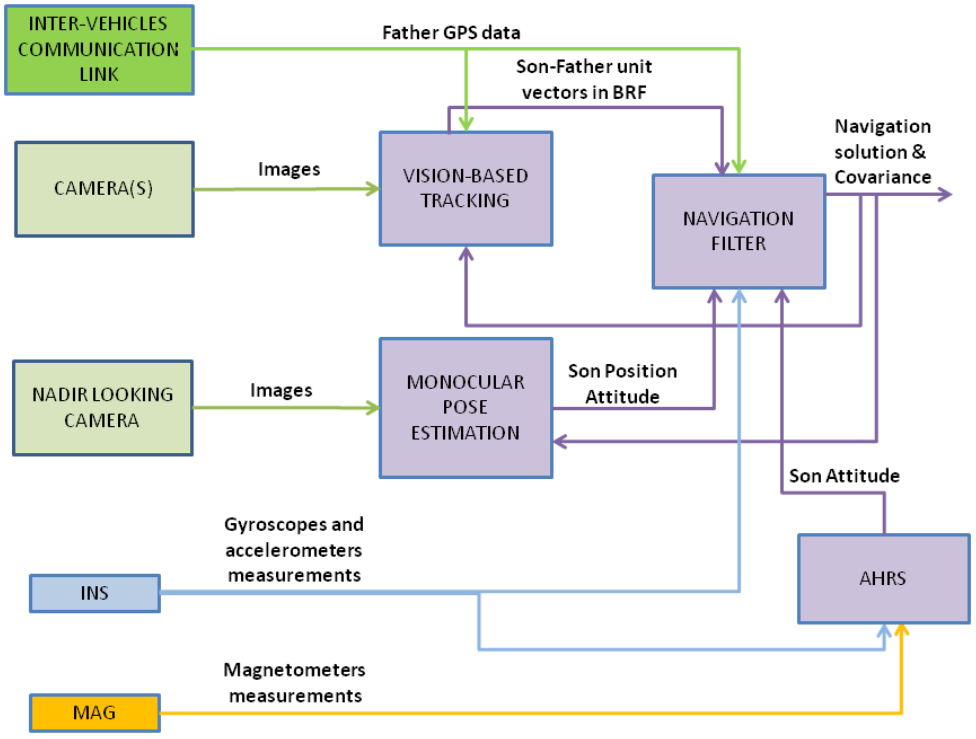

Figure 4.4: Logical architecture of line-of-sight approach + SLAM in GPS-Challenging environment.

In the following, for the sake of mathematical simplicity it is assumed that the camera is installed in a strapdown configuration, and it is aligned with the BRF. Actually, the same processing architecture can be adopted for any strapdown installation geometry, and also for gimbaled installations (assuming accurate real time knowledge of gimbal pointing angles).

4.3.1 Line-of-Sight Measurement Update

In this section, the focus is set only on the tight integration of LOS measurements within the EKF, which couples the navigation system position error and the navigation attitude errors into the measurement process [88]. More details about the EKF can be found in subsection 3.3.4.

When the father is identified in the image by the vision-based tracking algorithm, son-to-father LOS (subsection 3.3.1) is established and it is possible to compute the azimuth and elevation measurement residuals to be integrated into the EKF linearized observation model

$$\delta Az = Az_{measured} - Az_{predicted} \tag{4.1}$$

$$\delta El = El_{measured} - El_{predicted} \tag{4.2}$$

where $Az_{measured}$ and $El_{measured}$ are the azimuth and elevation in BRF obtained by the vision-based tracking system (Figure 4.3 and Figure 4.4) and the predicted ones are obtained from the known GPS father position (transmitted to the son) and the predicted/propagated son position.

The predicted azimuth and elevation ($Az_{predicted}$; $El_{predicted}$) are related to the son-to-father relative position vector expressed in the son body reference frame $\Delta\underline{\bar{r}}^{BRF}$, where $\Delta\underline{\bar{r}}^{BRF}$ is given by

$$\Delta\underline{\bar{r}}^{BRF} = \underline{\underline{R}}^{b}_{n}\underline{\underline{R}}^{n}_{e}\Delta\underline{\bar{r}}^{ECEF} \tag{4.3}$$

in which, the overbar represents the output of the navigation system, $\underline{\underline{R}}_n^b$ is the rotation matrix from the navigation to the body reference frame, $\underline{\underline{R}}_e^n$ is the rotation matrix from the ECEF to the navigation frame, and the relative position vector in ECEF reference frame is

$$\Delta\bar{\underline{r}}^{ECEF} = \begin{bmatrix} (R_n + h_f)\cos\phi_f \cos\psi_f - (R_n + \bar{h}_s)\cos\bar{\phi}_s \cos\bar{\psi}_s \\ (R_n + h_f)\cos\phi_f \sin\psi_f - (R_n + \bar{h}_s)\cos\bar{\phi}_s \sin\bar{\psi}_s \\ [R_n(1-e^2) + h_f]\sin\phi_f - [R_n(1-e^2) + \bar{h}_f]\sin\bar{\phi}_s \end{bmatrix} \tag{4.4}$$

In Equation 4.4, (ϕ_f, ψ_f, h_f) are the father UAV geodetic position coordinates which are transmitted to the son, ($\bar{\phi}_s$, $\bar{\psi}_s$, $\bar{h}_s$) are the estimated son UAV geodetic position coordinates, R_n is the earth normal radius and e is the eccentricity.

From Equation 4.3 it is possible to compute the predicted azimuth and elevation angles exploiting the following relations

$$Az_{predicted} = \tan^{-1}\left(\frac{\Delta y^b}{\Delta x^b}\right) \tag{4.5}$$

$$El_{predicted} = \tan^{-1}\left(\frac{-\Delta z^b}{\sqrt{(\Delta x^b)^2 + (\Delta y^b)^2}}\right) \tag{4.6}$$

where Δx^b, Δy^b and Δz^b are the $\Delta\bar{\underline{r}}^{BRF}$ components.

It is important to underline that, as shown in Equation 4.3 and Equation 4.4, predicted azimuth and elevation angles contain the dependency on son position and attitude state variables.

A further customization of the EKF observation model derives from the assumption that son dynamics does not foresee significant accelerations, compared with gravity. Hence, besides exploiting magnetometers to compute vehicle heading, it is possible to use accelerometers measurements to have a relatively rough estimate of pitch and roll angles. As a consequence, the measurement vector, representing the difference between the true measurements and the measure-

ments estimated from the propagated state vector is

$$\delta \underline{z} = \begin{bmatrix} \delta PR_1 \\ \cdots \\ \delta PR_n \\ \delta Az \\ \delta El \\ \epsilon_{accmag,n} \\ \epsilon_{accmag,e} \\ \epsilon_{accmag,d} \end{bmatrix} \tag{4.7}$$

where:

- δPR_s is the pseudorange measurement residual for the s-th satellite computed as the difference between the measured range for the s-th satellite and a pivot satellite, minus the predicted difference (n measurements are available if $n+1$ satellites are in view);

- $\epsilon_{accmag,n}$, $\epsilon_{accmag,e}$ and $\epsilon_{accmag,d}$ are the residuals relevant to attitude measurements provided by accelerometers and magnetometers;

- δAz and δEl are the LOS measurement residuals presented in Equation 4.1 and Equation 4.2.

The measurement matrix $\underline{\underline{H}}_k$, at the k-th time instant, is given by

$$\underline{\underline{H}}_k = \begin{bmatrix} \underline{\underline{H}}_n & \underline{\underline{0}}_{n\times 3} & \underline{\underline{0}}_{n\times 3} \\ \dfrac{\partial Az}{\partial \delta p} & \underline{0} & \dfrac{\partial Az}{\partial \rho} \\ \dfrac{\partial El}{\partial \delta \underline{p}} & \underline{0} & \dfrac{\partial El}{\partial \underline{\rho}} \\ \underline{\underline{0}} & \underline{\underline{0}} & \underline{\underline{I}}_3 \end{bmatrix} \tag{4.8}$$

in which: $\underline{0}$ is a 1×3 null elements vector; $\underline{\underline{0}}_{n\times 3}$ is the $n \times 3$ null matrix; $\underline{\underline{I}}_3$ is a 3×3 identity matrix; $\underline{\underline{0}}$ is a 3×3 null matrix; $\underline{\underline{H}}_n$ is given by Equation 3.25;

and the partial derivatives $\frac{\partial Az}{\partial \delta \underline{p}}$ and $\frac{\partial Az}{\partial \underline{\rho}}$ represent, respectively, the derivatives of the azimuth measurement with respect to the position error vector and with respect to the attitude error vector, the same applies for the elevation partial derivatives.

When measurements are available, the measurement update phase is carried out using the standard Kalman filtering equations (Equation 3.52, Equation 3.53), leading to an estimate of the measurement error that is then subtracted to vehicle position, velocity and attitude to provide the final estimate.

Concerning the filter tuning, the process noise matrix $\underline{\underline{Q}}$ is obtained on the basis of inertial sensor specifications, while the measurement noise covariance matrix $\underline{\underline{R}}$ is built on the basis of magnetometers and accelerometers performance, pseudoranges uncertainties, and LOS measurements uncertainties.

In particular LOS Az and El uncertainties depend on the EO and the father GPS-based performance (σ^2_{EO} and σ^2_{GPS}), as well as the distance from the father L. Assuming uncorrelated measurements we have

$$\sigma^2_{Az} = \sigma^2_{Az,EO} + \sigma^2_{Az,GPS} \tag{4.9}$$

$$\sigma^2_{El} = \sigma^2_{El,EO} + \sigma^2_{El,GPS} \tag{4.10}$$

where

$$\sigma_{Az,GPS} \cong \frac{\sigma_{GPS,hor}}{L} \tag{4.11}$$

$$\sigma_{El,GPS} \cong \frac{\sigma_{GPS,ver}}{L} \tag{4.12}$$

and *hor* and *ver* refer to the horizontal and vertical components of σ^2_{GPS}. Both Equation 4.11 and Equation 4.12 indicate that the azimuth and elevation measurement uncertainties increase as the son-to-father distance decreases. In addition, it is worth noting that Equation 4.11 contains a conservative approach as the reported azimuth uncertainty is obtained in worst case geometries.

4.3.2 Monocular Pose Estimation

Monocular pose estimation is the problem of determining the time variation of position and attitude parameters of the son UAV with respect to a navigation frame, by processing images acquired by a single camera. This task is carried out by exploiting a customized visual SLAM approach which relies on feature-based algorithms for localization and mapping running at different update rates.

The detailed architecture of the pose estimation block included in the navigation framework proposed in this work is shown in Figure 4.5, where the exchange of information with the navigation filter block is also highlighted.

Specifically, the localization algorithm requires an initial pose solution, which is provided by the prediction step of the navigation filter, in order to generate an updated set of pose parameters. This updated pose represents an additional measurement information for the navigation filter. Conversely, the mapping function relies on multiple sets of pose parameters estimated by the correction step of the navigation filter during a specific time interval. Before entering the details of the techniques implemented for localization and mapping, it is worth outlining that both these two functions of the proposed visual SLAM framework, rely on the capability of correctly detecting and tracking features from the images acquired by a monocular camera system. Several techniques have been proposed in the open literature for extracting different kinds of image features, such as corners [89] or more complex descriptors [90, 91], as well as for feature tracking [46]. However, these tasks still involve significant technical challenges for practical implementation of visual SLAM approaches, especially for UAVs flying in outdoor environment due to the sensitiveness of visual sensor from ambient light variations. As this work focuses on demonstrating the potential advantages of estimating the navigation state of an UAV by combining cooperative and standalone vision-based information, the above-mentioned image processing tasks are not considered in the following.

Vision-based localization is the problem of estimating position and attitude of the UAV with respect to a navigation frame. This task is typically tackled by looking for correspondences between 2d features extracted from a single image and 3d objects whose location in the navigation frame is given by a map of the observed environment which is stored/built on board. If $\underline{s} = (u, v)^T$ is a generic image feature expressed in normalized image coordinates and $\underline{q} = (q_N, q_E, q_D)^T$ is the corresponding 3d object in the navigation frame, they are linked by

$$\underline{s} = \underline{\underline{K}}_{cam} \underline{\underline{R}}_b^c (\underline{\underline{R}}_n^b (\underline{q} - \underline{t}_n) + \underline{t}_{b,cam}) \tag{4.13}$$

where $\underline{\underline{K}}_{cam}$ is the camera intrinsic calibration matrix, $\underline{\underline{R}}_b^c$ and $\underline{t}_{b,cam}$ are the camera mounting parameters (i.e. the rotation matrix from body to camera reference frames and the camera position vector in the body frame, respectively), and $\underline{t}_n = (t_N, t_E, t_D)^T$ is the UAV position vector in NED. Once a number (N) of matches is found and tentative pose solution ($\underline{p}^t$) is given, it is possible to define the re-projection error (χ^2) as the sum of squared distances between the image points and the reprojections on the image plane of the corresponding 3d objects (according to the transformation defined by tentative pose solution). As the camera mounting parameters do not change during the flight in the case of a strapdown installation, and can be estimated by carrying out pre-mission calibration procedures, the camera and body reference frame are considered coincident and aligned in the following, for the sake of mathematical simplicity. Under this assumption, χ^2 can be estimated by

$$\chi^2(\underline{p}^t) = \sum_{i=1}^{N} \| \underline{s}^i - \underline{\underline{K}}_{cam} \underline{\underline{R}}_n^{b,t} (\underline{q}_i - \underline{t}_n^t) \|^2 \tag{4.14}$$

Hence, the goal of the localization algorithm is to find the set of position and attitude parameters which allows minimizing χ^2. Since, the quantity on the right-side of Equation 4.14 is a non-linear function of the pose parameters, χ^2 can be minimized in a least squares sense by using a customized implementation of the Levenberg-Marquandt (LM) algorithm [92].

As regards the mapping step of the visual SLAM framework, it consists in triangulating the geodetic 3d position of those 2d features which have been tracked along a certain sequence of frames. This task is tackled by implementing an $L2$ triangulation method [93] which has been proven to be applicable for UAVs flying in extended outdoor scenario [94]. Specifically, if a feature is tracked within a sequence of M frames, its 3d position $q_m = (q_{mN}, q_{mE}, q_{mD})^T$ can be estimated by iteratively solving the following equation

$$\begin{bmatrix} \frac{1}{\lambda_1}(u_1\underline{r}_{31} - \underline{r}_{11}) \\ \frac{1}{\lambda_1}(v_1\underline{r}_{31} - \underline{r}_{11}) \\ \vdots \\ \frac{1}{\lambda_M}(u_M\underline{r}_{3M} - \underline{r}_{1M}) \\ \frac{1}{\lambda_M}(v_M\underline{r}_{3M} - \underline{r}_{1M}) \end{bmatrix} \underline{q}_m = \begin{bmatrix} \frac{1}{\lambda_1}(u_1\underline{r}_{31} - \underline{r}_{11})t_{n1} \\ \frac{1}{\lambda_1}(v_1\underline{r}_{31} - \underline{r}_{11})\underline{t}_{n1} \\ \vdots \\ \frac{1}{\lambda_M}(u_M\underline{r}_{3M} - \underline{r}_{1M})t_{nM} \\ \frac{1}{\lambda_M}(v_M\underline{r}_{3M} - \underline{r}_{1M})t_{nM} \end{bmatrix} \tag{4.15}$$

where λ_i, (u_i,v_i) and $(\underline{r}_{1i}, \underline{r}_{2i}, \underline{r}_{3i})$ represent the scale factor, the normalized feature coordinates, and the rows of the rotation matrix R_n^b for the i^{th} frame in the considered sequence. At the first step of the iterative process all the scale factors are set to 1, while starting from the second step they are updated exploiting

$$\lambda_i^{upd} = \underline{r}_{3i}(\underline{q}_t - \underline{t}_{ni}); i = 1 : M \tag{4.16}$$

This process is iterated until the convergence criterion is met

$$\sum_{i=1}^{M} |\lambda_i^{upd} - \lambda_i| < \epsilon \tag{4.17}$$

In the equation above, ϵ is a convergence threshold which can be set to be very small (e.g. 10^{-5} meters in this work).

As this triangulation process is similar to the concept of stereovision, it is clear that the larger the UAV displacement during the time interval between the first and last frame of the considered sequence in which a certain feature is tracked, the better the accuracy level of the triangulation process.

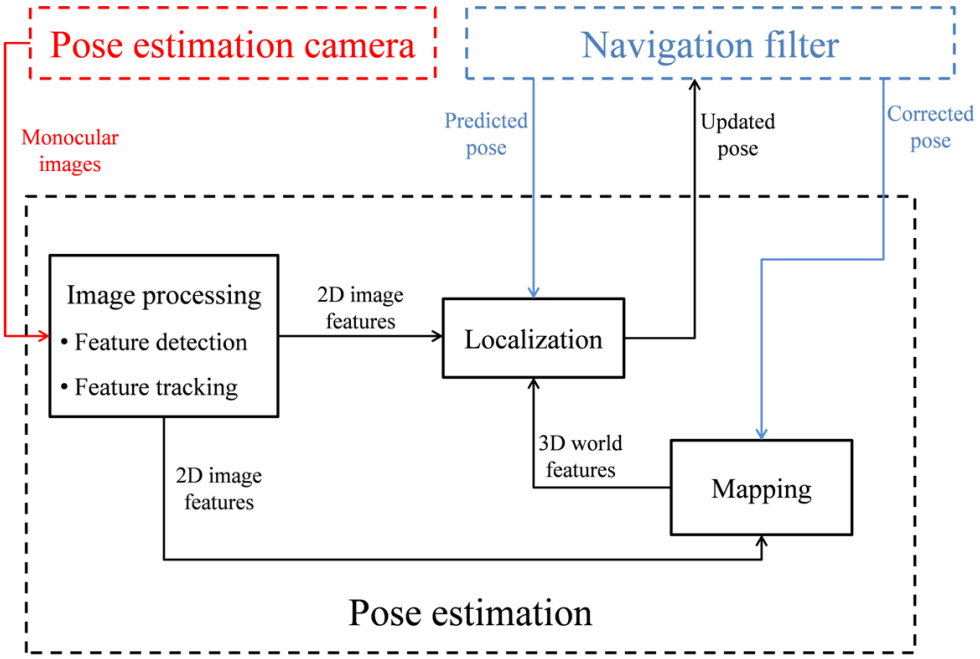

Figure 4.5: Detailed architecture of the pose estimation block.

4.4 Simulation Environment

The performance of the proposed autonomous navigation architecture has been preliminary assessed by means of numerical simulations.

To this aim, a simulation environment has been developed, which realistically reproduces the absolute trajectories of two UAVs, and the measurements provided by their on-board sensors. As regards the father vehicle, which is assumed to be under nominal GPS coverage, it is necessary to simulate the GPS position information which is broadcasted to the son.

The father GPS simulation process is summarized in Figure 4.6, where the GPS position uncertainty in NED is modeled as a non-zero-mean random error. Specifically, in order to take into account that GPS errors are correlated in time, the positioning error has been modeled as a constant bias plus a Gaussian white noise.

As regards the son vehicle, it is necessary to simulate the operation of both

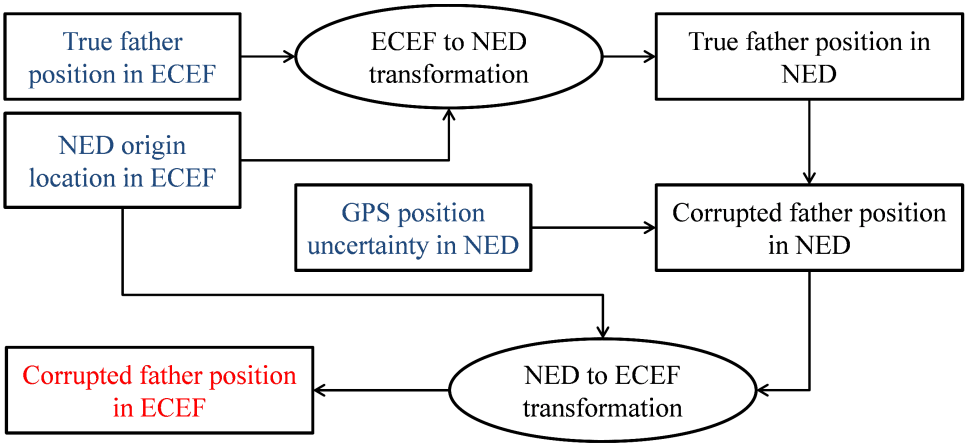

Figure 4.6: imulator of the father GPS position broadcasted to the son. The simulator input and output are highlighted in blue and red, respectively.

the target-tracking and, when available the SLAM cameras. The former is pointed towards the father and it is used to obtain its LOS in the body reference frame of the son. The simulation process is summarized in Figure 4.7, where the LOS uncertainty is modeled as a Gaussian white noise. Specifically, a standard deviation of 0.05° (which is equal to the IFOV of the simulated camera system) has been considered for both the azimuth and elevation components of the LOS.

As regards the SLAM camera, when the second navigation architecture (Figure 4.4) is considered, this is assumed to be mounted in nadir-looking geometry and it is used to detect and track ground features suitable to carry out autonomously localization and mapping. If the true features position in NED is assigned in input instead of the father position in NED, the simulation process is coincident to the one exploited to reproduce the operation of the target-tracking camera. However, in this case, the uncertainty in the feature detection process is modeled as a Gaussian white noise added to the feature position on the image plane. The parameters which determine the model exploited for the visual SLAM camera together with the standard deviation characterizing the noise on

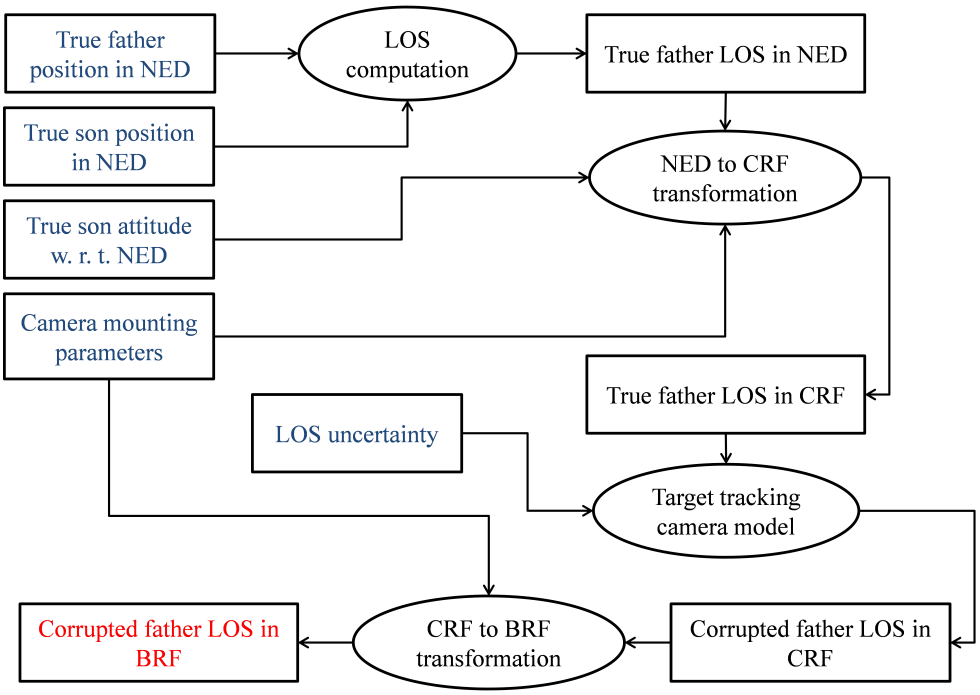

Figure 4.7: Simulator of the target-tracking camera. The simulator input and output are highlighted in blue and red, respectively.

Table 4.1: Model parameter of the SLAM camera.

Detection Size	2000×2000 pixel
Pixel dimension	$6 \cdot 10^{-6}$ m
Focal length	0.006 m
IFOV	$0.045°$
σ_{Pix}	5 pixel

Table 4.2: Inertial Sensors Bias and Random Errors.

Sensors	**Bias Instability**	**Random Walk**
Gyroscopes	$36°/h$	$4.6°/\sqrt{h}$
Accelerometers	$3 \cdot 10^{-4} m/s/h$	$0.06\ m/s/\sqrt{h}$

the feature position in the image (σ_{Pix}) are listed in Table 4.1.

As far as the son inertial sensors are concerned, these are simulated considering orders of magnitude of biases and random errors consistent with typical low cost MEMS sensors (Table 4.2). These measurements are then used in both AHRS and EKF filters.

In order to conclude this overview regarding the simulation environment, it is necessary to indicate the different update rates considered for the input to the navigation filter, and to clarify the strategy adopted for handling the features within the visual SLAM process. Specifically, the output of the AHRS filter is provided at 100 Hz while both the father LOS tracking and the localization algorithms are run at 10 Hz. As regards the mapping step, the map of the observed environment is updated by implementing the triangulation algorithm presented in subsection 4.3.2 every 2 seconds (at 0.5 Hz update rate). Only the features which are tracked over this entire time interval and are not present in the map (key features) are triangulated. Also, only three frames (the first, the

middle and the last acquired in the triangulation time interval) are considered in order to limit the computational cost while keeping the maximum baseline between the homologous observation of the same features in the scene. In order to initialize the SLAM process, a certain time interval (t_{INIT}), not longer than a few seconds, is assigned at the beginning of the simulation during which the son vehicle's pose is known with a given uncertainty. Thus, the features tracked during this time interval can be triangulated. This allows generating an initial map which can be used by the localization algorithm. This is the same as assuming that the son loses the GPS signal after an initial time, which may be plausible at the beginning of a mission scenario before entering in the GPS challenging area.

Before moving on to the results, it is important to outline that the idea of keeping fixed the update rate of the mapping algorithm, which is valid for the analyzed case studies, is not optimal for the SLAM process. Indeed, the decision of activating of the mapping function should dynamically adapt to variation in the vehicle's height and velocity in order to optimize the baseline for triangulation while avoiding loosing track of the features due to very large displacement.

4.5 Results

The simulation environment developed in section 4.4 gives the possibility to consider a wide variety of scenarios. In the following, for proof of concept, some particular cases are considered in which the chosen relative dynamics between son and father(s) put in evidence important results.

In addition, experimental results are presented by processing data acquired during the test 1 described in section 3.5.

4.5.1 EKF with cooperative aiding (Simulations)

The integration of the son-to-father LOS within the EKF has been tested through 100 numerical simulations.

In the performed analysis, since it is assumed that bounded attitude errors can be attained by exploiting accelerometers and gyroscopes, the major interest lies in evaluating the capability of cooperative navigation to reduce or eliminate position error drift. Thus, reported results focus on position error components in terms of mean error μ and standard deviation σ. In particular, latitude and longitude error variances are converted into Northing and Easting uncertainties computed assuming as origin the initial position of the son UAV.

Error estimates are useful to understand if a certain cooperative architecture can be adopted to fly safely in given GPS-challenging scenarios. In general, the cooperative concept can also be used in synergy with other systems/techniques, such as vision-aided navigation as it will be shown in subsection 4.5.2.

Three test cases have been considered, assuming a test duration of 300 seconds:

- Case 1: it is assumed that the flight is performed in a GPS-denied area, hence, no valid measurements from GPS satellites are available. There is 1 father vehicle that is moving in North direction at 10 m/s on a trajectory that is parallel to the one performed by the son UAV Figure 4.8. The initial displacement vector between the son and the father, in the son NED, is $[200, 0, -50]^T$ meters;

- Case 2: it is assumed that the son UAV is flying in a GPS-challenging environment, hence, by properly selecting a mask angle, valid GPS pseudo-range measurements from three satellites are available. In this simulation the father is moving in North direction at 10 m/s on a trajectory that is parallel to the one flown by the son Figure 4.8;

- Case 3: it is assumed that the son UAV is flying in a GPS-denied area and no valid measurements from GPS satellites are available. The son UAV is in hovering, while the father UAV describes a series of consecutive coordinated turns with a velocity of about 25 m/s Figure 4.9.

Figure 4.10 shows that single LOS aiding does not allow the navigation filter to significantly reduce the position error drift. In fact, given the assumed flight geometry, no direct positioning information is provided along North and Down directions. As a result, the accumulated error remains of the order of hundreds of meters in the considered simulation time. This effect is drastically mitigated assuming the availability of three valid pseudorange measurements (Figure 4.11, case 2). In this case, errors in East direction preserve the same order of magnitude of the previous case, while the drift in North and Down directions is eliminated.

As stated before, the practical availability of valid pseudorange measurements is not always ensured. Thus, it is interesting to evaluate the aiding capability of father dynamics (Case 3), which is done in Figure 4.12.

In this case, in spite of the absence of any pseudorange aiding, father dynamics allow eliminating position error drift and thus keeping a meter-level position accuracy within the whole simulation time.

Though the considered architecture is different with respect to classical passive ranging scenarios, it actually brings similar benefits in terms of relative position observability. In fact, oscillating LOS geometry generates similar oscillations in position errors.

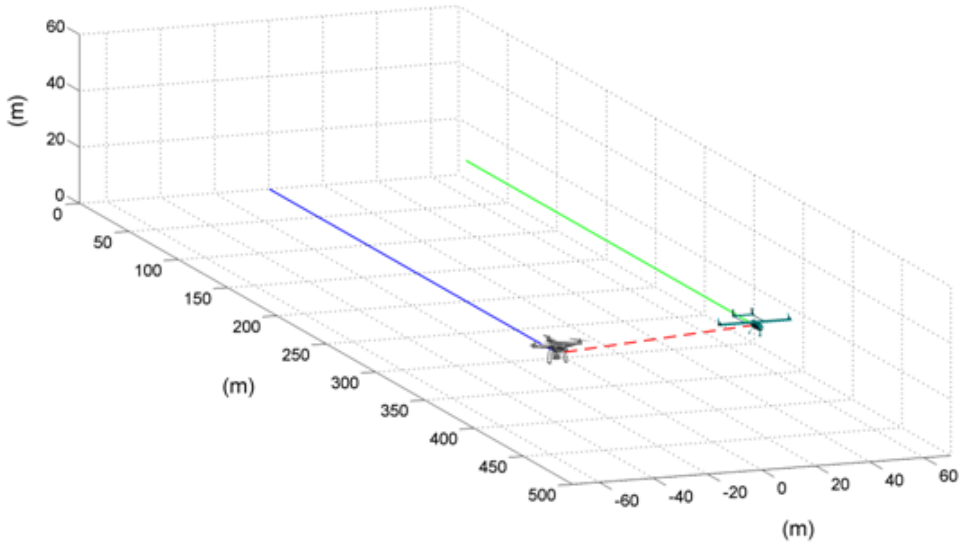

Figure 4.8: Son UAV (blue) and father UAV (green) trajectories represented in the son UAV initial NED reference frame. The red dashed line represents the LOS.

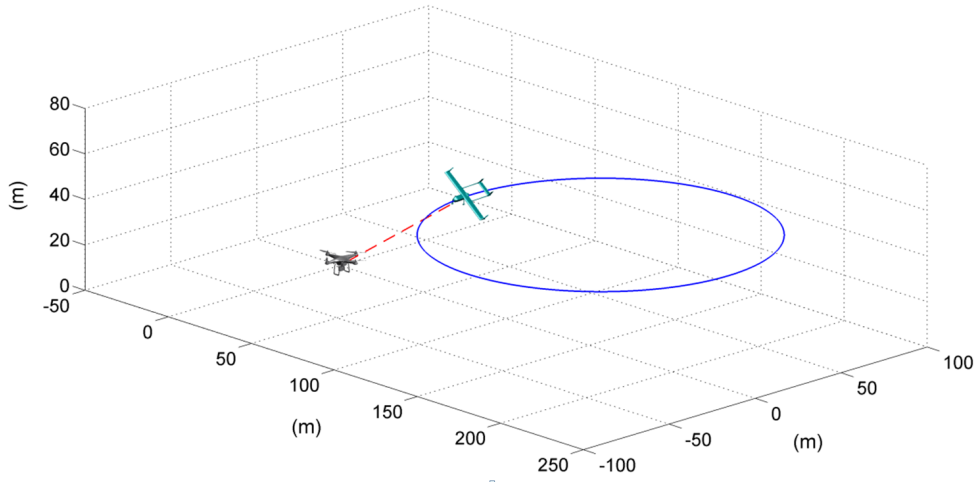

Figure 4.9: Son UAV in hovering wile father UAV is performing coordinated turns. The red dashed line represents the LOS.

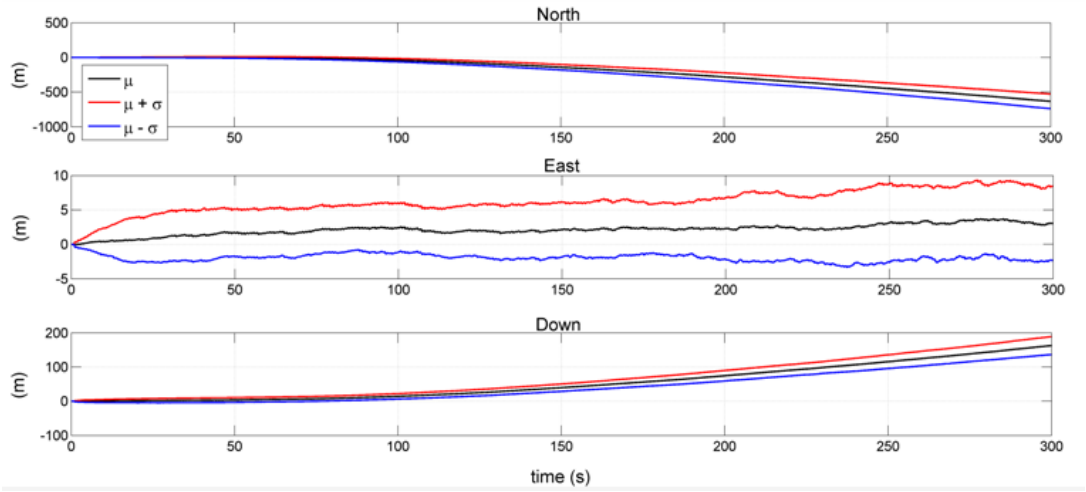

Figure 4.10: Statistics (mean μ and standard deviation σ) of the position error in NED as a function of time (Case 1).

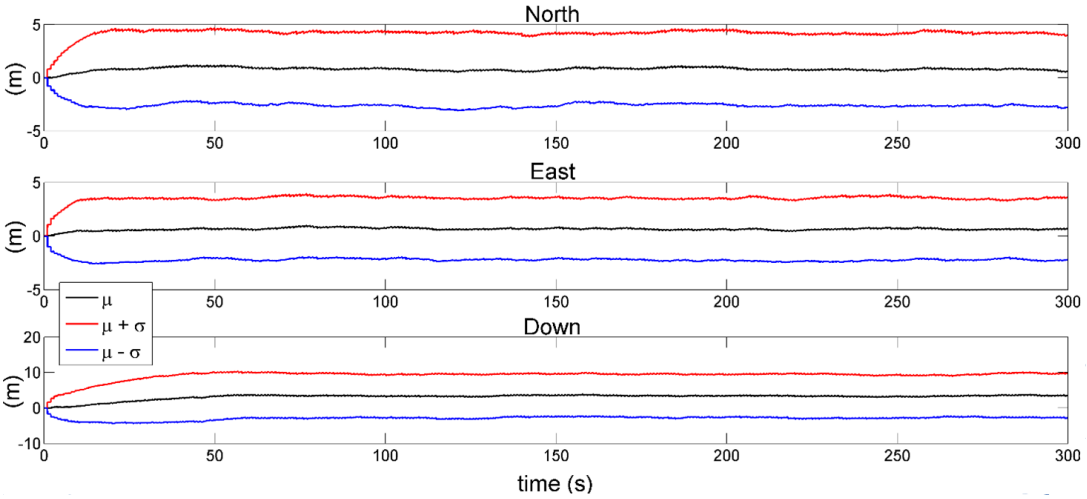

Figure 4.11: Statistics (mean μ and standard deviation σ) of the position error in NED as a function of time (Case 2).

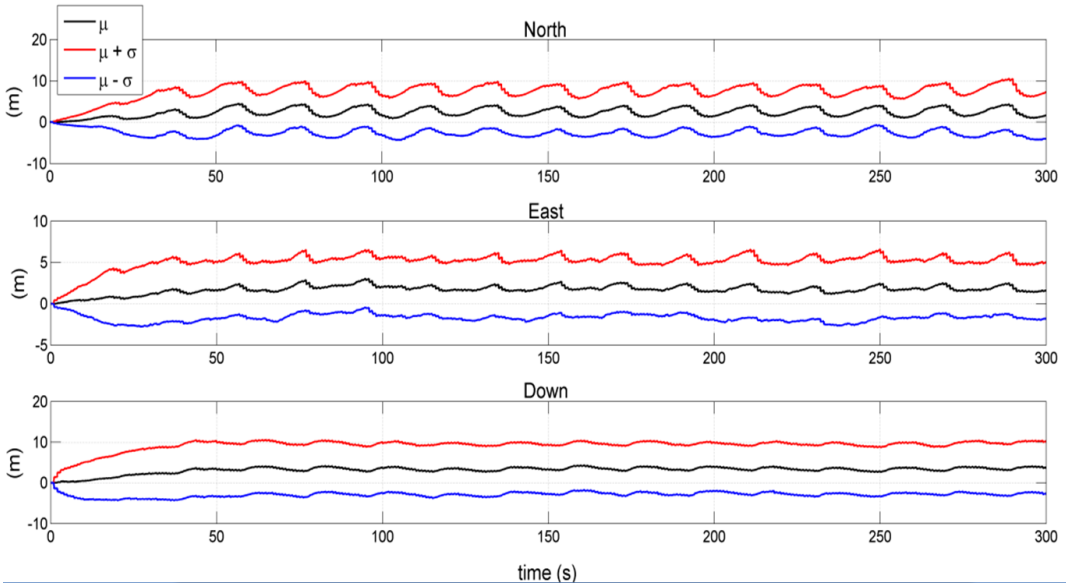

Figure 4.12: Statistics (mean μ and standard deviation σ) of the position error in NED as a function of time (Case 3).

4.5.2 EKF with cooperative aiding and vision-based SLAM (Simulations)

The performance of navigation framework in which cooperative measurements and SLAM are combined (Figure 4.4) has been assessed in terms of the accuracy which characterizes the position components of the estimated pose state. In the analyzed case study, two UAVs fly along a linear path in North direction keeping fixed both the speed (5 m/s) and the altitude with respect to ground. Specifically, the son vehicle flies at an altitude of 20 meters, while the father provides a constant baseline with respect to the son of 20 meters and 80 meters in Up and North directions, respectively. The simulation lasts 5 minutes and the time interval exploited to initialize the map is set to 2 seconds. Finally, the presence of 2000 features is simulated on the ground area covered by the FOV of the nadir-looking camera. These features are uniformly distributed with a density around 0.03 $features/m^2$ in the NED horizontal plane, and between -1

m and 1 m of altitude.

The time variation of the error in the estimation of the son vehicle's position vector in NED is shown in Figure 4.13. The major result is that the position solution provided by the proposed EKF is characterized by a limited error for each of its components, in spite of the absence of a direct aiding from GPS, for 5 minutes during which the son vehicle travelled 1500 meters. Specifically, there is no error accumulation in the estimation of the East component of the position vector during the entire simulation time. Indeed, the error is bounded in a narrow interval around 0, as demonstrated by the values of the temporal mean (0.19 meters) and std (0.82 meters). As regards the North and Down components of the position vector, the estimation error slowly increases as a function of time but the accumulated error at the end of trajectory (EoT) is small (i.e. around 21 m and 22 m in North and Down, respectively) compared to the overall travelled path (around 1%). If the attention is focused on the first 100 seconds of the simulation time, during which the travelled path is 500-meters long, the overall performance of the navigation filter is even better as the error in the estimated vehicle displacement is kept below 6 meters in North, and 3 meters in Down and East.

Analysis of these results has shown a significant correlation between the error in the estimation of the overall position vector and the mapping error obtained in the triangulation process. Of course, this is a direct consequence of exploiting the visual-SLAM concept.

It is now necessary to clarify, how the different aiding factors introduced in the proposed EKF architecture, namely the loosely-coupled pose estimate from the visual SLAM algorithm and the tightly-coupled visual/GPS cooperative measurement from the father vehicle, contribute to obtain the accuracy level presented above. To this end, the time statistics of the position estimation accuracy provided by the developed EKF over the entire simulation time are

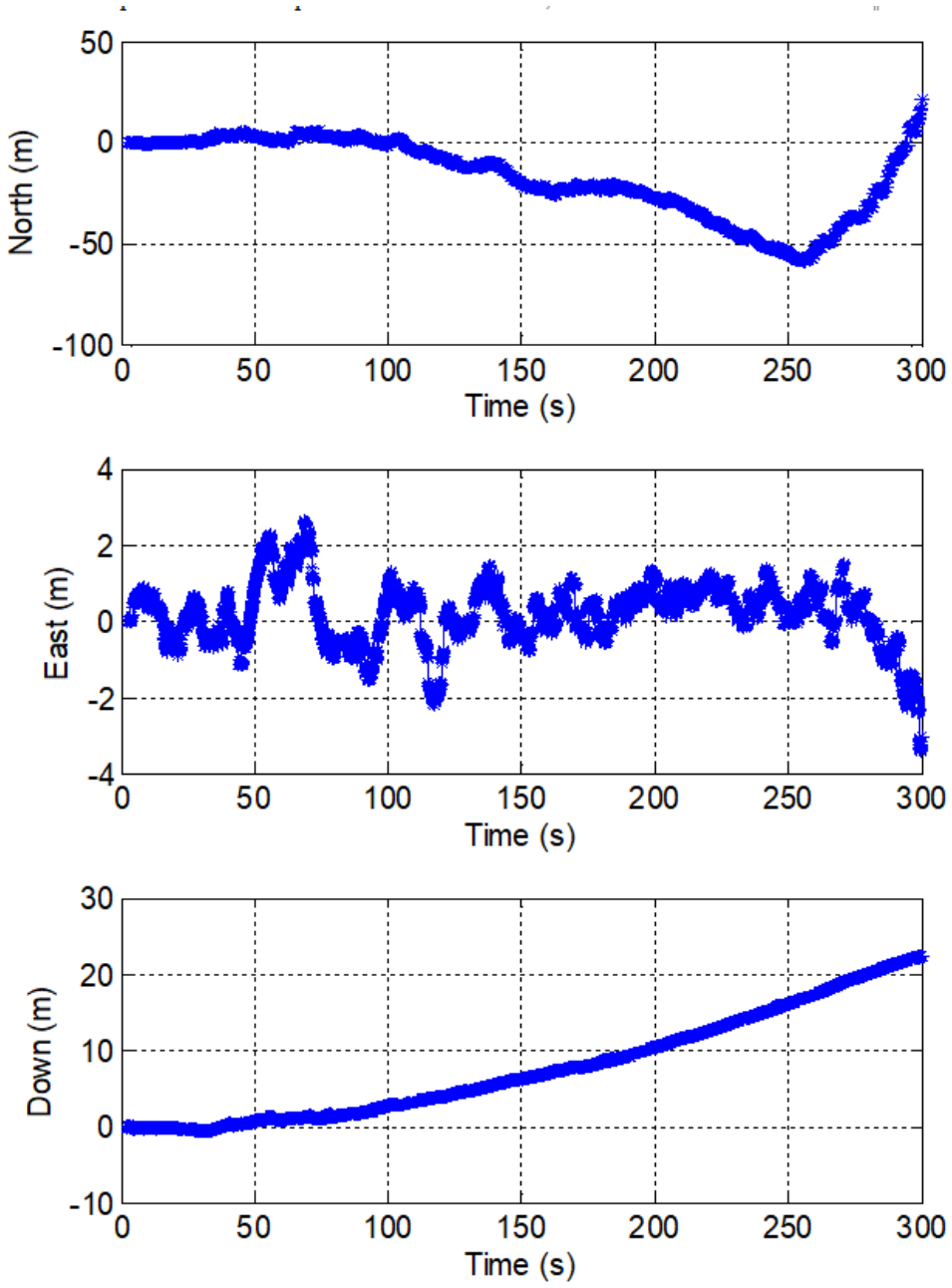

Figure 4.13: Son vehicle position error in NED as a function of time.

shown in Table 4.3, where a comparison is carried out considering the results provided by two additional navigation solutions:

- Standalone visual-SLAM;
- EKF with cooperative aiding.

Starting from the standalone visual-SLAM algorithm, the position estimation error along East and Down directions is characterized by a significant drift as it can be seen by looking at the value of the EoT error, while the corresponding root mean square error (rms), evaluated over the entire trajectory, is about 73 meters and 179 meters, respectively. Conversely, the estimation error in the North position component does not drift and its rms and maximum values are about 13 meters and 22 meters, respectively. This result can be explained since the apparent movement of the features tracked in the images collected by the nadir-looking camera minimizes the mapping error along the North direction and thus makes this movement observable. The situation changes completely when the LOS is integrated in the EKF. In fact, due to the considered formation geometry, the error drift in East direction is eliminated (the EOT error is about 1 m) and the estimation error does not overcome a threshold of approximately 3 m. Unfortunately, the LOS aiding does not allow the navigation filter to avoid the position error drift along the North and Down directions. Consequently, the accumulated position error goes up to a few hundreds of meters. The above mentioned effects are drastically mitigated, both in terms of rms and EoT error, when both LOS and visual-SLAM are integrated within the EKF.

Besides showing the potential of the combined visual SLAM / cooperative approach, these statistics clearly demonstrate how the flight trajectory and the formation geometry impact the navigation performance. This naturally leads to the need of coordinated motion between UAVs.

Table 4.3: Comparison of position estimation errors: Standalone visual-SLAM, EKF + visual-SLAM, EKF + cooperative aiding, EKF + cooperative aiding + visual-SLAM.

Navigation approach	Error in North			Error in East			Error in Down		
	rms (m)	max (m)	EoT (m)	rms (m)	max (m)	EoT (m)	rms (m)	max (m)	EoT (m)
Standalone visual-SLAM	13.50	22.23	13.06	73.19	161.54	161.54	179.59	416.43	416.43
EKF with cooperative aiding	414.22	787.27	787.27	1.19	3.09	1.28	99.43	191.05	191.05
EKF with cooperative and visual-SLAM aiding	25.45	58.39	21.14	0.84	3.40	3.01	10.41	22.39	22.35

4.5.3 EKF with cooperative aiding (Experimental Results)

The preliminary experimental results shown in the following have been obtained using the experimental setup of Test 1 (subsection 3.5.2) where the two ground antennas this time play the role of fathers. That is, the Pelican UAV flying in GPS-challenging environments, is the son, while the two ground antennas with full GPS-coverage, are the surrogate father vehicles.

The analysis has been conducted on a time frame of about 70 seconds during which it is assumed that the Pelican UAV is flying in a GPS-denied environment. Hence, within the filtering architecture, described in Figure 4.3, only LOS and attitude measurements have been integrated.

In the following, the position, in terms of North (Figure 4.14), East (Figure 4.15) and Down (Figure 4.16), estimated by the proposed EKF where 1 LOS (single ground antenna) and 2 LOS (both ground antennas) are integrate, is compared with the position provided by the Pelican GPS receiver. By analyzing these results it is possible to highlight that:

- integrating 1 LOS, or 2 LOS, within the EKF, provides a significant improvement with respect to the pure inertial navigation;
- the position error of the proposed EKF is bounded in the considered time

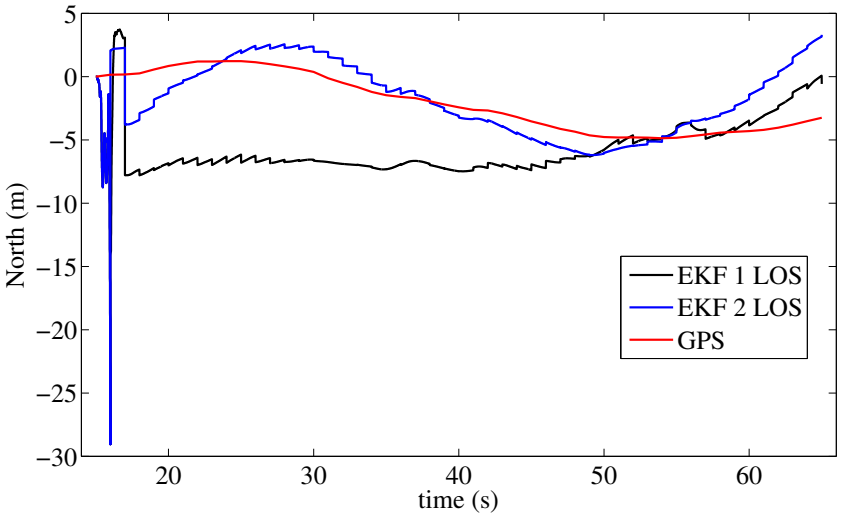

Figure 4.14: Comparison of the North position component estimated by the EKF (with 1 LOS and 2 LOS), with the one provided by the on board GPS receiver.

frame;

- the East component is characterized by an almost constant bias related to: 1) magnetic disturbances (bias on the magnetometer-based heading); 2) residual camera misalignment.

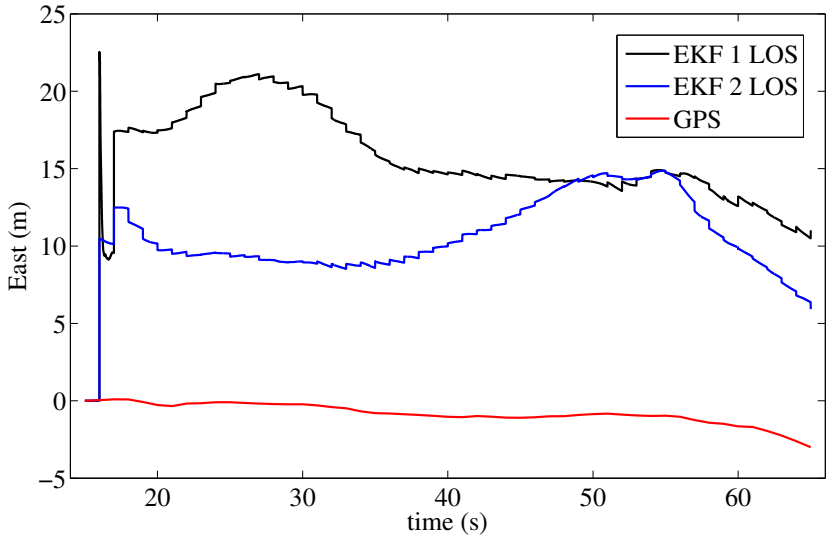

Figure 4.15: Comparison of the East position component estimated by the EKF (with 1 LOS and 2 LOS), with the one provided by the on board GPS receiver.

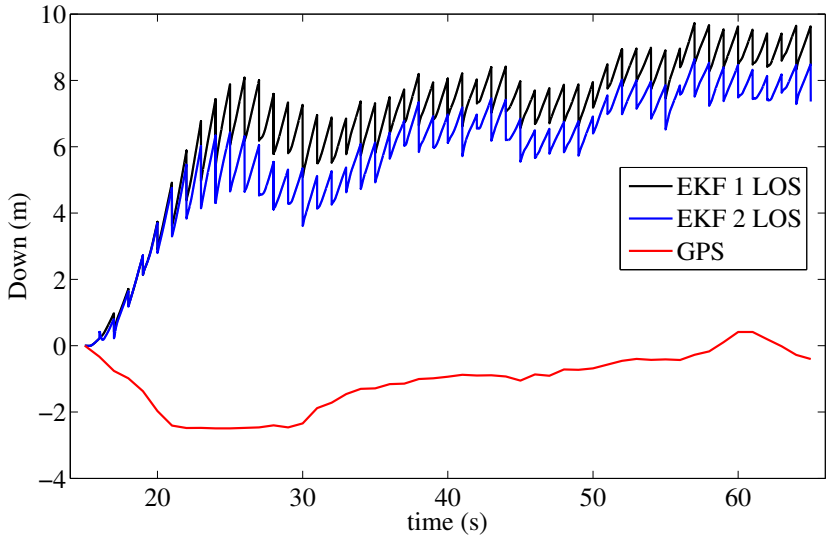

Figure 4.16: Comparison of the Down position component estimated by the EKF (with 1 LOS and 2 LOS), with the one provided by the on board GPS receiver.

Chapter 5

Autonomous UAV Take-off and Landing

In many UAV applications, flexible trajectory generation algorithms and robust navigation and control techniques, are required to enable high levels of autonomy for critical mission phases, such as take-off, area coverage, and landing. Moreover, the need of overcoming the flight time limit, especially in monitoring applications where UAVs take-off from a *nest* and return to it for recharging, requires high levels of system autonomy to guarantee safe and reliable operation.

Often, the final phase (landing) is the most critical as it involves performing delicate maneuvers; e.g., landing on a station for re-charging [95] or on a ground carrier for transportation [8]. These procedures are subject to constraints on time and space, and must be robust to changes in environmental conditions, such as visibility and wind disturbances [96]. To achieve smooth landings, precise sensing and accurate control techniques are therefore required.

In this chapter, these problems are addressed by integrating, within the end-to-end software system developed at the ETH Zürich, a trajectory generation algorithm based on a visual tracking system and a bio-inspired guidance method for autonomously landing on a specified target either indoor or outdoor. This

activity has been conducted during a 6 month of Academic Guest period at ETH Zürich, and the motivation is to increase reliability and versatility of UAVs.

The adopted approach, presented in [97], is based on the improved intrinsic tau guidance theory [98, 99] to generate spatio-temporal (4-D) trajectories for a desired time-to-contact (TTC) based on the estimate of the relative pose of the UAV with respect to the target. This approach enables to perform a maneuver with arbitrary initial and final motion states, and tailor its trajectory profile for various types of rotary- or fixed-wing tasks, such as landing, in-flight obstacle avoidance, and object-picking.

The advantage of this approach is the possibility to generate "*user-oriented*" trajectories, where fundamental parameters can be tuned based on the mission requirements. As such, the user may be interested in assigning predefined mission requirements for the trajectory, such as to maintain the course within the boundary of two intersecting planes (e.g., flying within a natural or man-made canyon), controlling the total mission time or energy consumption, or specifying the initial and final landing angles.

In the following, simulation and experimental (indoor/outdoor) results are presented, considering a rotary-wing UAVs equipped with a downward-looking camera for detecting a static target.

5.1 Related Work

Significant work has been recently done on autonomous landing methods for UAVs in various environments. As discussed in [96], landing navigation frameworks mainly use a GPS and an IMU, with small, light-weight visual sensors often integrated in order to improve the accuracy and to detect the landing platform.

As far as guidance is concerned, several researchers adopted position-based

approaches such as the pursuit [100] and the proportional [101] laws which leverage LOS to navigate the UAV towards the target. While these methods provide precise tracking [8], they may require complex control algorithms and lack controllability of the UAV trajectory pattern and profile, thus restricting their applicability.

Bio-inspired guidance paradigms represent a further solution. In fact, these algorithms are usually based on visual information and use the TTC [102] or optical flow [103] to generate 4-D trajectories [103, 104], enabling the control of both their spatial and temporal components. In this category, the general tau theory [98, 102] has been popularly postulated to describe goal-directed movements, e.g. collision avoidance [99], docking, and landing [104]. Kendoul [104] recently introduced a tau-based UAV autopilot and implemented it to perform high-accuracy maneuvers. Similarly, here the tau principles are used to generate 4-D trajectories for landing. However, by using elements of improved intrinsic tau guidance [99], our method is not restricted to static initial and final states and is thus also suitable for landing on moving platforms.

5.2 Logical Architecture

The logical architecture of the algorithms running on the UAV is described in Figure 5.1, which depicts the different interacting modules. In particular, the input data (Figure 5.1, left) include: GPS measurements, images from the downward-looking camera and the Visual-Inertial (VI-)sensor, and accelerometer and gyroscope measurements from the VI-sensor and the on-board IMU.

As far as the navigation is concerned, the adopted framework consists of two main blocks (ROVIO and MSF). The RObust Visual Inertial Odometry (ROVIO) framework [32] provides the UAV pose, by integrating VI-sensor and GPS data. This is then integrated with UAV IMU data within the MSF frame-

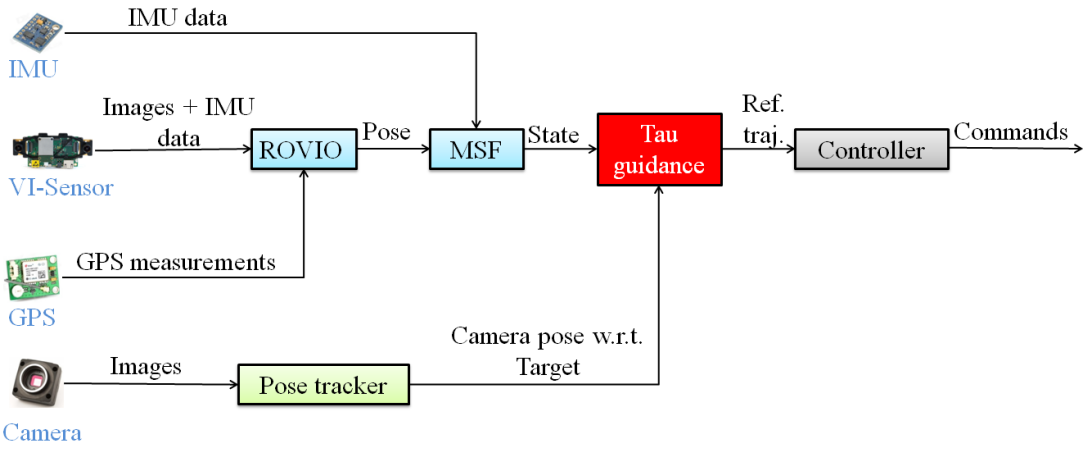

Figure 5.1: Logical architecture for autonomous UAVs landing.

work [105] to obtain a refined state estimate Figure 5.1. It is worth noting that, in the absence of GPS data (e.g. indoor environments), only images and IMU data are input to ROVIO and a pure visual inertial odometry is performed.

Guidance is based on the improved tau guidance strategy (red block in Figure 5.1), which uses the actual UAV state and the camera-to-target relative pose to generate reference trajectories that are then tracked by a non-linear Model Predictive Controller (MPC) [106].

In the following, the focus is set on the improved intrinsic tau guidance strategy.

5.3 Tau guidance

As already mentioned, there are various UAV missions requiring large area coverage. For safe and robust autonomous operation, it is necessary to generate successive and consecutive trajectories by maintaining position and/or velocity continuities on the boundary waypoint between the n^{th} and the $n^{th}+1$ trajectories. Adjourning the trajectories is also required during the successive steps of following or landing on a moving object, taking into account the error deriving

by the tracking algorithm, including noise. Consequently, the main problem is to develop and apply a fast and flexible algorithm enabling the UAV to perform the above-mentioned phases autonomously, while maintaining a small number of intuitive turning parameters.

The general goal-directed trajectory generation problem is defined as follows. A spatio-temporal 4-D UAV trajectory is described by the state:

$$\underline{S}(t) = \{x(t),\, y(t),\, z(t), \dot{x}(t),\, \dot{y}(t),\, \dot{z}(t)\}$$

The aim is to guide the UAV from arbitrary initial states $\underline{S}(t_0)$ to goal states $\underline{S}(t_0 + T)$ in the execution time T.

The trajectory is adjourned based on visual information provided by a camera during the approach phase. The specific requirements for a successful landing are to:

1. reach the target point in a specified time T,
2. arrive and stop at the target point with zero velocity at contact, such that $\underline{S}(t) = \{x(t),\, y(t),\, z(t),\, 0,\, 0,\, 0\}$ at $t = t_0 + T$,
3. reach the target point from a specific approach direction.

5.3.1 Trajectory Parametrization

With reference to Figure 5.2, in the East-North-Up (ENU) frame, the landing maneuver usually requires arriving at a destination with a final state of the trajectory depending on the target morphology and dynamics. The main gaps are

- the distance gap $d(t)$,
- the relative speed,

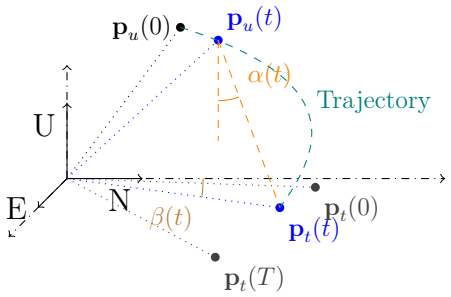

Figure 5.2: Reference frame and main gaps for autonomous tau-landing.

- the approaching angle of the trajectory $\alpha(t)$, between $d(t)$ and the normal to the EN plane,
- the approaching angle of the trajectory $\beta(t)$, which permits changing the UAV heading during perching.

$d(t)$ is the instantaneous distance along the LOS to the target, given by the difference between the UAV position $\underline{p}_u(t)$, and the target position $\underline{p}_t(t)$. The relative speed is given by $\dot{\underline{p}}_u(t) - \dot{\underline{p}}_t(t)$ which, in order to avoid collisions, must be zero at the touch-down. The approaching angle $\alpha(t)$ is based on the landing approach, and consequently depends on the UAV platform and application, e.g., along the tangent to the surface for a fixed-wing UAV, near-vertical for a rotary-wing UAV, or inclined at a certain angle to enter an opening. The approaching angle $\beta(t)$ ensures that the body frames, of the UAV and the target, respect a required orientation at the touch-down, e.g., when recharging requires docking between the two.

5.3.2 Improved Intrinsic Tau Guidance Strategy

The developed landing method uses the improved intrinsic tau guidance strategy [99] to allow for goal-directed movements and, in particular, to start the trajectory with arbitrary initial flight conditions. The intrinsic guidance gap of

a movement $G_v(t)$ can be formulated as:

$$\begin{cases} G_v(t) = -0.5at^2 + V_G t + G_0, \\ \dot{G}_v(t) = -at + V_G, \\ \ddot{G}_v(t) = -a, \end{cases} \tag{5.1}$$

where a is the acceleration, V_G is an initial velocity, and G_0 specifies an initial intrinsic gap. In particular, the intrinsic tau guidance strategy Equation 5.1 represents the vertical component of a projectile motion. Once the acceleration a is assigned, the initial velocity V_G and the initial gap G_0 must be computed according to the initial ($t = 0$) and the final ($t = T$) conditions of the actual movement, as described in the following.

Considering the movement along a generic x-axis from time 0 to T as an example, the position and velocity gaps can be expressed as $\Delta x = x_T - x$ and $\Delta \dot{x} = \dot{x}_T - \dot{x}$, respectively, where x_T and $\dot{x}_T$ denote the goal states at time T. By Applying the tau coupling strategy [104, 99] for synchronous gap-closing it is possible to obtain the reference trajectory

$$\begin{cases} x(t) = x_T + \dot{x}_T(t - T) - \dfrac{\chi_{x0}}{G_0^{1/k_x}} G_v^{1/k_x}, \\ \dot{x}(t) = \dot{x}_T - \dfrac{\chi_{x0}}{k_x G_0^{1/k_x}} \dot{G}_v G_v^{1/k_x - 1}, \\ \ddot{x}(t) = -\dfrac{\chi_{x0}}{k_x G_0^{1/k_x}} G_v^{1/k_x - 2} \left(\dfrac{1 - k_x}{k_x} \dot{G}_v^2 + G_v \ddot{G}_v \right). \end{cases} \tag{5.2}$$

where k_x is a gain parameter controlling gap convergence along the x-axis, as discussed below.

From the definition of G_v, Equation 5.2, and Equation 5.1, it can be shown that:

$$\begin{cases} G_0 = \dfrac{\chi_{x0} g T^2}{2(\chi_{x0} + k_x \Delta \dot{x}_0 T)}, \\ V_G = \dfrac{k_x \Delta \dot{x}_0 g T^2}{2\left(\chi_{x0} + k_x \Delta \dot{x}_0 T\right)}. \end{cases} \tag{5.3}$$

G_0 and V_G can be viewed as bonding actual and intrinsic movements due to gravitational effects. If $k_x \in (0,\, 0.5)$, $(x,\, \dot{x},\, \ddot{x}) \rightarrow (x_T,\, \dot{x}_T,\, 0)$ and the position and velocity can be steadily guided to the target values, as required. Hence, varying the elements of $\underline{k} = \{k_x,\, k_y,\, k_z\}$ within this range allows for modifying the trajectory profile along each axis.

In addition, using the tau coupling strategy it is possible to apply a more "$user - oriented$" approach by coupling to the intrinsic movements the gaps $d(t)$, $\alpha(t)$ and $\beta(t)$ as follows:

$$d(t) = \frac{d(0)}{G_0^{\frac{1}{k_d}}} G_v^{\frac{1}{k_d}} \tag{5.4}$$

$$\alpha(t) = \frac{\alpha(0)}{d(0)^{\frac{1}{k_\alpha}}} d(t)^{\frac{1}{k_\alpha}} \tag{5.5}$$

$$\beta(t) = \frac{\beta(0)}{d(0)^{\frac{1}{k_\beta}}} d(t)^{\frac{1}{k_\beta}} \tag{5.6}$$

Where each gap has its own gain parameter (k_d,k_α,k_β). Combining these equations the position vector at time t of the UAV is simply given by:

$$\underline{p}(t) = \underline{p}(T) + \begin{bmatrix} -d(t) sin\alpha(t) cos\beta(t) \\ -d(t) sin\alpha(t) sin\beta(t) \\ d(t) cos\alpha(t) \end{bmatrix} \tag{5.7}$$

5.4 Simulations

The performance of the proposed landing method is validated preliminarily in simulation. The simulation environment is developed in the RotorS framework [107], which realistically replicates the flight dynamics of an Asctec Firefly and

its on-board sensors. For the IMU, the orders of magnitude of biases and random errors are set to be consistent with MEMS used on the AscTec Firefly (Table 5.1). Furthermore, the GPS position uncertainty in the ENU frame is modeled as a constant bias plus Gaussian white noise to account for the time correlation in GPS errors. For vision sensing, only the downward-looking camera was simulated with an IFOV uncertainty modeled as Gaussian white noise with a standard deviation of 0.05°. This camera is used to detect the landing target on the ground and to obtain its relative pose with respect to the UAV. Consequently, navigation is achieved here without simulating ROVIO, but only integrating simulated position and attitude measurements within the MSF framework.

Table 5.1: Assumptions on the simulated bias and random errors for our simulation trials.

Sensors	Bias instability	Random walk
Gyroscopes	14.5°/hr	$0.66°/\sqrt{hr}$
Accelerometers	0.25 mg	$0.11\ \mathrm{m/sec}/\sqrt{hr}$

The simulations serve to validate and integrate each component of the software framework before the experimental tests. Since the focus is set on rotary-wing UAVs, the interest is also to land on the platform with a desired orientation $\alpha(t)$ and zero velocity. Hence, simulations have been performed to evaluate the behavior of trajectory shapes for varying coefficients $\underline{k}$ with an emphasis on vertical landing. Figure 5.3 (a) shows a comparison of different landing trajectories where the maneuver starts from an height of 1.5 m and EN components of 0.8 m each. This figure evidences how the 3-D shape of each trajectory is determined by coupling the coefficients $\underline{k}$. In particular, the smaller is the adopted k value, the faster is the closing of the relative gap. In addition, Figure 5.3 (b) shows

the velocity and acceleration profiles during the near-vertical landing trajectory (blue curve in Figure 5.3 (a)), demonstrating that zero velocity is reached at the end of the landing maneuver.

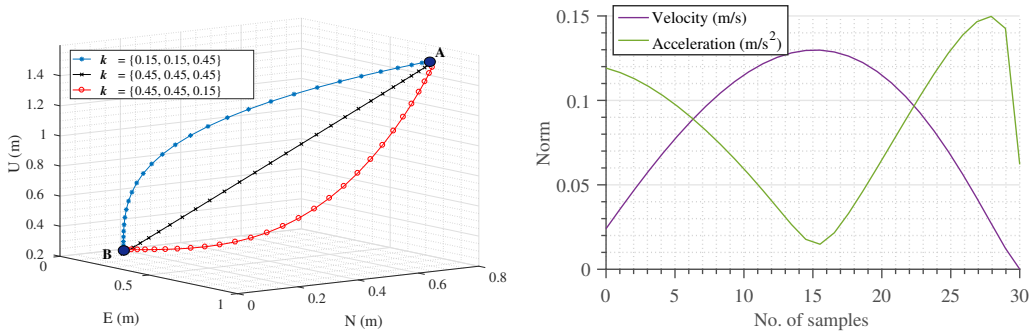

(a) **(b)**

Figure 5.3: (a) depicts landing trajectories with different elements in $\underline{k}$. These parameters enable modifying the trajectory profile for LOS (black), near-vertical (blue), and near-horizontal (red) shapes. (b) shows the velocity and acceleration norm profiles for the near-vertical (blue) curve in (a).

5.5 Experimental Setup

This section details physical system architectures used to test the proposed method. To demonstrate applicability, experiments in both outdoor and indoor environments have been conducted.

The outdoor experiments are conducted on an empty $20 \times 20\,\mathrm{m}$ farmland plot in clear weather conditions (Figure 5.4), where the algorithms are run in real-time on an AscTec Firefly (Figure 5.5). The UAV is equipped with an autopilot providing a low- and high-level control, and on-board computer (AscTec Mastermind), and the following sensors:

- 100 Hz IMU,

Figure 5.4: Experimental set-up on the field, with the GPS RTK base station visible on the right.

- 10 Hz Piksi V2 RTK differential GPS,
- 20 Hz VI-sensor,
- 50 Hz downward-looking Point Grey Chameleon 2.0 camera.

The landing platform target (Figure 5.6) is an A3 (297×420 mm) arrangement of variable-dimension tags, obtained from the `ar_track_alvar` library. The nested tag layout on the platform allows for detecting and estimating the camera-to-target relative pose from different altitudes. Note that, in this chapter, static platform is considered for proof of concept and leave the study of moving targets to future work.

Indoor experiments were also performed in an empty 20×20 m environment (Figure 5.7) using the same landing platform. Here, algorithms run in real-time on a DJI Matrice 100 with a 100 Hz IMU and Intel RealSense ZR300 camera providing 30 Hz images. The system comprises the general pipeline in Figure 5.1;

Figure 5.5: AscTec Firefly positioned on the landing platform.

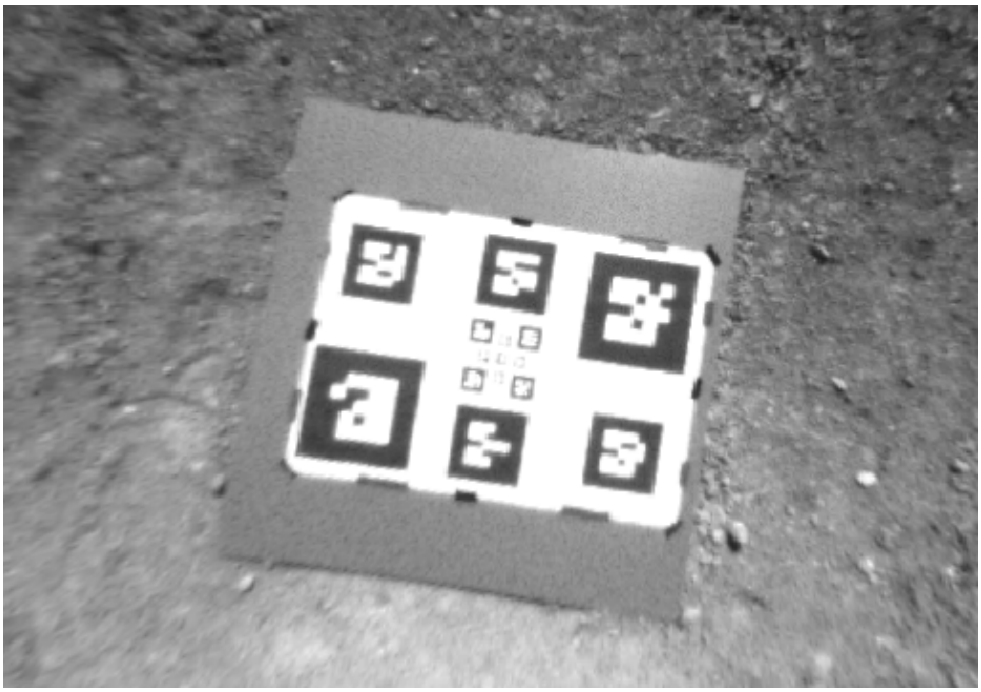

Figure 5.6: AscTec Firefly positioned on the landing platform.

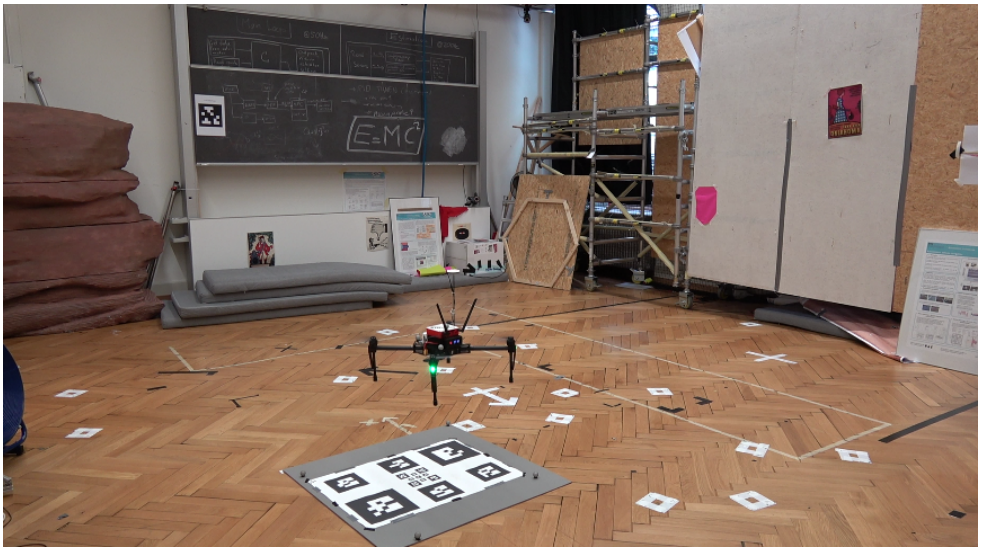

Figure 5.7: A side view of our indoor experimental set-up showing the UAV and the landing platform.

however, in the absence of GPS data, only images and IMU data are input to ROVIO and MSF.

5.6 Experimental Results

Multiple experiments have been conducted to test the developed approach using the set-ups described in section 5.5. In each trial, the UAV was commanded to:

1. take-off and perform its mission,
2. fly back to the landing area,
3. fly a search path to detect the target, and
4. safely land on the target point in a specified time.

Figure 5.8 and Figure 5.9 illustrate the two autonomous landing stages for an outdoor test using an AscTec Firefly. The first stage is target detection (at an

height of about 2 m, as shown in Figure 5.8 (c)) followed by a refinement phase for noise reduction. Once the target is detected and tracked, the UAV starts the approaching stage during which the camera continues tracking the target to update its relative pose. If the difference between successive target positions is larger than a certain tolerance, the trajectory is re-planned accordingly and passed to the non-linear MPC.

These aspects are evident in Figure 5.8, which shows the UAV position components in the ENU frame. A comparison of the reference trajectory generated by our guidance strategy with the UAV position output from the MSF framework confirms that the controller follows the reference throughout the maneuver until the touch-down.

Figure 5.9 compares the UAV position and velocity along the three coordinate axes. The plots illustrate the optimum velocity profile of the maneuver to reach the softest touch-down while achieving the accuracy required to land near the target center.

As shown in Figure 5.10, the final landing position remains within a maximum dispersion of several centimeters with respect to the target center. It is worth noting that, if the target is lost for a certain time period, the UAV is commanded to climb to increase the camera footprint, and returns on the landing path only after the target is detected and tracked again. Figure 5.10 demonstrates this effect as the target is lost at ~ 20 cm height mainly due to the UAV shadow causing occlusions impeding robust tracking. As a result, the UAV ascends, landing smoothly upon target re-detection.

In addition, 63 successful indoor landings were executed with the DJI Matrice 100. State estimation was obtained by integrating ROVIO within the MSF framework, the relative pose between the UAV and the landing platform was obtained by images acquired by the Intel RealSense ZR300 and the VICON system was used for ground truth reference. These tests show the repeatabil-

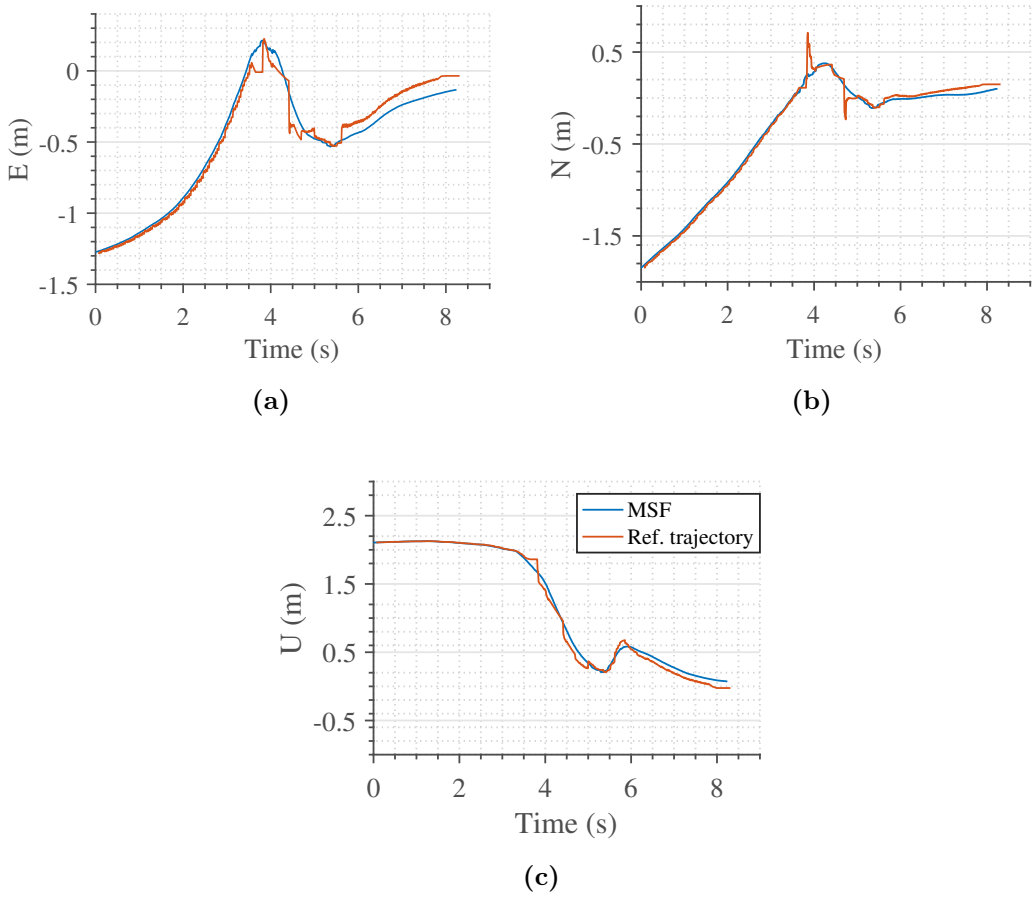

Figure 5.8: Differences between the reference and MSF trajectories during the final phases of landing.

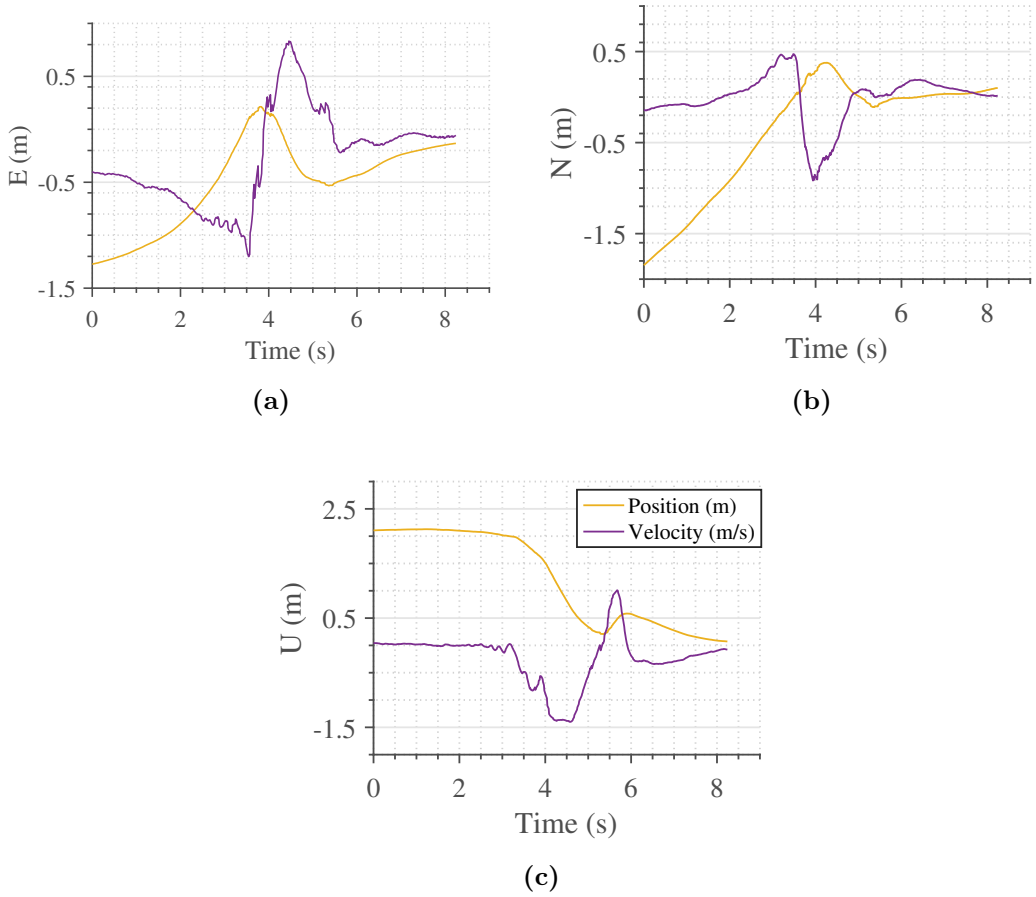

Figure 5.9: Velocity profile during the landing maneuver with the position profile as a reference.

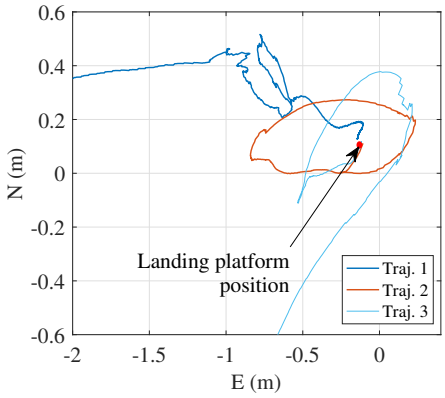

Figure 5.10: UAV landing position with respect to the target position in the EN plane.

Height (m)	1.5		2.0		2.5	
	$k_z = 0.2$	$k_z = 0.4$	$k_z = 0.2$	$k_z = 0.4$	$k_z = 0.2$	$k_z = 0.4$
Mean (m)	0.15	0.16	0.14	0.14	0.2	0.19
Std (m)	0.02	0.04	0.04	0.05	0.04	0.04

Table 5.2: Landing mean errors and standard deviations for the case studies considered.

ity and robustness of the proposed landing approach as well as its achievable accuracy. To this end, six case studies were considered varying in the **k** coefficients and the height of the target detection stage . The approaching heights tested were 1.5 m, 2 m, and 2.5 m meters, with two different sets of **k** coefficients: $k_x = k_y = 0.2, k_z = 0.4$, and $k_x = k_y = k_z = 0.2$. Statistical results are summarized in Table 5.2. Here, errors are computed based on UAV and target ground truth positions acquired from the VICON system.

Chapter 6

Conclusions

This thesis presented new methodologies to overcome single micro-UAV limits (e.g. performance, coverage and reliability), where the concept is to exploit two or more UAVs flying cooperatively, and to develop an autonomous take-off and landing technique, in order to improve navigation performance and flight autonomy. In fact, formations of UAVs, besides being adopted for real time coverage of large areas and for increasing the capability to prevent and control natural disasters, can be exploited to improve the navigation performance, of vehicles within the formation, by adopting two main concepts, that is, information sharing and relative sensing.

Among several research challenges to be addressed in order to design and operate a distributed system of vehicles working together for real time applications, this thesis in particular has achieved the following results:

Improvement of UAV navigation performance In this research activity, algorithms for cooperative UAV navigation in outdoor environments were presented. These algorithms are based on the concepts of differential GNSS, relative sensing provided by machine vision (DGPS/Vision), and sensor fusion with the onboard navigation sensors. The logical architecture and the main processing steps were presented, focusing on the vision-based

tracking algorithm, the two adopted differential GPS solutions (CGDPS and code-based DGPS) and the sensor fusion algorithm based on a customized EKF. Both numerical simulations and flight results showed the potential of sub-degree angular accuracy. In particular, proper formation geometries, and even relatively small baselines, allow achieving a heading uncertainty that can approach 0.1°, which represents a very important result taking into account typical performance levels of IMUs onboard small UAVs. Furthermore, the dependency of attitude estimation performance on formation geometry can be exploited to the navigation advantage if proper cooperative guidance laws are used to reconfigure the UAV formation as needed. Flight experiments showed that the main factor enabling highly accurate attitude estimates is the information independence from both inertial and magnetic measurements. On the one hand, DGPS/Vision estimates are not influenced by flight history and changing inertial sensors biases, thus being insensitive to error accumulation phenomena. On the other hand, they are not affected by magnetic phenomena which are difficult to counteract in single vehicle applications since resulting errors depend on vehicle orientation.

UAV navigation in GPS challenging environments This research topic aimed at developing algorithms, for improving navigation performance of UAVs flying in GPS-challenging environments (e.g. natural or urban canyons, or mixed outdoor-indoor settings), based on the concept of including within the navigation filter the line-of-sight with respect to a cooperative vehicle flying under nominal GPS coverage. After an overview of cooperative and vision-aided approaches, logical architecture and the mathematical structure of the algorithms were discussed. The core of the algorithms is an Extended Kalman Filter (EKF) which integrates measurements coming from on-board inertial sensors with measurements coming

from a cooperative vehicle flying under nominal GPS coverage, that is the visual Line-Of-Sight (LOS) and its GPS position. In addition, the integration with monocular pose estimation algorithms was investigated showing the possibility to counteract the position error drift. The performance of the proposed approach was evaluated through numerical simulations in which low cost MEMS inertial sensors and typical uncertainty values for both cooperative and vision-based navigation techniques were assumed. Moreover, preliminary experimental results have been achieved by adopting a customized quadrotor and two ground GPS antennas. Results showed that aiding measurements from standalone visual-SLAM or a single cooperative UAV do not allow eliminating position error drift. However, combining both approaches drastically reduces the position error drift keeping meter-level positioning accuracy also in absence of reliable GPS observables. Moreover, the error drift can be reduced either integrating valid pseudorange measurements in the tightly coupled filtering structure, or exploiting ad hoc commanded motion of the cooperative vehicle under GPS coverage. In both these cases, meter-level positioning accuracy is preserved in spite of absent or limited GPS coverage, resulting in the unavailability of position fix. These results show that cooperative navigation has a significant potential for safe flight in GPS-challenging environments, also in absence of inter-vehicle range measurements.

Autonomous take-off and landing This research activity, conducted during a 6 month Academic Guest period at ETH Zürich, focused on increasing reliability, versatility and flight time of UAVs, by developing an autonomous cooperative take-off and landing technique.

In particular, a guidance approach, based on the improved intrinsic Tau guidance law for autonomous UAV landing on a static platform was presented. The guidance theory generates smooth and computationally ef-

ficient 4-D trajectories that are both suitable for fixed- and rotary-wing UAV platforms. The framework was validated in simulations and multiple outdoor and indoor experiments with different platforms, showing that trajectories can be easily designed by varying the guidance coefficients. Results from over 60 indoor tests, using a VICON system only to provide ground truth reference, demonstrate landing with centimeter-level accuracy.

Appendices

Appendix A

System dynamic matrix

Navigation error arises due to initial condition error and the accumulation of instrumentation errors through the integration process. This section, focuses on model development for the geographic frame (NED) mechanization approach [9]. In particular, this appendix introduces the 9×9 continuous-time system dynamic matrix $\underline{\underline{F}}$ of the linear dynamic model for the

$$\delta\dot{\underline{x}} = \underline{\underline{F}}\delta\underline{x} + \underline{\underline{\Gamma}}\,\underline{q} \tag{IA.1}$$

where $\delta\dot{\underline{x}}$ is the state error vector defined in Equation 3.15, and $\underline{\underline{\Gamma}}$ and $\underline{q}$ are

$$\underline{\underline{\Gamma}} = \begin{bmatrix} \underline{\underline{0}} & \underline{\underline{0}} \\ -\underline{\underline{R}}_b^n & \underline{\underline{0}} \\ \underline{\underline{0}} & -\underline{\underline{R}}_b^n \end{bmatrix}; \underline{q} = \left[(\delta\underline{f}^b)^T, (\delta\underline{\omega}_{ib}^b)^T\right]^T \tag{IA.2}$$

To clearly present the matrix entries, it is important to define the following terms

- ω_{ie} = earth rotational rate
- R_e = earth radius
- ϕ = latitude

Table A.1: Dynamic matrix entries

$\Omega_N = \omega_{ie}\cos\phi$	$\omega_E = \rho_E$	$F_{53} = -\rho_E\rho_D - k_D\rho_N$
$\Omega_D = -\omega_{ie}\sin\phi$	$\omega_D = \Omega_D + \rho_D$	$F_{54} = -(\omega_D + \Omega_D)$
$\rho_N = \frac{v_e}{R_e}$	$k_D = \frac{v_d}{R_e}$	$F_{55} = k_D - \rho_E\tan\phi$
$\rho_E = -\frac{v_n}{R_e}$	$F_{41} = -2\Omega_N v_e - \frac{\rho_N v_e}{\cos\phi^2}$	$F_{56} = \omega_N + \Omega_N$
$\rho_D = -\frac{v_e\tan\phi}{R_e}$	$F_{43} = \rho_E k_D - \rho_N\rho_D$	$F_{63} = \rho_N^2 + \rho_E^2 - 2\frac{g}{R_e}$
$\omega_N = \Omega_N + \rho_N$	$F_{51} = 2(\Omega_N v_n + \Omega_D v_d) + \frac{\rho_N v_n}{\cos\phi^2}$	$F_{91} = \Omega_N + \frac{\rho_N}{\cos\phi^2}$

- $f_n; f_e; f_d$ = specific force components in NED

- $v_n; v_e; v_d$ = velocity components in NED

Consequently (see also Table A.1), the 9x9 system dynamic matrix is given by

$$\underline{\underline{F}} = \begin{bmatrix} 0 & 0 & \frac{\rho_E}{R_e} & \frac{1}{R_e} & 0 & 0 & 0 & 0 & 0 \\ -\frac{\rho_D}{\cos\phi} & 0 & -\frac{\rho_N}{R_e\cos\phi} & 0 & \frac{1}{R_e\cos\phi} & 0 & 0 & 0 & 0 \\ 0 & 0 & 0 & 0 & 0 & -1 & 0 & 0 & 0 \\ F_{41} & 0 & F_{43} & k_D & 2\omega_D & -\rho_E & 0 & f_d & -f_e \\ F_{51} & 0 & F_{53} & F_{54} & F_{55} & F_{56} & -f_d & 0 & f_n \\ -2v_e\Omega_D & 0 & F_{63} & 2\rho_E & -2\omega_N & 0 & f_e & -f_n & 0 \\ -\Omega_D & 0 & \frac{\rho_N}{R_e} & 0 & -\frac{1}{R_e} & 0 & 0 & \omega_D & -\omega_E \\ 0 & 0 & \frac{\rho_E}{R_e} & \frac{1}{R_e} & 0 & 0 & -\omega_D & 0 & \omega_N \\ F_{91} & 0 & \frac{\rho_D}{R_e} & 0 & \frac{\tan\phi}{R_e} & 0 & \omega_E & -\omega_N & 0 \end{bmatrix} \quad \text{(IA.3)}$$

Acknowledgments

During my PhD activity, I had the opportunity of working and collaborating with many great researchers. Most of them have contributed to my professional growth, and I would like to thank them all for their help.

First and foremost, I would like to thank my supervisors, Professors Domenico Accardo and Giancarmine Fasano, their guidance and support has been fundamental to define the research path and to broaden my knowledge. Professor Alfredo Renga also contributed to my professional growth and deserves my special thanks. Moreover, I would like to thank my colleagues and friends, Antonio, Roberto and Vittorio with whom I shared a wide part of my joys, expectations and hopes. More in general, I would like to thank the whole Aerospace Systems Team for the great moments shared during this journey.

During my PhD a six month research period was also spent at ETH, in Zurich, with the Autonomous Systems Lab (ASL). I immediately felt part of the group and I really enjoyed the team spirit and the possibility of sharing opinions, jokes, ideas. Hence, my special thanks to Professor Roland Siegwart and Juan Nieto for having given me the possibility of joining this great team. Moreover, thanks to the whole MAV team, in particular Inkyu, Masha and Raghav for their help and efforts in conducting the experimental campaigns.

A heartfelt thanks goes out to Marcella who has been there every step of the way with patience and love. Finally, my biggest thank goes to my family for all their love and encouragement, I can't see getting where I am without them.

Bibliography

[1] K. Valavanis and G.J. Vachtsevanos. *Handbook of Unmanned Aerial Vehicles*. Springer, Dordrecht, The Netherlands, 2015.

[2] M. Brooks. Welcome to the personal drone revolution. *New Scientist*, 216(2894):42–45, 2012.

[3] Federal Aviation Administration. FAA Aerospace Forecast Fiscal Years 2010-2030, 2010.

[4] Federal Aviation Administration. Testimony Statement of Earl Lawrence, 2017.

[5] K. Dalamagkidis. *Classification of UAVs in Handbook of Unmanned Aircraft Systems*. Springer, Dordrecht, Netherlands, 2015.

[6] R. Austin. *Unmanned Aircraft System: UAVS Design, Development and Deployment*. John Wiley & Sons, Ltd, Chichester, UK, 2010.

[7] B Clough. Metrics, schmetrics! How do you track a UAV's autonomy? In *Proceedings of the AIAA 1st Technical Conference and Workshop on Unmanned Aerospace Vehicles*, Portsmouth, 2002.

[8] Farid Kendoul. Survey of advances in guidance, navigation, and control of unmanned rotorcraft systems. *Journal of Field Robotics*, 29(2):315–378, 2012.

[9] Jay Farrell. *Aided Navigation: GPS with High Rate Sensors*. McGraw-Hill, Inc., New York, 1 edition, 2008.

[10] C. De Wagter, S. Tijmons, B.D.W. Remes, and G.C.H.E. de Croon. Autonomous flight of a 20-gram Flapping Wing MAV with a 4-gram onboard stereo vision system. In *2014 IEEE International Conference on Robotics and Automation (ICRA)*, pages C. De Wagter, S. Tijmons, B.D.W. Remes, and G.C.H., 2014.

[11] Amedeo Rodi Vetrella, Giancarmine Fasano, and Domenico Accardo. Differential GNSS and Vision-Based Tracking to Improve Navigation Performance in Cooperative Multi-UAV Systems. *Sensors*, 16(no. 12):Article number 2164, 2016.

[12] Amedeo Rodi Vetrella, Giancarmine Fasano, and Domenico Accardo. Satellite and Vision-aided Sensor Fusion for Cooperative Navigation of Unmanned Aircraft Swarms. *Journal of Aerospace Information Systems (JAIS)*, 14(6):327–344, 2017.

[13] Giancarmine Fasano, Domenico Accardo, Antonio Moccia, and David Maroney. Sense and avoid for unmanned aircraft systems. *Aerospace and Electronic Systems Magazine*, 31(11):82–110, 2016.

[14] Giancarmine Fasano, Domenico Accardo, Anna Elena Tirri, Antonio Moccia, and Ettore De Lellis. Radar/electro-optical data fusion for non-cooperative UAS sense and avoid. *Aerospace Science and Technology*, 46:436–450, 2015.

[15] Luis Mejias, John Lai, Jason J. Ford, and Peter O'Shea. Demonstration of closed-loop airborne sense-and-avoid using machine vision. *Aerospace and Electronic Systems Magazine*, 27(4):4–7, 2012.

[16] C.; Eling, M.; Wieland, C.; Hess, L.; Klingbeil, and H. Kuhlmann. Development and Evaluation of UAV based Mapping Systems for Remote Sensing and Surveying Applications. *International Archives of the Photogrammetry, Remote Sensing and Spatial Information Sciences*, Volume XL-, 2015.

[17] Y. Lin, J. Hyyppa, and A. Jaakkola. Mini-UAV-Borne LIDAR for Fine-Scale Mapping. *IEEE Geoscience and Remote Sensing Letters*, 8(3):426–430, 2011.

[18] M. Rehak and J. Skaloud. Applicability of new approaches of sensor orientation to micro aerial vehicles. In *XXIII ISPRS Congr.*, pages 441–447, Prague, Czech Repub., 2016.

[19] U-blox. NEO-M8P series.

[20] Piksi Multi GNSS Module.

[21] Amedeo Rodi Vetrella, Giancarmine Fasano, Alfredo Renga, and Domenico Accardo. Cooperative UAV Navigation Based on Distributed Multi-Antenna GNSS, Vision, and MEMS Sensors. In *IEEE International Conference on Unmanned Aircraft Systems*, Denver, CO, USA, 2015. IEEE.

[22] Amedeo R Vetrella, Giancarmine Fasano, and Domenico Accardo. Accurate attitude estimation for cooperating UAVs based on tight integration of GNSS and vision-based measurements. *Submitted to IEEE Transactions on Aerospace and Electronics Systems*.

[23] Amedeo Rodi Vetrella, Flavia Causa, Alfredo Renga, Giancarmine Fasano, Domenico Accardo, and Michele Grassi. Flight Demonstration of Multi-UAV CDGPS and Vision-Based Sensing for High Accuracy Attitude Esti-

mation. In *IEEE International Conference on Unmanned Aircraft Systems*, Miami, FL, USA, 2017. IEEE.

[24] Amedeo Rodi Vetrella, Flavia Causa, Alfredo Renga, Giancarmine Fasano, Domenico Accardo, and Michele Grassi. Multi-UAV Carrier Phase Differential GPS and Vision-based Sensing for High Accuracy Attitude Estimation. *Submitted toJournal of Intelligent & Robotic Systems for publication.*

[25] H.G. De Marina, F.J., Pereda, and J.M. Giron-Sierra. UAV attitude estimation using unscented kalman filter and TRIAD. *IEEE Trans. Ind. Electron.*, Volume 59(Issue 11):pp. 4465–4474, 2012.

[26] Roberto G Valenti, Ivan Dryanovski, and Jizhong Xiao. Keeping a good attitude: A quaternion-based orientation filter for IMUs and MARGs. *Sensors*, 15(8):pp. 19302—-19330, 2015.

[27] SBG. Ellipse.

[28] Sensonor. Stim300.

[29] G. Giorgi, P.J.G. Teunissen, S. Verhagen, and P.J. Buist. Testing a new multivariate GNSS carrier phase attitude determination method for remote sensing platforms. *Advances in Space Research*, 46(2):118–129, 2010.

[30] D. Scaramuzza and F. Fraundorfer. Visual Odometry [Tutorial]. *IEEE Robotics & Automation Magazine*, 18(4):80–92, 2011.

[31] C. Forster, L. Carlone, F. Dellaert, and D. Scaramuzza. On-Manifold Preintegration for Real-Time Visual–Inertial Odometry. *IEEE Transactions on Robotics*, 33(1):1–21, 2017.

[32] Michael Bloesch, Sammy Omari, Marco Hutter, and Roland Siegwart. Robust Visual Inertial Odometry Using a Direct EKF Based Approach.

In *IEEE/RSJ Intenational Conference on Intelligent Robots and Systems*, pages 298–304, Hamburg, 2015. IEEE.

[33] N. Michael, D. Mellinger, Q. Lindsey, and V. Kumar. The GRASP multiple micro UAV testbed. *IEEE Robotics and Automation Magazine*, 17(3), 2010.

[34] M. Saska, J. Chudoba, L. Precil, J. Thomas, G. Loianno, A. Tresnak, V. Vonasek, and V. Kumar. Autonomous deployment of swarms of micro-aerial vehicles in cooperative surveillance. In *IEEE International Conference on Unmanned Aircraft Systems 2014 (ICUAS 2014)*, Orlando, 2014.

[35] A. Tsourdos, B. White, and M. Shanmugavel. *Cooperative Path Planning of Unmanned Aerial Vehicles*. Wiley, 2010.

[36] I.V.Melnyk, J.A.Hesch, and S.I.Roumeliotis. Cooperative Vision-aided Inertial Navigation Using Overlapping Views. In *IEEE Int. Conf. on Robotics Automation*, Saint Paul, Minnesota, USA, 2012.

[37] H. Mokhtarzadeh and D. Gebre-Egziabher. Performance of networked dead reckoning navigation system. *IEEE Transactions on Aerospace and Electronic Systems,*, 52(5):2539–2553, 2016.

[38] S. Lynen, M.W. Achtelik, S. Weiss, M. Chli, and R. Siegwart. A Robust and Modular Multi-Sensor Fusion Approach Applied to MAV Navigation. In *IEEE/RSJ Int. Conference on Intelligent Robots and Systems (IROS)*, 2015.

[39] H.D. Black. A passive system for determining the attitude of a satellite. *AIAA J.*, 2:1350–1351, 1964.

[40] J.R. Wertz. Spacecraft Attitude Determination and Control. *D. Reidel Publishing Company*, 1978.

[41] W. Yuanwei, S. Yao, and W. Guanghui. Vision-based Real-Time Aerial Object Localization and Tracking for UAV Sensing System, 2017.

[42] A. Nussberger, H. Grabner, and L. Van Gool. Feature article: Robust Aerial Object Tracking from an Airborne platform. *IEEE Aerospace and Electronic Systems Magazine*, 31(7):38–46, 2016.

[43] G. Fasano, D. Accardo, and A.E. et al. Tirri. Sky Region Obstacle Detection and Tracking for Vision-Based UAS Sense and Avoid. *J. Intell Robot Syst*, 2016.

[44] D. Comaniciu, V. Ramesh, and P. Meer. Real-time tracking of non-rigid objects using mean shift. In *IEEE Conference on Computer Vision and Pattern Recognition (CVPR)*, pages 142–149. IEEE, 2000.

[45] R. T. Collins and Y. Liu. On-Line Selection of Discriminative Tracking Features. In *IEEE Conf. on Computer Vision (ICCV),*, pages 346–352. IEEE, 2003.

[46] C. Tomasi and T. Kanade. Detection and Tracking of Point Features. *Tech. rep., International Journal of Computer Vision*, 1991.

[47] Roberto Opromolla, Amedeo R Vetrella, Giancarmine Fasano, and Domenico Accardo. Airborne Visual Tracking for Cooperative UAV Swarms. In *AIAA SciTech 2018*, Florida, 2018. AIAA.

[48] J.; Heikkilla and O. Silvén. A Four-step Camera Calibration Procedure with Implicit Image Correction. In *In Proceedings of the 1997 Computer Society Conference on Computer Vision and Pattern Recognition*, San Juan, Puerto Rico, 1997.

[49] E.D. Kaplan, J.L. Leva, D. Milbert, and M.S. Pavloff. *Fundamentals of Satellite Navigation. In Understanding GPS, Principles and Applications*. Artech House, Boston,MA, USA, 2nd edition, 2006.

[50] *GPS Standard Positioning Service Performance Standard*. Office of the Secretary of Defense, New York, NY, USA, 4th edition, 2008.

[51] A Parkins. Increasing GNSS RTK Availability with a New Single-Epoch Batch Partial Ambiguity Resolution Algorithm. *GPS Solutions*, 15(4):391–402, 2011.

[52] G Hu, D A Abbey, N Castleden, W E Featherstone, C Earls, O Ovstedal, and D Weihing. An Approach for Instantaneous Ambiguity Resolution for Medium- to Long-Range Multiple Reference Station Networks. *GPS Solutions*, 9(1):1–11, 2005.

[53] O Montenbruck, M Wermuth, R Kahle, Deutsches Zentrum, and Raumfahrt Dlr. GPS Based Relative Navigation for the TanDEM-X Mission - First Flight Results. *Earth*, (February 2016):2797–2807, 2011.

[54] J Liu, M E Cannon, P Alves, M G Petovello, G Lachapelle, G MacGougan, and L DeGroot. A performance comparison of single and dual frequency GPS ambiguity resolution strategies. *GPS Solutions*, 7(2):87–100, 2003.

[55] A. Renga, G. Fasano, D. Accardo, M. Grassi, U. Tancredi, G. Rufino, and A. Simonetti. Navigation facility for high accuracy offline trajectory and attitude estimation in airborne applications. *International Journal of Navigation and Observation*, 2013, 2013.

[56] P. J G Teunissen. The least-squares ambiguity decorrelation adjustment: a method for fast GPS integer ambiguity estimation. *Journal of Geodesy*, 70(1-2):65–82, 1995.

[57] Urbano Tancredi, Alfredo Renga, and Michele Grassi. Real-Time Relative Positioning of Spacecraft over Long Baselines. *Journal of Guidance, Control, and Dynamics*, 37(1):47–58, 2014.

[58] Paul D. Groves. *Principles of GNSS, Inertial, and Multisensor Integrated Navigation Systems*. 2008.

[59] S Verhagen. Integer ambiguity validation: an open problem? *GPS Solutions*, 8(1):36–43, 2004.

[60] W.G. Melbourne. The Case for Ranging in GPS-based Geodetic Systems. In *1st International Symposium on Precise Positioning with the Global Positioning System*, pages 373–386, 1985.

[61] G Wübbena. Software Developments for Geodetic Positioning with GPS using TI-4100 Code and Carrier Measurements. In *1st International Symposium on Precise Positioning with the Global Positioning System*, pages 403–412, 1985.

[62] Sandra Verhagen and Li Bofeng. LAMBDA software package, Matlab Implementation, Version 3.0, 2012.

[63] Paul D. Groves. Navigation using inertial sensors [Tutorial]. *IEEE Aerospace and Electronic Systems Magazine*, 30(2), 2015.

[64] M.D. Shuster and S.D. Oh. Three-axis attitude determination from vector observations. *AIAA Journal of Guidance and Control*, 4(1):70–77, 1981.

[65] Rui Hirokawa and Takuji Ebinuma. A Low-Cost Tightly Coupled GPS/INS for Small UAVs Augmented with Multiple GPS Antennas. *Journal of the Institute of Navigation*, 56(1):34–44, 2009.

[66] Comune di Napoli. Rilievo aerofotogrammetrico. 1:1000 del comune di Napoli.

[67] Y. Bar-Shalom. Update with out-of-sequence measurements in tracking: exact solution. *IEEE Trans. Aerosp. Electorn. Syst.*, 38(3), 2002.

[68] G. Fasano, D. Accardo, A.E. Tirri, A. Moccia, and E. De Lellis. Radar/electro-optical data fusion for non-cooperative UAS sense and avoid. *Aerospace Science and Technology*, 46:436–450, 2015.

[69] A. Bachrach, S. Prentice, R. He, and N. Roy. RANGE-Robust autonomous navigation in GPS-denied environments. *Journal of Field Robotics*, 28(5):644–666, 2011.

[70] Amedeo Rodi Vetrella, Giancarmine Fasano, and Domenico Accardo. Cooperative navigation in GPS-challenging environments exploiting position broadcast and vision-based tracking. In *IEEE, International Conference on Unmanned Aircraft Systems*, Arlington, VI, USA, 2016. IEEE.

[71] Amedeo Rodi Vetrella, Roberto Opromolla, Giancarmine Fasano, Domenico Accardo, and Michele Grassi. Autonomous Flight in GPS-Challenging Environments Exploiting Multi-UAV Cooperation and Vision-aided Navigation. In *AIAA Infotech@ Aerospace*, Grapevine, TX, USA, 2017. AIAA.

[72] (University of Minnesota). Impact and Mitigation of GPS-Unavailability on Small UAV Navigation, Guidance and Control.

[73] S. Weiss and Et alii. Monocular Vision for Long-term Micro Aerial Vehicle State Estimation: A Compendium. *Journal of Field Robotics*, 30(5):803–831, 2013.

[74] G. Chowdhary and Et alii. GPS-denied Indoor and Outdoor Monocular Vision Aided Navigation and Control of Unmanned Aircraft. *Journal of Field Robotics*, 30(3):415–438, 2013.

[75] A. Lie and Et Alii. An Airborne Experimental Test Platforms. *Inside GNSS*, pages 40–47, 2014.

[76] Z Zhu and Et alii. Architecture for Asymmetric Collaborative Navigation. In *IEEE PLANS*, 2012.

[77] B. Ludington, E. Johnson, and G. Vachtsevanos. Augmenting UAV Autonomy. *IEEE Robotics & Automation Magazine*, 13:63–71, 2006.

[78] Z. Yu, K. Nonami, J. Shin, and D. Celestino. 3D Vision Based Landing Control of a Small Scale Autonomous Helicopter. *International Journal of Advanced Robotic Systems*, 4:51–56, 2007.

[79] J. Kelly, S. Saripalli, and G. S. Sukhatme. Combined Visual and Inertial Navigation for An Unmanned Aerial Vehicle. In *Proceedings of the International Conference on Field and Service Robotics*, 2017.

[80] F. Caballero, L. Merino, J. Ferruz, and A. Ollero. Unmanned Aerial Vehicle Localization Based on Monocular Vision and Online Mosaicking. *Journal of Intelligent and Robotic Systems*, 55:323–343, 2009.

[81] S. Weiss and R. Siegwart. Real-time metric state estimation for modular vision-inertial systems. In *Proceedings of IEEE International Conference on Robotics and Automation*, pages 4531–4537, Shanghai, China,, 2011. IEEE.

[82] F. Andert, S. Lorenz, L. Mejias, and D. Bratanov. Radar-Aided Optical Navigation for Long and Large-Scale Flights over Unknown and Non-Flat Terrain. In *International Conference on Unmanned Aircraft Systems (ICUAS)*, 2016.

[83] L. Merino, J. Wiklund, F. Caballero, A. Moe, J.R. Martinez-De Dios, and Et Alii. Vision-Based Multi-UAV Position Estimation. *IEEE Robotics & Automotion Magazine*, 1070(9932), 2006.

[84] P.E. Forssen and A. Moe. View matching with blob features. In *in Proc. 2nd Canadian Conf Robot Vision,*, pages 228–235, 2005.

[85] V. Indelman and Et alii. Graph-Based distributed cooperative navigation for a general multi-robot measurement model. *International Journal of Robotics Research*, 31(9):1057–1080, 2012.

[86] I.V.; Melnyk, J.A.; Hesch, and S.I. Roumeliotis. Cooperative Vision-aided Inertial Navigation Using Overlapping Views. In *IEEE Int. Conf. on Robotics Automation*, Saint Paul, Minnesota, USA,, 2012.

[87] O. Shakernia, W.-Z. Chen, and V.M. Raska. Passive Ranging for UAV Sense and Avoid Applications,. In *AIAA Infotech@Aerospace*, 2005.

[88] R.M. Rogers. *Applied Mathematics in Integrated Navigation Systems*. AIAA Education Series.

[89] J. Shi and C. Tomasi. Good features to track. In *In Computer Vision and Pattern Recognition*, pages 593–600. IEEE, 1994.

[90] D. G. Lowe. Distinctive image features from scale-invariant keypoints. *International Journal of Computer Vision*, 60(2):91–110, 2004.

[91] E. Rublee, V. Rabaud, K. Konolige, and G. Bradski. ORB: An efficient alternative to SIFT or SURF. In *International conference on computer vision*, pages 2564–2571. IEEE, 2011.

[92] H. P. Gavin. The Levenberg-Marquardt method for nonlinear least squares curvefitting problems. Technical report, Technical Report. Department of Civil & Environmental Engineering, Duke University, 2013.

[93] F. Lu and R. Hartley. A fast optimal algorithm for L2 triangulation Tokyo. In *in Asian Conf. on Computer Vision*, pages 18–22, 2007.

[94] F. Andert and L. Mejias. Improving monocular SLAM with altimeter hints for fixed-wing aircraft navigation and emergency landing. In *2015 International Conference on Unmanned Aircraft Systems (ICUAS)*, 2015.

[95] Francesco Cocchioni, Adriano Mancini, and Sauro Longhi. Autonomous Navigation, Landing and Recharge of a Quadrotor using Artificial Vision. In *International Conference on Unmanned Aircraft Systems*, pages 418–429, 2014.

[96] Alvika Gautam, P B Sujit, and Srikanth Saripalli. A Survey of Autonomous Landing Techniques for UAVs. *International Conference on Unmanned Aircraft Systems*, pages 1210–1218, 2014.

[97] Amedeo Rodi Vetrella, Inkyu Sa, Marija Popovic, Raghav Khanna, Juan Nieto, Giancarmine Fasano, Domenico Accardo, and Roland Siegwart. Improved Tau-Guidance and Vision-aided Navigation for Robust Autonomous Landing of UAVs. In *Field and Service Robotics (FSR)*. Springer, 2017.

[98] D N Lee. A theory of visual control of braking based on information about time-to-collision. *Perception*, 5(4):437–459, 1976.

[99] Zuqiang Yang, Zhou Fang, and Ping Li. Decentralized 4D Trajectory Generation for UAVs Based on Improved Intrinsic Tau Guidance Strategy. *International Journal of Advanced Robotic Systems*, 13(3):1–13, 2016.

[100] Seungho Yoon, Youdan Kim, and Seungkeun Kim. Pursuit Guidance Law and Adaptive Backstepping Controller Design for Vision-Based Net-Recovery UAV. In *AIAA Guidance, Navigation and Control Conference and Exhibit*, number August, pages 1–33, Honolulu, HI, 2008. AIAA.

[101] Takeshi Yamasaki, Hirotoshi Sakaida, Keisuke Enomoto, Hiroyuki Takano, and National Defense Academy. Robust Trajectory-Tracking Method for UAV Guidance. In *International Conference on Control, Automation and Systems*, pages 1404–1409, Seoul, 2007. IEEE.

[102] D N Lee, M N O Davies, P R Green, and F R (Ruud). Van Der Weel. Visual control of velocity of approach by pigeons when landing. *Journal of Experimental Biology*, 180:85–104, 1993.

[103] Reuben Strydom, Aymeric Denuelle, and Mandyam V Srinivasan. Bio-Inspired Principles Applied to the Guidance , Navigation and Control of UAS. *Aerospace*, 3(21), 2016.

[104] F Kendoul. Four-dimensional guidance and control of movement using time-to-contact: Application to automated docking and landing of unmanned rotorcraft systems. *The International Journal of Robotics Research*, 33(2):237–267, 2013.

[105] Simon Lynen, Markus W Achtelik, Stephan Weiss, Margarita Chli, and Roland Siegwart. A Robust and Modular Multi-Sensor Fusion Approach Applied to MAV Navigation. In *IEEE/RSJ International Conference on Intelligent Robots and Systems*, pages 3923–3929, Tokyo, 2013. IEEE.

[106] Mina Kamel, Thomas Stastny, Kostas Alexis, and Roland Siegwart. *Model Predictive Control for Trajectory Tracking of Unmanned Aerial Vehicles Using Robot Operating System*, pages 3–39. Springer International Publishing, Cham, 2017.

[107] Fadri Furrer, Michael Burri, Markus Achtelik, and Roland Siegwart. RotorS A Modular Gazebo MAV Simulator Framework. *Springer International Publishing*, Volume 1:pp. 595–625, 2016.